Algorithms for real-frequency evaluation of diagrammatic expansions

by

©Amir Taheridehkordi

A thesis submitted to the School of Graduate Studies in partial fulfillment of the requirements for the degree of Doctor of Philosophy

Department of Physics and Physical Oceanography

Memorial University of Newfoundland

Fall 2020

St. John's Newfoundland

Abstract

We compute perturbative expansions of the self-energy and spin susceptibility functions in real-frequency space for the two-dimensional Hubbard model using a new solution method. Each term of the expansion, represented by a Feynman diagram, is translated into its mathematical representation, which includes two types of summations: momentum-space (spatial) and frequency-space (temporal). We introduce algorithmic Matsubara integration (AMI), a method which utilizes the residue theorem to perform the Matsubara frequency summations and store the result in a symbolic form. This method provides the exact result (up to machine precision) at minimal computational expense. We then combine AMI with the Monte Carlo methods to sample diagram topologies in the expansion and to perform momenta summations. To optimize the Monte Carlo integration procedure we group the diagrams according to the symmetry of their integrands determined by the graph invariant transformations (GITs). Since the result of AMI (up to momentum sums) is analytic in terms of the external Matsubara frequency, temperature (T), chemical potential (μ), and Hubbard on-site potential (U), the analytic continuation to the real-frequency axis can be performed symbolically at any point of $T - \mu - U$ phase space, even at $T = 0$ which has been inaccessible in standard methods due to non-ergodicity of the Monte Carlo sampling in this temperature regime. We compare our results to other numerical methods in the parameter regimes where the perturbative expansion is convergent,

and finally, benchmark our results on the real-frequency axis.

Lay Summary

Condensed matter physics explores materials composed of a huge number of particles and their collective behavior originating from their interactions. The complexity of these systems makes condensed matter phenomena a non-trivial field of science, which requires advanced analytical and numerical tools.

One of the most challenging and interesting problems in condensed matter theory is to determine the role of the electron-electron interactions in materials. For example, such interactions give rise to the metal-insulator transition, where the standard independent electron models predict the system to be fully metallic. Furthermore, electron-electron interactions are responsible for the emergence of high-temperature superconductivity. For these reasons this specific problem has attracted many researchers in theoretical, computational and experimental physics.

In order to theoretically describe electron-electron interactions one needs, as the first step, to consider a model that mimics realistic crystals. The Hubbard model is the simplest lattice model that simulates condensed matter systems with electron-electron interactions. The model assumes that the interaction (or potential) energy associated with two electrons is zero unless they occupy exactly the same site in the lattice, i.e., electrons are free to move around in the lattice and they only affect each other if they are at exactly the same place. Despite the conceptual simplicity of the model it turns out to be one of the most challenging problems in theoretical physics.

The model has been studied for decades but it has yet to be fully understood.

The goal of this thesis is to introduce a new methodology, based upon the well-known residue theorem, to systematically calculate different physical quantities for the Hubbard model. We use the so-called Feynman diagrammatic expansion, which is a pictorial version of perturbation theory in the context of quantum field theory. One might imagine each diagram as a representation of a set of scattering processes due to electron-electron interactions in the lattice, however, we should remember that each diagram represents a high-dimensional integral which finally yields to a number. The significant difference of our approach with other popular methods is that we solve part of the problem analytically. This enables us to provide the results in real (physical) frequency, moreover, other methods are based upon fully numerical algorithms which solve the model in the imaginary (non-physical) domain. As we shall show our method can be used to compute different physical thermodynamic observables such as electron densities, however, it is the *only* existing approach which can be used to calculate response functions such as charge and magnetic susceptibilities. Furthermore, its simplicity and generality makes it possible to be extended to many other problems in condensed matter and high-energy physics. We thus believe our method can potentially be applied to classes of problems which are currently considered to be intractable.

Co-Authorship

This is a manuscript style thesis comprised of three peer-reviewed papers published in Physical Review B: The first work "Algorithmic Matsubara integration for Hubbard-like models" was published in January 2019, the second work "Optimal grouping of arbitrary diagrammatic expansions via analytic pole structure" was published in March 2020, and the final work "Algorithmic approach to diagrammatic expansions for real-frequency evaluation of susceptibility functions" published in July 2020.

The thesis author (Amir Taheridehkordi) was the main contributor for all of the manuscripts included in this thesis, sharing authorship with Dr. Stephanie H. Curnoe and Dr. James P. F. LeBlanc, the supervisors for this PhD project. He selected the research problems addressed in the papers. He invented and developed the computational algorithms which he then (with his supervisor Dr. James P. F. LeBLanc) implemented in Python and C++, and he wrote the first draft of each paper.

Acknowledgements

I would like to thank my supervisors, Dr. Stephanie H. Curnoe and Dr. James P. F. LeBlanc, for their support, encouragement and guidance during this project; without their help this project would have not been the same.

I also wish to thank my wife, Khorshid, who stood by me through all my travels and absences during my PhD studies.

Table of Contents

List of Tables

List of Figures

List of abbreviations and symbols

AMI	Algorithmic Matsubara integration
β	Inverse temperature
c_i	Fermionic annihilation operator
χ_c	Charge spin susceptibility function
χ_L	Longitudinal spin susceptibility function
χ_T	Transverse spin susceptibility function
δ_{ij}	Kronecker delta
DiagMC	Diagrammatic Monte Carlo
F	Number of loops in a Feynman diagram
f	Fermi distribution function
$\mathcal{G}$	Matsubara Green's function
GIT	Graph invariant transformation
$i\nu_n$	Fermionic Matsubara frequency
$i\Omega$	Bosonic Matsubara frequency
$\mathbf{k}$	Crystal momentum vector
m	Order of a Feynman diagram
μ	Chemical potential
n_i	Number operator
1PIR	One-particle irreducible

ϕ	Feynman diagram topologies
Π	Polarization function
$\mathbf{r}$	Position vector
Res	Residue
RPA	Random phase approximation
s	Spin
T	Temperature
$\mathcal{T}$	Time ordering operator
t	Real time
τ	Imaginary time
TMA	T-matrix approximation
U	Hubbard interaction strength

Chapter 1

Introduction

A piece of solid material contains of the order of 10^{23} interacting particles. The theoretical treatment of interactions between such a huge number of particles is central to the field of many-body physics. Due to the large number of ions and electrons in a solid and the long range Coulomb interaction between them, an exact solution to the many-body Shrödinger equation is impossible to find. Therefore, various approximations and model systems have been introduced to describe the physics of interacting many-body systems [1].

The Hubbard model [2–4] is a cornerstone of correlated electron physics; by assuming a constant on-site interaction between electrons it simplifies the long-range Coulomb interaction in the lattice. Historically, the model has been first seen as a minimal model to describe the metal-insulator phase transition at half-filling (i.e., one particle per site). It was then comprehensively studied as the simplest many-body model with the potential to describe features of high-temperature superconductors [5, 6]. In recent years, the model has been of central interest due to its direct realization with ultra cold atom experiments [7–9]. Today the model is also considered as a test-bed for developing modern numerical methods in condensed matter

theory [10].

In order to describe the physics of the Hubbard Hamiltonian on a lattice, different numerical algorithms have been developed. These methods have a wide range from non-perturbative approaches such as dynamical mean-field theory (DMFT) and its extensions [11–13] and dual fermion (DF) techniques [14–18] to perturbation theory based approaches including diagrammatic Monte Carlo (DiagMC) [19–24], which uses Monte Carlo simulations to numerically evaluate the diagrammatic expansions of different physical observables. The approach used in this thesis is also based upon perturbation theory and uses some elements of DiagMC.

In standard DiagMC a combination of imaginary time (τ) and momentum ($\mathbf{k}$) spaces as well as diagram topologies (ϕ) are sampled [19] using the usual Metropolis-Hastings Monte Carlo simulation [25, 26]. Although DiagMC was initially proposed to evaluate the perturbative expansion of the polaron problem [27], thanks to the simplicity of the approach as well as its generality, it was also used to compute the Green's function and susceptibility expansions of the Hubbard model [10, 28]. It is now believed to be one of the most reliable techniques in many-body physics.

Similar to other many-body algorithms DiagMC relies on the so-called Matsubara formalism [29–31], i.e., the problem is solved in the imaginary time, or equivalently, imaginary frequency space. This is ideal for calculating thermodynamic quantities such as particle densities and energies, where the summations are performed over all of the independent temporal degrees of freedom (times, or equivalently, frequencies). However, expressing response functions, such as Green's functions, spectral functions and susceptibilities in real-time or real-frequency space, is a formidable task. Although there are numerical analytic continuation procedures to translate the results from the Matsubara axis to the real axis [32–36] they are all mathematically ill-posed and the resulting uncertainty in both high and low temperature regimes is high [37–39].

These uncertainties grow at high temperatures because Matsubara axis data becomes sparse, while obtaining precise Matsubara axis data at low temperatures becomes increasingly more challenging due to the compression of the Matsubara scale with decreased temperature. The main motivation of this work is to provide a perturbation theory based method to directly evaluate the expansions of the response functions in real-frequency space without need for any ill-defined numerical analytic continuation procedures.

As in standard DiagMC we represent each term of the perturbative series as a Feynman diagram [40–42], which is a pictorial representation of high-dimensional temporal-spatial integrals. We implement algorithms to systematically construct the diagram topologies. We then use the well-known Feynman rules to translate each unique topology to its corresponding mathematical expression in the frequency-momentum space.

Next we propose a new algorithm, based upon the standard residue theorem [43], which we call algorithmic Matsubara integration (AMI). Our algorithm applies to $\{\nu, \mathbf{k}, \phi\}$ space instead of probing $\{\tau, \mathbf{k}, \phi\}$ as is usually done in standard DiagMC. We *analytically* evaluate the temporal integrals of an arbitrary Feynman diagram arising from perturbative expansion of a physical object composed of bare Green's functions with bare vertices, such that, the result of the temporal integrals is exact (up to machine precision). As a result the sampling phase space in the Monte Carlo process is reduced from $\{\nu, \mathbf{k}, \phi\}$ to $\{\mathbf{k}, \phi\}$. In addition, since the solution of the temporal part is analytic in temperature T, chemical potential μ, Hubbard interaction U, and external frequency, the $T - \mu - U$ phase space can be explored with minimal computational expense. Moreover, analytic continuation can be performed symbolically, which eliminates the need for any numerical analytic continuation procedures. Furthermore, the method, in principle, enables us to evaluate a truncated perturba-

tive expansion at any temperature, even in $T = 0$ limit; this limit is unreachable in standard DiagMC methods since the set of Matsubara frequencies compresses as the temperature decreases, i.e., in the zero temperature limit the number of samples needed to obtain reasonable statistical errors tends to infinity. In this thesis, we concentrate on the two-dimensional (2D) single-band Hubbard model, however, AMI is general enough to be applied to any diagrammatic expansion with arbitrary dimensionality in condensed matter or high-energy physics as long as the analytic representations of the terms are known.

We then complete our machinery by combining AMI with Monte Carlo methods. We propose two different Monte Carlo simulations to probe the momentum and topological spaces. In DiagMC methods, to suppress the sign problem the diagrams are represented as determinants [22, 44, 45]. In our case, since we evaluate the diagrams in Matsubara frequency space rather than imaginary time space, such a manipulation is not feasible. We instead utilize the analytical pole structure of the diagrams to construct the so-called sign-blessed groups. Doing so we dramatically reduce the sign problem in the numerical evaluation of the diagrams. We use our algorithm to evaluate the self-energy, Green's function and susceptibility functions on the Matsubara axis for the 2D Hubbard model; we benchmark our results and compare to other numerical methods to prove the correctness of our method. Lastly, for the first time, we provide real-frequency results for the spectral function and spin susceptibility without application of numerical analytic continuation procedures.

The rest of this thesis is organized as follows. In Chapter 2 we review the principles of quantum field theory, the Hubbard model and perturbation theory in the Green's function formalism. At the end of the chapter we present the diagrammatic expansions of the self-energy and susceptibility functions for the Hubbard model, which are the physical quantities we are mostly interested in. Readers who are already famil-

iar with Feynman diagrammatic techniques could skip this chapter. We reproduce our first publication [46] in Chapter 3, which explains the details of AMI and its implementation. In Chapter 4, we reproduce our second publication [47], where we describe first our algorithm to generate diagrammatic expansions and translate them to integrals in the frequency-momentum space. Taking the self-energy function as an example, we construct optimally sign-blessed groups and evaluate the expansion in both imaginary and real-frequency space. In Chapter 5 we use our methodology to evaluate the spin-susceptibility functions for the 2D Hubbard model at half-filling. In this chapter we reproduce our third publication [48], in which, for the first time, the transverse spin susceptibility is calculated as a function of real frequency beyond the common low order approximations. We also investigate the role of diagrams in the low coupling regime order-by-order. Finally, we summarize the thesis in Chapter 6 and discuss future work.

Bibliography

[1] A. Fetter and J. Walecka. *Quantum Theory of Many-particle Systems*. Dover Publications, Mineola, New York, 2003.

[2] J. Hubbard and B. H. Flowers. Electron correlations in narrow energy bands. *Series A. Math. and Phys. Sci.*, 276, 1963.

[3] Elliott H. Lieb and F. Y. Wu. Absence of Mott Transition in an Exact Solution of the Short-Range, One-Band Model in One Dimension. *Phys. Rev. Lett.*, 20:1445–1448, 1968.

[4] J. P. F. LeBlanc, Andrey E. Antipov, Federico Becca, Ireneusz W. Bulik, Garnet Kin-Lic Chan, Chia-Min Chung, Youjin Deng, Michel Ferrero, Thomas M. Hen-

derson, Carlos A. Jiménez-Hoyos, E. Kozik, Xuan-Wen Liu, Andrew J. Millis, N. V. Prokof'ev, Mingpu Qin, Gustavo E. Scuseria, Hao Shi, B. V. Svistunov, Luca F. Tocchio, I. S. Tupitsyn, Steven R. White, Shiwei Zhang, Bo-Xiao Zheng, Zhenyue Zhu, and Emanuel Gull. Solutions of the Two-Dimensional Hubbard Model: Benchmarks and Results from a Wide Range of Numerical Algorithms. *Phys. Rev. X*, 5:041041, 2015.

[5] F. Mancini, S. Marra, and H. Matsumoto. Spin magnetic susceptibility in the two-dimensional Hubbard model. *Phys. C: Superconduc.*, 252(3):361–374, 1995.

[6] Youjin Deng, Evgeny Kozik, Nikolay V Prokof'ev, and Boris V Svistunov. Emergent BCS regime of the two-dimensional fermionic Hubbard model: Ground-state phase diagram. *Europhys. Lett.*, 110(5):57001, 2015.

[7] Michael Köhl, Henning Moritz, Thilo Stöferle, Kenneth Günter, and Tilman Esslinger. Fermionic Atoms in a Three Dimensional Optical Lattice: Observing Fermi Surfaces, Dynamics, and Interactions. *Phys. Rev. Lett.*, 94:080403, 2005.

[8] Robert Jördens, Niels Strohmaier, Kenneth Günter, Henning Moritz, and Tilman Esslinger. A Mott insulator of fermionic atoms in an optical lattice. *Nature*, 455(7210):204–207, 2008.

[9] Peter T. Brown, Debayan Mitra, Elmer Guardado-Sanchez, Peter Schauß, Stanimir S. Kondov, Ehsan Khatami, Thereza Paiva, Nandini Trivedi, David A. Huse, and Waseem S. Bakr. Spin-imbalance in a 2D Fermi-Hubbard system. *Science*, 357(6358):1385–1388, 2017.

[10] Thomas Schäfer, Nils Wentzell, Fedor Šimkovic IV, Yuan-Yao He, Cornelia Hille, Marcel Klett, Christian J. Eckhardt, Behnam Arzhang, Viktor Harkov, François-Marie Le Régent, Alfred Kirsch, Yan Wang, Aaram J. Kim, Evgeny

Kozik, Evgeny A. Stepanov, Anna Kauch, Sabine Andergassen, Philipp Hansmann, Daniel Rohe, Yuri M. Vilk, James P. F. LeBlanc, Shiwei Zhang, A. M. S. Tremblay, Michel Ferrero, Olivier Parcollet, and Antoine Georges. Tracking the Footprints of Spin Fluctuations: A Multi-Method, Multi-Messenger Study of the Two-Dimensional Hubbard Model. *arXiv:2006.10769*, 2020.

[11] Antoine Georges, Gabriel Kotliar, Werner Krauth, and Marcelo J. Rozenberg. Dynamical mean-field theory of strongly correlated fermion systems and the limit of infinite dimensions. *Rev. Mod. Phys.*, 68:13–125, 1996.

[12] G. Kotliar, S. Y. Savrasov, K. Haule, V. S. Oudovenko, O. Parcollet, and C. A. Marianetti. Electronic structure calculations with dynamical mean-field theory. *Rev. Mod. Phys.*, 78:865–951, 2006.

[13] A. Toschi, A. A. Katanin, and K. Held. Dynamical vertex approximation: A step beyond dynamical mean-field theory. *Phys. Rev. B*, 75:045118, 2007.

[14] A. N. Rubtsov, M. I. Katsnelson, and A. I. Lichtenstein. Dual fermion approach to nonlocal correlations in the Hubbard model. *Phys. Rev. B*, 77:033101, 2008.

[15] A. N. Rubtsov, M. I. Katsnelson, A. I. Lichtenstein, and A. Georges. Dual fermion approach to the two-dimensional Hubbard model: Antiferromagnetic fluctuations and Fermi arcs. *Phys. Rev. B*, 79:045133, 2009.

[16] Andrey E. Antipov, James P. F. LeBlanc, and Emanuel Gull. Opendf - An Implementation of the Dual Fermion Method for Strongly Correlated Systems. *Phys. Proc.*, 68:43–51, 2015.

[17] Jan Gukelberger, Evgeny Kozik, and Hartmut Hafermann. Diagrammatic Monte Carlo approach for diagrammatic extensions of dynamical mean-field theory:

Convergence analysis of the dual fermion technique. *Phys. Rev. B*, 96:035152, 2017.

[18] Sergei Iskakov, Hanna Terletska, and Emanuel Gull. Momentum-space cluster dual-fermion method. *Phys. Rev. B*, 97:125114, 2018.

[19] Kris Van Houcke, Evgeny Kozik, N. Prokof'ev, and B. Svistunov. Diagrammatic Monte Carlo. *Phys. Proc.*, 6:95–105, 2010.

[20] K. Van Houcke, F. Werner, E. Kozik, N. Prokof'ev, B. Svistunov, M. J. H. Ku, A. T. Sommer, L. W. Cheuk, A. Schirotzek, and M. W. Zwierlein. *Nat. Phys.*, 8:366, 2012.

[21] E. Kozik, K. Van Houcke, E. Gull, L. Pollet, N. Prokof'ev, B. Svistunov, and M. Troyer. Diagrammatic Monte Carlo for correlated fermions. *Europhys. Lett.*, 90(1):10004, 2010.

[22] Riccardo Rossi. Determinant Diagrammatic Monte Carlo Algorithm in the Thermodynamic Limit. *Phys. Rev. Lett.*, 119:045701, 2017.

[23] Nikolay Prokof'ev and Boris Svistunov. Bold Diagrammatic Monte Carlo Technique: When the Sign Problem Is Welcome. *Phys. Rev. Lett.*, 99:250201, 2007.

[24] S. A. Kulagin, N. Prokof'ev, O. A. Starykh, B. Svistunov, and C. N. Varney. Bold Diagrammatic Monte Carlo Method Applied to Fermionized Frustrated Spins. *Phys. Rev. Lett.*, 110:070601, 2013.

[25] M. E. J. Newman and G. T. Barkema. *Monte Carlo Methods in Statistical Physics*. Clarendon Press, 1999.

[26] K. Binder. *Monte Carlo Methods in Statistical Physics (Topics in Current Physics)*. Springer, 1986.

[27] Nikolai V. Prokof'ev and Boris V. Svistunov. Polaron Problem by Diagrammatic Quantum Monte Carlo. *Phys. Rev. Lett.*, 81:2514–2517, 1998.

[28] J. P. F. LeBlanc, Andrey E. Antipov, Federico Becca, Ireneusz W. Bulik, Garnet Kin-Lic Chan, Chia-Min Chung, Youjin Deng, Michel Ferrero, Thomas M. Henderson, Carlos A. Jiménez-Hoyos, E. Kozik, Xuan-Wen Liu, Andrew J. Millis, N. V. Prokof'ev, Mingpu Qin, Gustavo E. Scuseria, Hao Shi, B. V. Svistunov, Luca F. Tocchio, I. S. Tupitsyn, Steven R. White, Shiwei Zhang, Bo-Xiao Zheng, Zhenyue Zhu, and Emanuel Gull. Solutions of the Two-Dimensional Hubbard Model: Benchmarks and Results from a Wide Range of Numerical Algorithms. *Phys. Rev. X*, 5:041041, 2015.

[29] G. D. Mahan. *Many-particle physics*. Plenum Press, New York, 1981.

[30] M. V. Sadovskii. *Diagrammatic: Lectures on Selected Problems in Condensed Matter Theory*. World Scientific, 2006.

[31] A. A. Abrikosov, L. P. Gorkov, and Dzyaloshinskii. *Methods of Quantum Field Theory in Statistical Physics*. Pergamon Press, Oxford, 1963.

[32] Dominic Bergeron and A.-M. S. Tremblay. Algorithms for optimized maximum entropy and diagnostic tools for analytic continuation. *Phys. Rev. E*, 94:023303, 2016.

[33] R. Levy, J. P. F. LeBlanc, and E. Gull. Implementation of the Maximum Entropy Method for Analytic Continuation. *Comp. Phys. Comm.*, 215:149, 2017.

[34] A. Gaenko, A. E. Antipov, G. Carcassi, T. Chen, X. Chen, Q. Dong, L. Gamper, J. Gukelberger, R. Igarashi, S. Iskakov, M. Könz, J. P. F. LeBlanc, R. Levy, P. N. Ma, J. E. Paki, H. Shinaoka, S. Todo, M. Troyer, and E. Gull. Updated core libraries of the ALPS project. *Comp. Phys. Comm.*, 213:235–251, 2017.

[35] Alexander Gaenko, Emanuel Gull, Andrey E. Antipov, Lukas Gamper, Gabriele Carcassi, Joe Paki, Ryan Levy, Michele Dolfi, Jonas Greitemann, and James P.F. LeBlanc. ALPSCore: Version 0.5.4, 2016.

[36] Markus Wallerberger, Sergei Iskakov, Alexander Gaenko, Joseph Kleinhenz, Igor Krivenko, Ryan Levy, Jia Li, Hiroshi Shinaoka, Synge Todo, Tianran Chen, Xi Chen, James P. F. LeBlanc, Joseph E. Paki, Hanna Terletska, Matthias Troyer, and Emanuel Gull. *arXiv:1811.08331*, 2018.

[37] J. Vučičević, J. Kokalj, R. Žitko, N. Wentzell, D. Tanasković, and J. Mravlje. Conductivity in the Square Lattice Hubbard Model at High Temperatures: Importance of Vertex Corrections. *Phys. Rev. Lett.*, 123:036601, 2019.

[38] Edwin W. Huang, Ryan Sheppard, Brian Moritz, and Thomas P. Devereaux. Strange metallicity in the doped Hubbard model. *Science*, 366(6468):987–990, 2019.

[39] J. Vučičević and M. Ferrero. Real-frequency diagrammatic Monte Carlo at finite temperature. *Phys. Rev. B*, 101:075113, 2020.

[40] R. P. Feynman. Space-Time Approach to Quantum Electrodynamics. *Phys. Rev.*, 76:769–789, 1949.

[41] Gordon Baym and Leo P. Kadanoff. Conservation Laws and Correlation Functions. *Phys. Rev.*, 124:287–299, 1961.

[42] J. M. Luttinger and J. C. Ward. Ground-State Energy of a Many-Fermion System. II. *Phys. Rev.*, 118:1417–1427, 1960.

[43] H. J. Weber and G. B. Arfken. *Essential Mathematical Methods for Physicists*. Academic Press, London, 2003.

[44] Fedor Šimkovic and Evgeny Kozik. Determinant Monte Carlo for irreducible Feynman diagrams in the strongly correlated regime. *Phys. Rev. B*, 100:121102, 2019.

[45] Alice Moutenet, Wei Wu, and Michel Ferrero. Determinant Monte Carlo algorithms for dynamical quantities in fermionic systems. *Phys. Rev. B*, 97:085117, 2018.

[46] Amir Taheridehkordi, S. H. Curnoe, and J. P. F. LeBlanc. Algorithmic Matsubara integration for Hubbard-like models. *Phys. Rev. B*, 99:035120, 2019.

[47] Amir Taheridehkordi, S. H. Curnoe, and J. P. F. LeBlanc. Optimal grouping of arbitrary diagrammatic expansions via analytic pole structure. *Phys. Rev. B*, 101:125109, 2020.

[48] Amir Taheridehkordi, S. H. Curnoe, and J. P. F. LeBlanc. Algorithmic approach to diagrammatic expansions for real-frequency evaluation of susceptibility functions. *Phys. Rev. B*, 102:045115, 2020.

Chapter 2

Background material

This chapter is devoted to reviewing the essential theoretical tools used in this work. We first provide some basics about the Hubbard model. Then we present the finite temperature Green's function formalism and mention the diagrammatic expansion of the Green's and susceptibility functions.

2.1 Hubbard model

The Hubbard model was originally proposed to model electronic correlations in narrow energy bands [1]. The model was independently suggested by Gutzwiller [2] and Kanamori [3] around the same time. The Hamiltonian is given by

$$H = -t \sum_{\langle i,j\rangle\sigma} (c^{\dagger}_{i\sigma} c_{j\sigma} + c^{\dagger}_{j\sigma} c_{i\sigma}) - \mu \sum_{i\sigma} n_{i\sigma} + U \sum_{i} n_{i\uparrow} n_{i\downarrow}. \tag{2.1}$$

where i and j are two indices which denote the lattice site, $\langle i, j\rangle$ implies that only hopping to the nearest neighbor is allowed without spin flipping, $\uparrow$ and $\downarrow$ are spin up and down, respectively, $c_{i\sigma}$ ($c^{\dagger}_{i\sigma}$) annihilates (creates) an electron with spin σ at site i, $n_{i\sigma} = c^{\dagger}_{i\sigma} c_{i\sigma}$ is the number operator which counts the number of electrons in site i, and

μ is the chemical potential. The first and the third terms are kinetic (tight-binding) and potential (Hubbard) terms of the Hamiltonian, respectively.

2.2 Finite temperature Green's function

At finite temperature T, the Matsubara Green's function is defined to be [4]

$$\mathcal{G}(\mathbf{k}, \tau_2 - \tau_1) = -\langle \mathcal{T}_\tau \psi_{\mathbf{k}}(\tau_2) \psi^\dagger_{\mathbf{k}}(\tau_1) \rangle, \tag{2.2}$$

where τ is imaginary (Matsubara) time $0 < \tau < \beta = 1/T$, $\mathcal{T}_\tau$ is Matsubara time-ordering operator, and $\psi_{\mathbf{k}}(\tau)$ ($\psi^\dagger_{\mathbf{k}}(\tau)$) annihilates (creates) a particle in state $\mathbf{k}$ and is given by

$$\psi_{\mathbf{k}}(\tau) = e^{H\tau} \psi_{\mathbf{k}} e^{-H\tau}, \tag{2.3}$$

where $\psi_{\mathbf{k}} = \psi_{\mathbf{k}}(0)$. In addition, for an observable O, $\langle O \rangle$ is average over grand canonical ensemble defined by

$$\langle O \rangle = \frac{\mathrm{Tr}[\rho O]}{\mathrm{Tr}[\rho]}, \tag{2.4}$$

with $\rho = e^{-\beta H}$. The finite temperature Green's function can be expanded in frequency space using the Fourier expansion

$$\mathcal{G}(\mathbf{k}, \tau) = \frac{1}{\beta} \sum_{n=-\infty}^{+\infty} e^{-i\nu_n \tau} \mathcal{G}(\mathbf{k}, i\nu_n), \tag{2.5}$$

or equivalently

$$\mathcal{G}(\mathbf{k}, i\nu_n) = \frac{1}{2} \int_{-\beta}^{+\beta} d\tau e^{i\nu_n \tau} \mathcal{G}(\mathbf{k}, \tau). \tag{2.6}$$

Moreover, for fermionic systems Eq. (2.4) implies that

$$\mathcal{G}(\mathbf{k},\tau) = -\mathcal{G}(\mathbf{k},\tau+\beta). \tag{2.7}$$

Replacing (2.7) in (2.5) we immediately see that the terms with even n are vanishing and for fermions we always encounter with odd Matsubara frequencies $\nu_n = (2n+1)\pi/\beta$. Similar arguments for bosons shows that only even Matsubara frequencies emerge. Furthermore, the bare Matsubara Green's function is given by [4]

$$\mathcal{G}_0(\mathbf{k},\tau) = \{\theta(\tau)[1-f(\mathbf{k})] - \theta(-\tau)f(\mathbf{k})\}e^{-(\epsilon(\mathbf{k})-\mu)\tau}, \tag{2.8}$$

where $f(\mathbf{k}) = [1+e^{\beta(\epsilon(\mathbf{k})-\mu)}]^{-1}$ is the Fermi distribution function, $\epsilon(\mathbf{k})$ is the energy dispersion and $\theta(\tau)$ is the step function. Substituting Eq. (2.8) into Eq. (2.6) we obtain the bare Matsubara Green's function in frequency domain:

$$\mathcal{G}_0(\mathbf{k}, i\nu_n) = \frac{1}{i\nu_n - \epsilon(\mathbf{k}) + \mu}. \tag{2.9}$$

In order to obtain the real frequency result one finally replaces $i\nu_n \to \nu + i0^+$.

2.3 Diagrammatic expansion of Green's function

We aim to find the perturbative expansion of the finite temperature Green's function for a general two-body potential. Following the so-called S-matrix approach [5] one

can easily show:

$$\mathcal{G}(\mathbf{r}_1,\tau,\mathbf{r}_2,\tau') = \frac{\mathrm{Tr}\left\{e^{-\beta H_0}\sum_{n=0}^{\infty}\frac{(-1)^n}{n!}\int_{\tau_0}^{\tau}d\tau_1...\int_{\tau_0}^{\tau}d\tau_n\mathcal{T}_\tau V_I(\tau_1)...V_I(\tau_n)\psi(\mathbf{r},\tau)\psi^\dagger(\mathbf{r}',\tau')\right\}}{\mathrm{Tr}\left\{e^{-\beta H_0}\sum_{n=0}^{\infty}\frac{(-1)^n}{n!}\int_{\tau_0}^{\tau}d\tau_1...\int_{\tau_0}^{\tau}d\tau_n\mathcal{T}_\tau V_I(\tau_1)...V_I(\tau_n)\right\}}, \tag{2.10}$$

where H_0 is the free Hamiltonian operator *, $\psi(\mathbf{r},\tau)(\psi^\dagger(\mathbf{r},\tau))$ is the annihilation (creation) operator at position $\mathbf{r}$ and imaginary time τ and V_I is the two-body potential in the interaction picture given by

$$V_I(\tau_i) = e^{H_0\tau_i}\frac{1}{2}\int d\mathbf{r}d\mathbf{r}'\psi^\dagger(\mathbf{r})\psi^\dagger(\mathbf{r}')V(\mathbf{r},\mathbf{r}')\psi(\mathbf{r}')\psi(\mathbf{r})e^{-H_0\tau_i}, \tag{2.11}$$

Next we define [5]

$$v(x-x') = V(\mathbf{r}-\mathbf{r}')\delta(\tau-\tau'), \tag{2.12}$$

$$\psi(x_i) = e^{H_0\tau_i}\psi(\mathbf{r})e^{-H_0\tau_i}, \tag{2.13}$$

For example, we evaluate the first order term in the numerator of Eq. (2.10) (we call it $G_1(x,x')$):

$$G_1(x,x') = \frac{1}{2}\mathrm{Tr}\left(e^{-\beta H_0}\int d^4x_1d^4x_2v(x_1-x_2)\mathcal{T}_\tau\psi^\dagger(x_1)\psi^\dagger(x_2)\psi(x_2)\psi(x_1)\psi(x)\psi^\dagger(x')\right). \tag{2.14}$$

*For the Hubbard model H_0 includes the first and the second terms in Eq. (2.1).

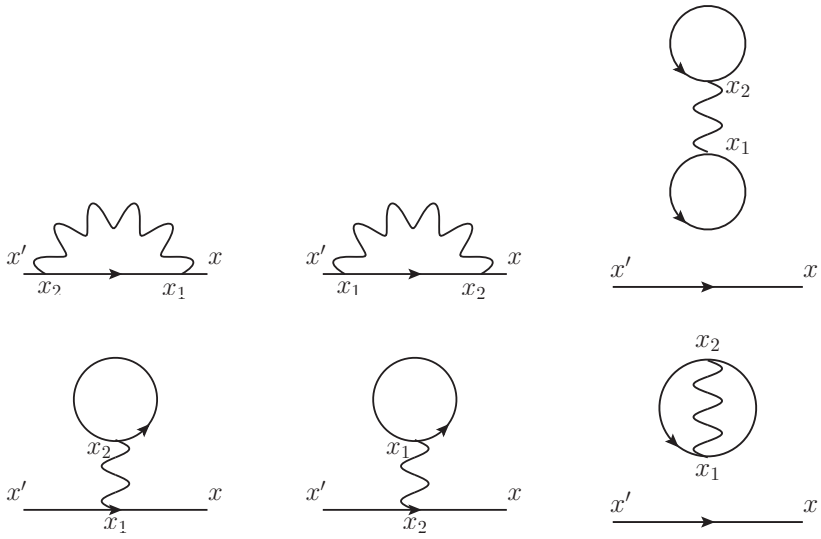

Figure 2.1: Feynman diagrams of the six first order terms arising from the perturbative expansion Eq. (2.10) of the numerator of the Green's function.

Applying Wick's theorem [5] we get six terms:

$$\begin{aligned} G_1(x,x') = \frac{1}{2}\int d^4x_1 d^4x_2 v(x_1-x_2)\Big[&\mathcal{G}_0(x,x')\mathcal{G}_0(x_2,x_2)\mathcal{G}_0(x_1,x_1) \\ &- \mathcal{G}_0(x,x')\mathcal{G}_0(x_2,x_1)\mathcal{G}_0(x_1,x_2) + \mathcal{G}_0(x,x_1)\mathcal{G}_0(x_1,x_2)\mathcal{G}_0(x_2,x') \\ &- \mathcal{G}_0(x,x_1)\mathcal{G}_0(x_2,x_2)\mathcal{G}_0(x_1,x') + \mathcal{G}_0(x_2,x_1)\mathcal{G}_0(x,x_2)\mathcal{G}_0(x_1,x') \\ &- \mathcal{G}_0(x,x_2)\mathcal{G}_0(x_1,x_1)\mathcal{G}_0(x_2,x')\Big]. \end{aligned} \tag{2.15}$$

Note that by commuting the fermionic operators we get extra minus sign in three of the terms. We present these six terms pictorially in Fig. 2.1. There are two types of diagrams: connected and disconnected. While the numerator of Eq. (2.10) (evaluated to all orders in perturbation theory) is in fact the product of the total contribution of the disconnected diagrams and total contribution of the connected diagrams, the denominator of Eq. (2.10) is just the sum of the disconnected diagrams. Therefore, only the connected diagrams effectively contribute in the final perturbative

expansion. Considering the first order connected diagrams, we observe that for any distinct topology there are two identical terms. In general, at the nth order there are $2^n n!$ identical terms for each distinct topology.

In this thesis we work in the momentum-frequency space. Here, we summarize the so-called *Feynman rules* in momentum-frequency space for mth order contribution to Green's function:

- Draw all topologically distinct diagrams with m interaction lines (wavy lines) and $2m+1$ particle lines (solid lines).
- Assign a momentum and Matsubara frequency to each particle line considering conservation of energy at each vertex.
- Assign a bare Green's function $\mathcal{G}_0 = \frac{1}{i\nu_n - \epsilon(\mathbf{k}) + \mu}$ to each solid line with frequency $i\nu_n$ and momentum $\mathbf{k}$.
- Each interaction line should be weighted with $v(\mathbf{k})$.
- Perform summations over all internal (independent) momenta and frequencies.
- Multiply each diagram by $(-1)^m (-1)^F (2s+1)^F \frac{T^m}{(2\pi)^{dm}}$ where F is the number of loops in the diagram, d is the dimensionality of the model and s is the spin.
- Insert convergence factor $e^{i\nu_n 0^+}$ for each simple closed fermionic loop, where ν_n is the assigned frequency to the line.

2.3.1 Dyson's equation and self-energy

Since any diagram in the perturbative expansion of Green's function is in fact a high dimensional integral in frequency-momentum (or equivalently in time-position) space, any effort to reduce the diagrammatic space is valuable. To do so Dyson's equation

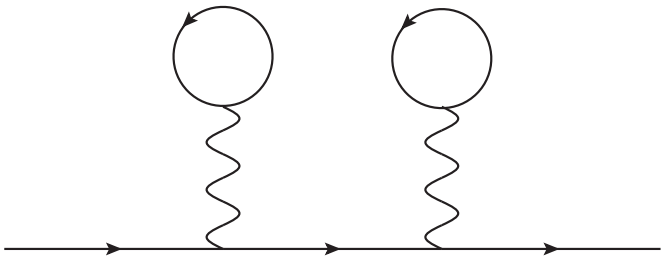

Figure 2.2: An example of a one-particle reducible diagram. The diagram is split into two connected diagrams by cutting the solid line in the middle.

is usually used. In principle Dyson's equation enables one to perform a summation of an infinite sub-series of Green's function diagrams [4]. In the series expansion of the Green's function there exist two classes of diagrams. The first class, which are called one-particle reducible diagrams, are those that can be split into two diagrams by cutting one of the fermionic (solid) lines. We show an example of such diagrams in Fig. 2.2. The second class of diagrams are those which are not reducible and, therefore, are called one-particle irreducible (1PIR) diagrams. We then define self-energy (Σ) to be the sum of all the 1PIR Green's function diagrams dropping the bare Green's functions assigned to the external legs. Finally, the full Green's function is determined by Dyson's equation:

$$\mathcal{G} = \mathcal{G}_0 + \mathcal{G}_0 \Sigma \mathcal{G}. \tag{2.16}$$

Therefore, in order to approximate Green's function one could evaluate the self-energy expansion up to some truncation order and substitute the result in Eq. (2.16).

2.3.2 Hubbard self-energy diagrams

We are mostly interested in the Hubbard model on a two-dimensional square lattice. We limit ourselves to the nearest neighbor tight-binding dispersion given by $\epsilon(\mathbf{k}) =$

$-2t\Big(\cos k_x + \cos k_y\Big) - \mu$, where t is the hopping amplitude and μ is the chemical potential. Following the Feynman rules, in general, the diagrammatic expansion of the Hubbard self-energy, truncated at order m_c, mathematically corresponds to

$$\Sigma(\mathbf{k}_{m+1}, \nu_{m+1}) = \sum_{m=1}^{m_c} \Bigg\{ \sum_{\{\zeta_m\}} \frac{(-1)^{m+F_{\zeta_m}} U^m}{(2\pi)^{2m} \beta^m} \sum_{\{\mathbf{k}_m\}} \sum_{\{\nu_m\}} \prod_{j=1}^{2m-1} \mathcal{G}_0^j(\epsilon^j, X^j) \Bigg\}, \qquad (2.17)$$

where $\{\zeta_m\}$ is the set of diagram topologies of order m and F_{ζ_m} is the number of fermionic loops in the diagram with topology ζ_m. Note that a self-energy diagram of order m has $2m-1$ solid lines and m (independent) internal frequencies and momenta. Here, we define the frequency of each line as the linear combination $X^j = \sum_{\ell=1}^{m+1} i\alpha_\ell^j \nu_\ell$, where ν_ℓ are the independent Matsubara frequencies and the allowed values for the coefficients α_ℓ^j are zero, plus one, or minus one. Similarly, the free particle energy is $\epsilon^j = \epsilon(\mathbf{K}_j)$, where $\mathbf{K}_j = \sum_{\ell=1}^{m+1} \alpha_\ell^j \mathbf{k}_\ell$ and $\mathbf{k}_\ell$ are the independent momenta. Moreover, on LHS of Eq. (2.17), ν_{m+1} and $\mathbf{k}_{m+1}$ are the external frequency and momentum, respectively.

We store connected one-particle irreducible diagrams that are Hubbard-type, i.e., we store the set of 1PIR diagrams, in which, the interaction lines connect fermionic lines with different spins. The total number of such diagrams at each order $N_{init}^{(m)}$ is given in Table. 2.1. We also use a simple but powerful trick to decrease the number of diagrams in the diagrammatic expansions by redefining the chemical potential [6] and neglecting all the diagrams with tadpole insertions (the diagrams which include fermionic loops attached by a wavy tail):

$$\mu \to \mu - U n_\sigma, \qquad (2.18)$$

where n_σ is the density of particles with spin $\sigma \in \{\uparrow, \downarrow\}$. Thus, in order to determine the density and redefined (or effective) chemical potential one should take the following

steps [7]:

1. For the chemical potential μ find the density of particles by using [6]:

$$n = 2n_\sigma, \tag{2.19}$$

with

$$n_\sigma = \frac{1}{(2\pi)^2} \sum_{\mathbf{k}} \mathcal{G}_\sigma(\tau = 0^-, \mathbf{k}), \tag{2.20}$$

where $\mathcal{G}_\sigma$ is the full Green's function which can be approximated by using Dyson's equation. Note that the self-energy diagrams with tadpole insertions must be dropped from the expansion. We recall that

$$\mathcal{G}_\sigma(\tau, \mathbf{k}) = \frac{1}{\beta} \sum_{i\nu_n} e^{-i\nu_n \tau} \mathcal{G}_\sigma(i\nu_n, \mathbf{k}), \tag{2.21}$$

where $i\nu_n$ are fermionic Matsubara frequencies. Therefore, to compute n_σ one should perform sums over the external Matsubara frequency and momentum.

2. Calculate the effective chemical potential:

$$\mu_{\text{eff}} = \mu - Un/2. \tag{2.22}$$

3. Repeat steps 1 and 2 self-consistently to achieve density and effective chemical potential. For instance, for the half-filled model ($n = 1$) we have $\mu = U/2$ and $n_\uparrow = n_\downarrow = 1/2$ which corresponds to $\mu_{\text{eff}} = 0$.

In order to complete our discussion we consider the Hubbard self-energy diagrams at third order shown in Fig. 2.3. Six of the eighth diagrams can be neglected by

Table 2.1: Diagrammatic space for the Hubbard self-energy expansion up to sixth order. $N_{init}^{(m)}$ is the total number of mth order Hubbard self-energy diagrams in the original expansion. $N^{(m)}$ is the total number of mth order Hubbard self-energy diagrams neglecting all diagrams with tadpole insertions by applying the chemical potential shift explained in the text.

m	1	2	3	4	5	6
$N_{init}^{(m)}$	1	2	8	44	296	2312
$N^{(m)}$	0	1	2	12	70	515

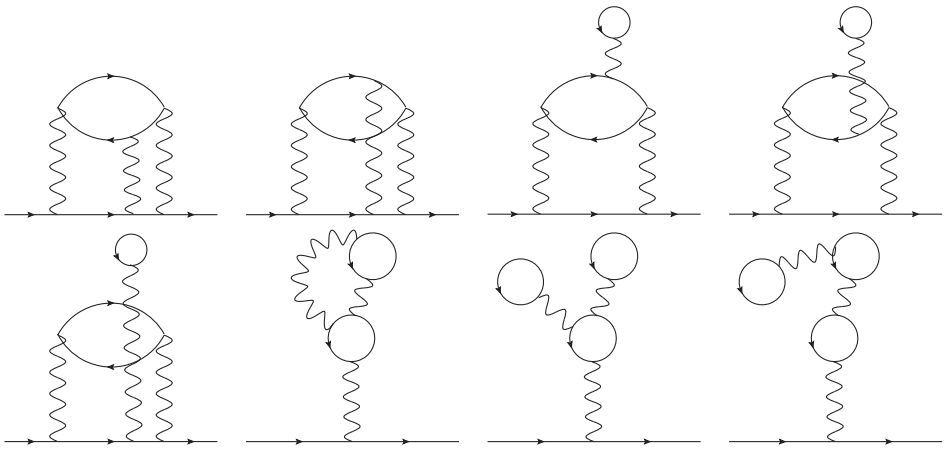

Figure 2.3: The third order terms of the Hubbard self-energy expansion. In this series expansion we only consider the terms which are non-zero for the on-site Hubbard potential between two electrons with different spins. After shifting the chemical potential only the first two diagrams in the first row remain.

shifting the chemical potential self-consistently. Therefore, we are left with only two third order diagrams. Shown in the third row of Table 2.1 are the number of self-energy diagrams which one needs to evaluate at each order for the Hubbard model.

2.4 Diagrammatic expansion of susceptibility functions

In this section we use the S-matrix approach to construct the perturbative series expansion of the spin susceptibility functions for the single-band Hubbard model. We define two types of susceptibility functions: longitudinal spin susceptibility and transverse spin susceptibility. As we shall see, the diagrammatic representation of the longitudinal spin susceptibility is closely related to that of the charge susceptibility, however, the perturbative expansion for the transverse spin susceptibility leads to different diagram topologies.

2.4.1 Longitudinal spin susceptibility

The longitudinal spin susceptibility $\chi_L(x, x')$ is defined to be [8]

$$\chi_L(x, x') = \langle \mathcal{T}_\tau S^z(x) S^z(x') \rangle, \tag{2.23}$$

where

$$S^z(x) = \frac{1}{2} \sum_{\sigma,\sigma'} \psi^\dagger_\sigma(x) \sigma^z_{\sigma,\sigma'} \psi_{\sigma'}(x), \tag{2.24}$$

and $x = (\mathbf{r}, \tau)$, $\sigma \in \{\uparrow, \downarrow\}$, $\psi_\sigma(x)$ ($\psi^\dagger_\sigma(x)$) annihilates (creates) a particle with spin σ at x and σ^z is a Pauli matrix. Eq. (2.24) can be rewritten as

$$S^z(x) = \frac{1}{2}\Big(\psi^\dagger_\uparrow(x)\psi_\uparrow(x) - \psi^\dagger_\downarrow(x)\psi_\downarrow(x)\Big). \tag{2.25}$$

We then substitute (2.25) in (2.23) to obtain

$$\begin{aligned}\chi_L(x,x') = \frac{1}{4}\Big[&\langle \mathcal{T}\psi^\dagger_\uparrow(x)\psi_\uparrow(x)\psi^\dagger_\uparrow(x')\psi_\uparrow(x')\rangle - \langle \mathcal{T}\psi^\dagger_\uparrow(x)\psi_\uparrow(x)\psi^\dagger_\downarrow(x')\psi_\downarrow(x')\rangle \\ &-\langle \mathcal{T}\psi^\dagger_\downarrow(x)\psi_\downarrow(x)\psi^\dagger_\uparrow(x')\psi_\uparrow(x')\rangle + \langle \mathcal{T}\psi^\dagger_\downarrow(x)\psi_\downarrow(x)\psi^\dagger_\downarrow(x')\psi_\downarrow(x')\rangle\Big] \\ = \frac{1}{2}\Big[&\langle \mathcal{T}\psi^\dagger_\uparrow(x)\psi_\uparrow(x)\psi^\dagger_\uparrow(x')\psi_\uparrow(x')\rangle - \langle \mathcal{T}\psi^\dagger_\uparrow(x)\psi_\uparrow(x)\psi^\dagger_\downarrow(x')\psi_\downarrow(x')\rangle\Big],\end{aligned} \tag{2.26}$$

which can be written as

$$\chi_L(x,x') = \frac{1}{2}\Big[\langle \mathcal{T}n_\uparrow(x)n_\uparrow(x')\rangle - \langle \mathcal{T}n_\uparrow(x)n_\downarrow(x')\rangle\Big]. \tag{2.27}$$

We note the similarity of Eq. (2.27) to the charge susceptibility defined by:

$$\chi_c(x,x') = 2\Big[\langle \mathcal{T}n_\uparrow(x)n_\uparrow(x')\rangle + \langle \mathcal{T}n_\uparrow(x)n_\downarrow(x')\rangle\Big], \tag{2.28}$$

We then conclude that the diagrammatic representations of the longitudinal spin susceptibility and the density-density susceptibility are the same in the sense of diagrams' topologies (see Fig. 2.4). One can also define reducible and irreducible susceptibility diagrams similarly to the self-energy diagrams. The reducible susceptibility diagrams are those which can be split into two connected susceptibility diagrams by cutting one of the wavy lines.

We emphasize that the sign of terms arising from $\langle \mathcal{T}n_\uparrow(x)n_\downarrow(x')\rangle$ are negative. It means that to compute χ_L we should separate the diagrams in the expansion into two

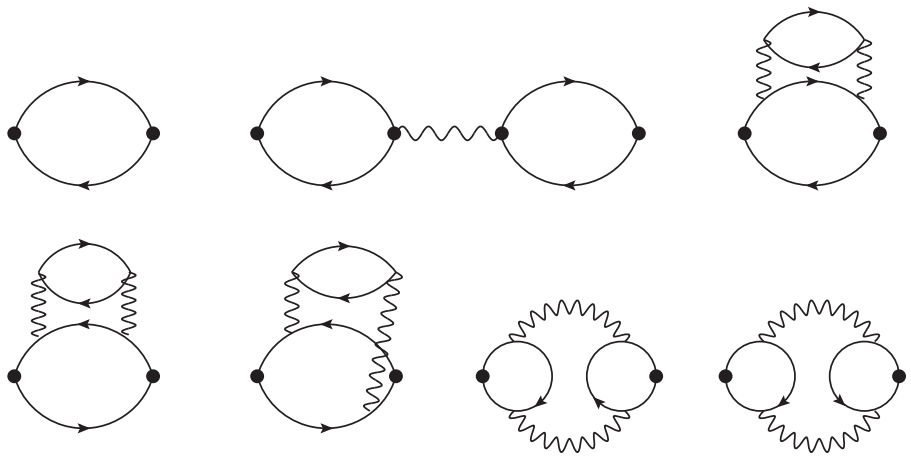

Figure 2.4: Diagrammatic expansion of the charge susceptibility or longitudinal spin susceptibility up to second order for the single-band Hubbard model. Each loop has a well-defined spin and two connected loops should have opposite spins. We do not show the diagrams with tadpole insertions and reducible second order ones.

groups:

1. $g_{\uparrow\uparrow}$: The set of diagrams arising from the $\langle \mathcal{T} n_\uparrow(x) n_\uparrow(x') \rangle$ term.

2. $g_{\uparrow\downarrow}$: The set of diagrams arising from the $\langle \mathcal{T} n_\uparrow(x) n_\downarrow(x') \rangle$ term.

To construct $g_{\uparrow\uparrow}$ and $g_{\uparrow\downarrow}$ for the Hubbard interaction one should follow a simple procedure:

1. Generate the set S of (irreducible and reducible) diagrams considering the Feynman rules for the Hubbard Hamiltonian. Note that in all the diagrams the principle loop has spin up.

2. For each diagram D of order m in S count the number of spin up and spin down fermionic lines and call them $N_\uparrow$ and $N_\downarrow$, respectively.

   (a) If $N_\uparrow = N_\downarrow + 2 = m + 2$ the diagram D belongs to $g_{\uparrow\uparrow}$.

   (b) If $N_\uparrow = N_\downarrow = m + 1$ the diagram D belongs to $g_{\uparrow\downarrow}$.

Then the longitudinal spin susceptibility is calculated by:

$$\chi_L = \frac{1}{2}\Big(\chi^{\uparrow\uparrow} - \chi^{\uparrow\downarrow}\Big), \tag{2.29}$$

where $\chi^{\uparrow\uparrow}$ and $\chi^{\uparrow\downarrow}$ are calculated from the diagrams in $g_{\uparrow\uparrow}$ and $g_{\uparrow\downarrow}$, respectively. Similarly the charge susceptibility is

$$\chi_c = 2\Big(\chi^{\uparrow\uparrow} + \chi^{\uparrow\downarrow}\Big). \tag{2.30}$$

2.4.2 Transverse spin susceptibility

By definition the transverse spin susceptibility is given by [9]

$$\chi_T(x, x') = \langle \mathcal{T}_\tau S^+(x) S^-(x') \rangle, \tag{2.31}$$

where $S^+(x)$ and $S^-(x')$ are spin-raising and spin-lowering operators which are defined by

$$S^+(x) = \psi^\dagger_\uparrow(x)\psi_\downarrow(x), \tag{2.32}$$

and

$$S^-(x) = \psi^\dagger_\downarrow(x)\psi_\uparrow(x), \tag{2.33}$$

where $x = (\mathbf{r}, \tau)$. We first replace (2.32) and (2.33) in (2.31):

$$\chi_T(x, x') = \langle \mathcal{T}\psi^\dagger_\uparrow(x)\psi_\downarrow(x)\psi^\dagger_\downarrow(x')\psi_\uparrow(x') \rangle \tag{2.34}$$

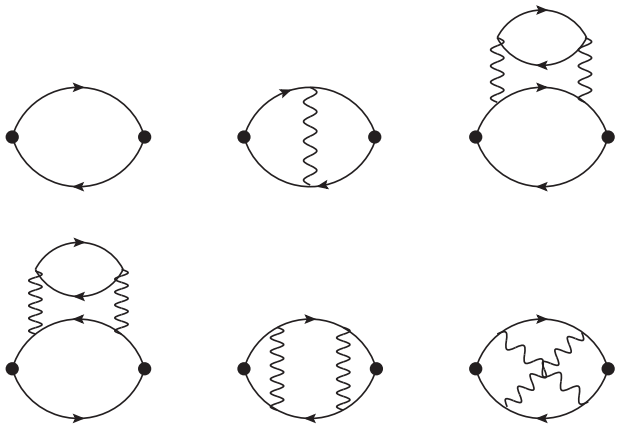

Figure 2.5: Diagrammatic expansion of the transverse spin susceptibility up to second order for the single-band Hubbard model. We do not show the diagrams with tadpole insertions. In the principle loop the particle line is spin down and the hole line is spin down.

The last step is to follow the S-matrix approach and apply Wick's theorem to establish the perturbative series expansion. The diagrammatic expansion of the transverse spin susceptibility up to second order is presented in Fig. 2.5, neglecting all the diagrams with tadpole insertions. We note that the diagrams' topologies for the transverse spin susceptibility are different from those of the longitudinal spin susceptibility, however, the Hubbard Hamiltonian is invariant under spin-rotations [10, 11], therefore, $\chi_T = 2\chi_L$.

2.5 Random phase and T-matrix approximations

In the random phase approximation (RPA) [12, 13] one considers an infinite subseries of diagrams, shown in Figure 2.6, to approximate charge and longitudinal spin susceptibilities. Thus, in the RPA scheme we have:

$$\chi_c^{\mathrm{RPA}}(i\Omega_m, \mathbf{q}) = 2\frac{\Pi_0(i\Omega_m, \mathbf{q})}{1 + U\Pi_0(i\Omega_m, \mathbf{q})}, \tag{2.35}$$

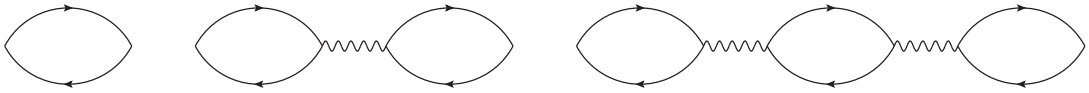

Figure 2.6: Diagrammatic expansion of the longitudinal spin and charge susceptibility functions up to second order for the single-band Hubbard model in the RPA scheme.

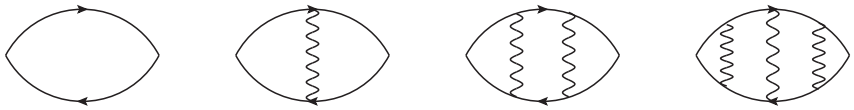

Figure 2.7: Diagrammatic expansion of the transverse spin susceptibility up to third order for the single-band Hubbard model in the TMA scheme.

and

$$\chi_L^{\mathrm{RPA}}(i\Omega_m, \mathbf{q}) = \frac{1}{2}\frac{\Pi_0(i\Omega_m, \mathbf{q})}{1 - U\Pi_0(i\Omega_m, \mathbf{q})}, \tag{2.36}$$

where $i\Omega_m$ is the external (bosonic) Matsubara frequency, $\mathbf{q}$ is the external momenta and

$$\Pi_0(i\Omega_m, \mathbf{q}) = -\frac{1}{\beta}\sum_{\nu_n}\sum_{\mathbf{k}} \mathcal{G}_0(i\nu_n, \mathbf{k})\mathcal{G}_0(i\nu_n + i\Omega_m, \mathbf{k} + \mathbf{q}) \tag{2.37}$$

is the first diagram in Fig. 2.6. In order to approximate the transverse spin susceptibility the T-matrix approximation (TMA) [14, 15] is commonly used. In this scheme one takes ladder diagrams into account (See Figure 2.7). A straightforward calculation shows that

$$\chi_T^{\mathrm{TMA}}(i\Omega_m, \mathbf{q}) = \frac{\Pi_0(i\Omega_m, \mathbf{q})}{1 - U\Pi_0(i\Omega_m, \mathbf{q})}. \tag{2.38}$$

Bibliography

[1] J. Hubbard and B. H. Flowers. Electron correlations in narrow energy bands. *Series A. Math. and Phys. Sci.*, 276, 1963.

[2] Martin C. Gutzwiller. Effect of Correlation on the Ferromagnetism of Transition Metals. *Phys. Rev. Lett.*, 10:159–162, 1963.

[3] Junjiro Kanamori. Electron Correlation and Ferromagnetism of Transition Metals. *Prog. Theo. Phys.*, 30:275–289, 1963.

[4] M. V. Sadovskii. *Diagrammatics: Lectures on Selected Problems in Condensed Matter Theory*. World Scientific, 2006.

[5] G. D. Mahan. *Many-particle Physics*. Plenum Press, New York, 1981.

[6] Kris Van Houcke, Evgeny Kozik, N. Prokof'ev, and B. Svistunov. Diagrammatic Monte Carlo. *Phys. Proc.*, 6:95–105, 2010.

[7] V. Zlatić, B. Horvatić, B. Dolički, S. Grabowski, P. Entel, and K.-D. Schotte. Perturbation expansion for the two-dimensional Hubbard model. *Phys. Rev. B*, 63:035104, 2000.

[8] Cornelia Hille, Fabian B. Kugler, Christian J. Eckhardt, Yuan-Yao He, Anna Kauch, Carsten Honerkamp, Alessandro Toschi, and Sabine Andergassen. *arXiv:2002.02733*, 2020.

[9] N. Bulut, D. J. Scalapino, and S. R. White. Spin-fluctuation mediated interaction in the two-dimensional Hubbard model. *Phys. C: Superconduc.*, 246(1):85–94, 1995.

[10] J. J. Vicente Alvarez, C. A. Balseiro, and H. A. Ceccatto. Spin- and charge-rotation invariant approach to the Hubbard model. *Phys. Rev. B*, 54:11207–11212, 1996.

[11] Atsushi Masumizu and Kiyoshi Sogo. Ward-Takahashi relations for SO(4) symmetry in the Hubbard model. *Phys. Rev. B*, 72:115107, 2005.

[12] David Bohm and David Pines. A Collective Description of Electron Interactions. I. Magnetic Interactions. *Phys. Rev.*, 82:625–634, 1951.

[13] David Bohm and David Pines. A Collective Description of Electron Interactions: III. Coulomb Interactions in a Degenerate Electron Gas. *Phys. Rev.*, 92:609–625, 1953.

[14] Hidetoshi Fukuyama and Yasumasa Hasegawa. t-Matrix Approximation to Two-Dimensional Hubbard Model. *Prog. Theo. Phys. Suppl.*, 101:441–452, 1990.

[15] Jan Gukelberger, Li Huang, and Philipp Werner. On the dangers of partial diagrammatic summations: Benchmarks for the two-dimensional Hubbard model in the weak-coupling regime. *Phys. Rev. B*, 91:235114, 2015.

Chapter 3

Algorithmic Matsubara integration for Hubbard-like models

We aim to use perturbation theory via the Feynman diagrammatic formalism to evaluate the self-energy and susceptibility functions of the Hubbard model in frequency-momentum space. To do so, one, in principle, needs to take the following steps:

1. Construct the diagrammatic expansion up to some truncation order.

2. Translate each diagram to its corresponding mathematical expression by using the Feynman rules.

3. Evaluate the frequency and momenta sums of each diagram.

Although it, in principle, is a trivial task, it is in practice an extremely challenging procedure. For this reason in this chapter we only focus on the analytic evaluation of the Matsubara sums for a given Feynman diagram.

The Matsubara sums in Matsubara frequency (or equivalently in imaginary time) space are typically evaluated by using Monte Carlo methods [1–4]. Then, in order to provide the result in real frequency space numerical methods, which are mathe-

matically ill-defined, have to be used. We completely resolve this issue introducing a powerful systematic machinery, which we call algorithmic Matsubara integration (AMI), based upon the residue theorem, to construct an analytic result for the frequency summations of a given Feynman diagram. In order to clarify the core idea of the AMI procedure we take the bare bubble as a simple example:

$$\Pi_0(i\Omega, \mathbf{q}) = -2T \int \frac{d\mathbf{k}_1}{(2\pi)^2} \sum_{\nu_1} \frac{1}{i\nu_1 - \epsilon(\mathbf{k}_1)} \frac{1}{i\nu_1 + i\Omega - \epsilon(\mathbf{k}_1 + \mathbf{q})}, \tag{3.1}$$

where $i\nu_1$ and $i\Omega$ are (internal) fermionic and (external) bosonic Matsubara frequencies, respectively, T is the temperature, $\mathbf{k}_1$ and $\mathbf{q}$ represent internal and external momenta, respectively, and $\epsilon(\mathbf{k})$ is the free particle energy. We rewrite (3.1) as

$$\Pi_0(i\Omega, \mathbf{q}) = -2 \int \frac{d\mathbf{k}_1}{(2\pi)^2} I_0(i\Omega, \mathbf{k}_1, \mathbf{q}), \tag{3.2}$$

with

$$I_0(i\Omega, \mathbf{k}_1, \mathbf{q}) = T \sum_{\nu_1} \frac{1}{i\nu_1 - \epsilon(\mathbf{k}_1)} \frac{1}{i\nu_1 + i\Omega - \epsilon(\mathbf{k}_1 + \mathbf{q})}. \tag{3.3}$$

This summation can be evaluated analytically using the residue theorem. For a function $h(\nu)$, where ν is a fermionic frequency we have

$$\sum_{\nu} h(i\nu) = \beta \sum_{\{z_0\}} \mathrm{Res}[f(z)h(z)]_{z_0}, \tag{3.4}$$

where $\{z_0\}$ are the poles of h with respect to $i\nu$, f is the Fermi distribution function and β is the inverse temperature (See Appendix A for proof). In fact, Eq. (3.4) reduces the infinite summation over the fermionic Matsubara frequencies to a finite summation with r terms where r is the total numbers of poles with respect to the

frequency $i\nu$. Applying (3.4) and doing straightforward algebra we obtain the full analytic expression of I_0:

$$I_0(i\Omega, \mathbf{k}_1, \mathbf{q}) = \frac{f[\epsilon(\mathbf{k}_1)] - f[\epsilon(\mathbf{k}_1 + \mathbf{q})]}{i\Omega + \epsilon(\mathbf{k}_1) - \epsilon(\mathbf{k}_1 + \mathbf{q})}. \tag{3.5}$$

Note that Eq. (3.5) is model independent and is valid for any time-independent interactive system. The final result for polarization bubble is obtained:

$$\Pi_0(i\Omega, \mathbf{q}) = -2 \int \frac{d\mathbf{k}_1}{(2\pi)^2} \frac{f[\epsilon(\mathbf{k}_1)] - f[\epsilon(\mathbf{k}_1 + \mathbf{q})]}{i\Omega + \epsilon(\mathbf{k}_1) - \epsilon(\mathbf{k}_1 + \mathbf{q})}. \tag{3.6}$$

Therefore, the result of AMI is fully analytic and can be evaluated exactly (up to machine precision) with no truncation error due to introducing a cut-off frequency, upon which one can impose a true analytic continuation to the real-frequency axis (see Appendix B for an instructive example). Our goal in this chapter is to provide an automated machinery to evaluate the Matsubara sums of a given Feynman diagram and return a full symbolic result similar to what we showed for the bare bubble. Since in general we deal with a finite number of sums over independent Matsubara frequencies, doing so requires an iterated application of the residue theorem which we shall discuss in detail in the following sections.

In the rest of this chapter we reproduce Ref. [5], Amir Taheridehkordi, Stephanie H. Curnoe, and James P. F. LeBlanc, doi: 10.1103/PhysRevB.99.035120; License number: RNP/20/OCT/031576; reproduced with kind permission of the publishers of Physical Review B. The manuscript is followed by Supplemental Material.

3.1 Abstract

We present an algorithm to evaluate Matsubara sums for Feynman diagrams comprised of bare Green's functions with single-band dispersions and local U Hubbard interaction vertices. The algorithm provides an exact construction of the analytic result for the frequency integrals of a diagram that can then be evaluated for all parameters U, temperature T, chemical potential μ, external frequencies and internal/external momenta. This method allows for symbolic analytic continuation of results to the real frequency axis, avoiding any ill-posed numerical procedure. This method can also be used to simultaneously evaluate diagrams throughout the entire T-U-μ phase space of Hubbard-like models even in the $T = 0$ limit at minimal computational expense.

3.2 Introduction

The Hubbard model [6] is a cornerstone of correlated electron physics and plays an important role as a testbed for the development of numerical algorithms. Among modern numerical tools, Diagrammatic Monte Carlo (DiagMC) is a powerful technique which performs integrals arising from perturbative expansions by sampling classes of connected Feynman diagrams [1–4]. Other algorithms have been developed from expansions around non-perturbative dynamical mean-field theory, [7–9] as well as so-called 'bold' extensions to DiagMC with a variety of possible of resummation schemes. [10, 11] However, it was recently shown [12, 13] that the resummation of the skeleton Feynman diagrammatic series for systems with the Hubbard interaction will lead to a false convergence towards an unphysical branch due to the Riemann series theorem at strong interactions, while the series based on bare Green's functions always converges to the expected physical result. [12] As a result, expressing the perturbation series in terms of bare Green's functions (and bare vertices) might be

preferable.

In the case of Hubbard-like models, [6] since each bare vertex is unstructured (U) in principal one needs only to compute the series of integrals over internal spatial (momentum) and time (frequency, commonly computed as a sum over Matsubara frequencies) variables for each diagram. Despite the conceptual simplicity of this proposal, in practice the problem remains a challenge. One difficulty lies in the factorial scaling of the number of diagrams one must sample as the interaction order increases. [4,14,15] Another is the poor convergence of sums over Matsubara frequencies, since the set of Matsubara frequencies [$i\nu_n = i\frac{\pi}{\beta}(2n+1)$ or $i\frac{\pi}{\beta}(2n)$ for fermions and bosons respectively] compresses as the temperature $T = 1/\beta$ decreases. Worse still is that numerical results by necessity express external lines of the Feynman diagrams in terms of Matsubara frequencies. The numerical process of analytic continuation of Matsubara frequencies to real frequencies is ill-posed, and while procedures such as maximum entropy inversion or Padé approximants have become standard and codes to implement these procedures are widely available, [16–19] the problem of analytic continuation remains a roadblock to providing reliable theoretical results to correlated many-body problems.

In this paper we propose a method which we call Algorithmic Matsubara Integration (AMI) in which we utilize the residue theorem to compute summations over independent Matsubara frequencies. The result of the algorithm is an analytic expression for the temporal integrals of a diagram of arbitrary order in terms of internal and external momenta and external Matsubara frequencies, upon which one can impose a true analytic continuation $i\omega_n \to \omega + i0^+$. AMI can be applied to any Hubbard-like model with an arbitrary dimensionality. To demonstrate the utility of this method, we provide examples of the AMI result which requires a choice of dispersion and dimensionality. For simplicity we use a nearest neighbor tight-binding dispersion on a

square lattice which allows us to comment on the scaling of computational cost with complexity of the integrand (*i.e.* expansion order).

Algorithm: DiagMC typically samples the entire space of diagram topologies as well as sampling over internal variables such as a set of momenta $\{k_n\} = k_1, k_2, ..., k_n$ and a set of frequencies $\{\nu_n\} = \nu_1, \nu_2, ..., \nu_n$. [1] Our aim is to reduce the space of sampling for Monte-Carlo methods from $\{k_n, \nu_n\} \to \{k_n\}$ by algorithmic evaluation of the analytic result of the $\{\nu_n\}$ integrals. By evaluating the sums over Matsubara frequencies algorithmically we completely remove the need to probe the frequency (time) configuration space.

Making no assumptions about the topology of the diagram, the general form of a diagram can be written as

$$\frac{U^{n_v}}{\beta^n} \sum_{\{k_n\}} \sum_{\{\nu_n\}} \prod_{j=1}^{N} G^j(\epsilon^j, X^j) = U^{n_v} \sum_{\{k_n\}} I^{(n)}, \tag{3.7}$$

$$I^{(n)} = \frac{1}{\beta^n} \sum_{\{\nu_n\}} \prod_{j=1}^{N} G^j(\epsilon^j, X^j), \tag{3.8}$$

where n_v is the order (the number of vertices) of the diagram, n is the number of summations over Matsubara frequencies $\{\nu_n\}$ and internal momenta $\{k_n\}$, and N is the number of internal lines representing bare Green's functions $G(\epsilon, X)$. The bare Green's function of the jth internal line is

$$G^j(\epsilon^j, X^j) = \frac{1}{X^j - \epsilon^j}, \tag{3.9}$$

where X^j is the frequency and $\epsilon^j = \epsilon^j(k_j)$ is the free particle dispersion. Constraints derived from energy and momentum conservation at each vertex allow us to express these quantities as linear combinations of internal $\{\nu_n, k_n\}$ and external $\{\nu_\gamma, k_\gamma\}$ frequencies and momenta, where $k_j = \sum_{\ell=1}^{m} \alpha_\ell^j k_\ell$, $X^j = \sum_{\ell=1}^{m} i\alpha_\ell^j \nu_\ell$, and $\gamma = m - n$ is

the number of unconstrained external frequencies. The coefficients α_ℓ^j are numbers which have only three possible values: zero, plus one or minus one. This allows us to represent G^j as an array of length $m+1$ of the form

$$G^j(X^j) \to [\epsilon^j, \vec{\alpha}^j], \tag{3.10}$$

where $\vec{\alpha}^j = (\alpha_1^j, ..., \alpha_m^j)$. Given our array representation of each G^j, we construct a nested array to represent the product of G^j which appears in Eq. (3.8),

$$\prod_{j=1}^{N} G^j(\epsilon^j, X^j) \to \Big[[\epsilon^1, \vec{\alpha}^1]; [\epsilon^2, \vec{\alpha}^2]; ...; [\epsilon^N, \vec{\alpha}^N]\Big]. \tag{3.11}$$

The size of this array is $N \times (m+1)$. As we shall show, this representation carries all the information we need to compute the summations in Eq. (3.8).

To begin the algorithm, we subdivide the original problem to the summation over a single frequency ν_p, and the remaining frequencies $\nu_n \neq \nu_p$,

$$I^{(n)} = \sum_{\{\nu_n\}, \nu_n \neq \nu_p} I_p, \tag{3.12}$$

$$I_p = \sum_{\nu_p} \prod_{j=1}^{N} G^j(\epsilon^j, X_m^j). \tag{3.13}$$

Central to computing Eq. (3.13) is the identification of the set of simple poles of the Green's functions. The pole of the jth Green's function with respect to the frequency ν_p exists so long as the coefficient α_p^j is non-zero, and is given by

$$z_p^{(j)} = -\alpha_p^j(-\epsilon^j + \sum_{\ell=1, \ell\neq p}^{m} i\alpha_\ell^j \nu_\ell) \quad \text{for} \quad \alpha_p^j \neq 0. \tag{3.14}$$

The number of simple poles for ν_p is $r_p = \sum_{j=i}^{N} |\alpha_p^i|$, which occur in r_p of N total Green's functions in the product of Eq. (3.13). We label these r_p Green's functions

as G^{i_1}, G^{i_2}, ..., $G^{i_{r_p}}$, and the set of simple poles will be denoted by $\{z_p^{(i_\ell)}\}_{\ell=1,2,...,r_p}$. Assuming all $z_p^{(i_\ell)}$ poles to be simple, the residue of each is

$$\alpha_p^{i_\ell} \prod_{j \neq i_\ell} G^j(\alpha_p^j z_p^{(i_\ell)} + \sum_{\ell \neq p} i\alpha_\ell^j \nu_\ell). \tag{3.15}$$

Note the sign $\alpha_p^{i_\ell}$ that is attached to this result.

To calculate the summation over the fermionic frequency ν_p in Eq. (3.13) we use the residue theorem,

$$\sum_{\nu_p} h(i\nu_p) = \beta \sum_{z_p} f(z_p) \mathrm{Res}[h(z)]_{z_p}, \tag{3.16}$$

where $f(z)$ is the Fermi function and z_p are the poles of $h(z)$. Applying (3.16) to the summation (3.13) and using (3.15), we find the result:

$$\begin{aligned} I_p = \alpha_p^{i_1} \beta f(z_p^{(i_1)}) \prod_{j \neq i_1} G^j(\alpha_p^j z_p^{(i_1)} + \sum_{\ell \neq p} i\alpha_\ell^j \nu_\ell) + \alpha_p^{i_2} \beta f(z_p^{(i_2)}) \prod_{j \neq i_2} G^j(\alpha_p^j z_p^{(i_2)} + \sum_{\ell \neq p} i\alpha_\ell^j \nu_\ell) \\ + ... + \alpha_p^{i_{r_p}} \beta f(z_p^{(i_{r_p})}) \prod_{j \neq i_{r_p}} G^j(\alpha_p^j z_p^{(i_{r_p})} + \sum_{\ell \neq p} i\alpha_\ell^j \nu_\ell). \end{aligned} \tag{3.17}$$

The Fermi function is evaluated as

$$f(z_p^{(i_\ell)}) = \frac{1}{\sigma \exp(-\beta \alpha_p^{i_\ell} \epsilon^{i_\ell}) + 1}, \tag{3.18}$$

where σ is a sign given by

$$\sigma(z_p^{i_\ell}) = \exp(i\beta \sum_{\ell \neq p} \alpha_\ell^{i_\ell} \nu_\ell), \tag{3.19}$$

that is, $\sigma = -1$ if there are an odd number of fermionic frequencies in the sum over

ℓ, otherwise $\sigma = 1$. Therefore $f(z_p^{(i_\ell)})$ is independent of Matsubara frequencies and only depends on the real energy dispersion, though its character might switch from fermionic to bosonic.

We have thus evaluated (3.13), a single frequency summation. There are r_p terms in the result, and each term in this result contains a product of $N-1$ Green's functions, which may be represented as a $(N-1)\times(m+1)$ dimensional array in the form (3.11). These arrays may be arranged into a single nested array of size $r_p \times (N-1)\times(m+1)$.

We make use of this result to calculate *all* of the summations in Eq. (3.8) using a recursive procedure. Without loss of generality we (arbitrarily) label the independent frequencies in the diagram as $\nu_1, \nu_2, \ldots \nu_n$, and perform the summations in this order. Each step of the procedure corresponds to the evaluation of one frequency summation. At the beginning of the procedure, the Feynman diagram that is to be evaluated is represented as a $1 \times N \times (m+1)$ dimensional array from which the poles of ν_1 are extracted. After the first summation is computed using (3.17), the result is stored in a $r_1 \times (N-1) \times (m+1)$ dimensional array, and the poles of ν_2 in this result are extracted. Subsequent steps will reduce the second dimension by one on each step, but the first dimension will increase according to the number of poles. When all summations have been completed all that remains are functions defined by the γ external frequencies.

To implement this procedure computationally we define the following objects:

- the arrays R_p representing the configurations of Green's functions after the pth summation (described above),
- the sets of poles P_p for ν_p in the configuration of Green's functions represented by R_{p-1},
- the set of signs S_p of the residues for each pole (the $\alpha_p^{i_\ell}$ in Eq. (3.15)).

The array of poles corresponding to ν_p has entries

$$P_p = [P_p^{(1)}, P_p^{(2)}, ..., P_p^{(r_{(p-1)})}], \tag{3.20}$$

with

$$P_p^{(\ell)} = [z_{p,\ell}^{(i_1)}, z_{p,\ell}^{(i_2)}, ..., z_{p,\ell}^{(i_{r_\ell})}]. \tag{3.21}$$

We note that $P_p^{(\ell)}$ is the array of poles for ν_p in the residue of the ℓth pole for ν_{p-1} stored in the previous configuration of Green's functions, R_{p-1}. Similarly we have an array of signs with the same dimensions as P_p:

$$S_p = [S_p^{(1)}, S_p^{(2)}, ..., S_p^{(r_{(p-1)})}], \tag{3.22}$$

with

$$S_p^{(\ell)} = [\alpha_{p,\ell}^{(i_1)}, \alpha_{p,\ell}^{(i_2)}, ..., \alpha_{p,\ell}^{(i_{r_\ell})}]. \tag{3.23}$$

where $\alpha_{p,\ell}$ are the nonzero coefficients of ν_p of the previous configuration of Green's functions, R_{p-1}.

Using these arrays, the full analytic result for Eq. (3.8) is given by

$$I^{(n)} = \frac{1}{\beta^n} \sum_{\{\nu_n\}} \prod_{j=1}^{N} G^j(\epsilon^j, X_m^j) = K \cdot R_n, \tag{3.24}$$

where

$$K = (S_1 * f(P_1)) \times (S_2 * f(P_2)) \times ... \times (S_n * f(P_n)). \tag{3.25}$$

In this expression, $f(P_p)$ is the Fermi function of an array with elements given by

$$[f(P_p)]^i_\ell = f(z^{(i)}_{p,\ell}), \tag{3.26}$$

and the operations '$*$', '$\times$', and '$\cdot$' are defined by

$$\begin{aligned}(C * D)^j_i &= C^j_i D^j_i \equiv G^j_i, \\ (G \times H)^j_i &= G_i H^j_i, \\ H \cdot C &= \sum_i H_i C_i.\end{aligned}$$

Equations (3.24) and (3.25) are primary results of this paper. These equations are obtained under the presumption that all of the poles are simple poles. Poles with higher multiplicity are equivalent to multiple simple poles and therefore the result of Eq. (3.24) holds even when poles with higher multiplicity arise. However, it is not the ideal representation since upon evaluation one will find cancelling divergent terms which sum to non-zero values, causing numerical instability. This problem can be avoided by generalizing for poles with multiplicity M. If $h(z)$ has a pole of order M at $z = z_0$, then the residue is given by

$$Res[h(z_0)] = \frac{1}{(M-1)!} \lim_{z \to z_0} \frac{d^{M-1}}{dz^{M-1}} \Big\{ (z - z_0)^M h(z) \Big\}. \tag{3.27}$$

In order to analytically evaluate arbitrary order derivatives, we employ the method of automatic differentiation which requires only knowledge of the first derivative and repeated application of chain rules. The first derivative with respect to $i\nu_p$ of the

multiplication of N Green's function is given via chain rule as

$$\frac{d}{d(i\nu_p)}(\prod_{j=1}^{N} G^j(\epsilon^j, X_m^j)) = \sum_{i=1}^{N} \frac{dG^i}{d(i\nu_p)} \prod_{j\neq i} G^j(\epsilon^j, X_m^j). \tag{3.28}$$

The first derivative of one of the Green's function with respect to $i\nu_p$ in the array representation can then be performed by returning two Green's functions,

$$\frac{dG^i(\epsilon^i, X_m^i)}{d(i\nu_p)} \to \left[[\epsilon^i, X_m^i]; [-\alpha_p^i \epsilon^i, \alpha_p^i X_m^i]\right]. \tag{3.29}$$

The $(M-1)$th order derivative can be computed by iterating (3.28). We therefore are able to express the residue for poles of $i\nu_p$ with any multiplicity using our symbolic representation. The only significant difference is that in the presence of multiple poles the entries of the S array are $\pm\frac{1}{(M-1)!}$ instead of only ± 1. The structures of P and R arrays remain the same but with additional terms arising from the chain rules, and Eqs. (3.24) and (3.25) remain valid to construct the final result.

We emphasize that since the result is symbolic in the set of yet-defined external frequencies $\{\nu_\gamma\}$, at the final step one can replace $i\nu_\gamma \to \nu_\gamma + i0^+$ just as in a standard analytic continuation. This eliminates the need for ill-posed numerical methods of analytic continuation in diagrammatics of Hubbard-like models. The method requires both the time to construct the solution, t_c, and the evaluation time, t_e, for each set, γ, of external variables. We therefore expect the scaling will go as $\gamma t_e + t_c$ where t_c is typically larger than t_e.

Examples: The AMI result for a Feynman diagram is valid for any Hubbard-like model and is not dependent on the lattice dimensionality. Here, in order to illustrate the utility of AMI we evaluate the temporal integrals of 3 diagrams of increasing complexity shown in the left hand column of Fig. 3.1. We assume a 2D square lattice

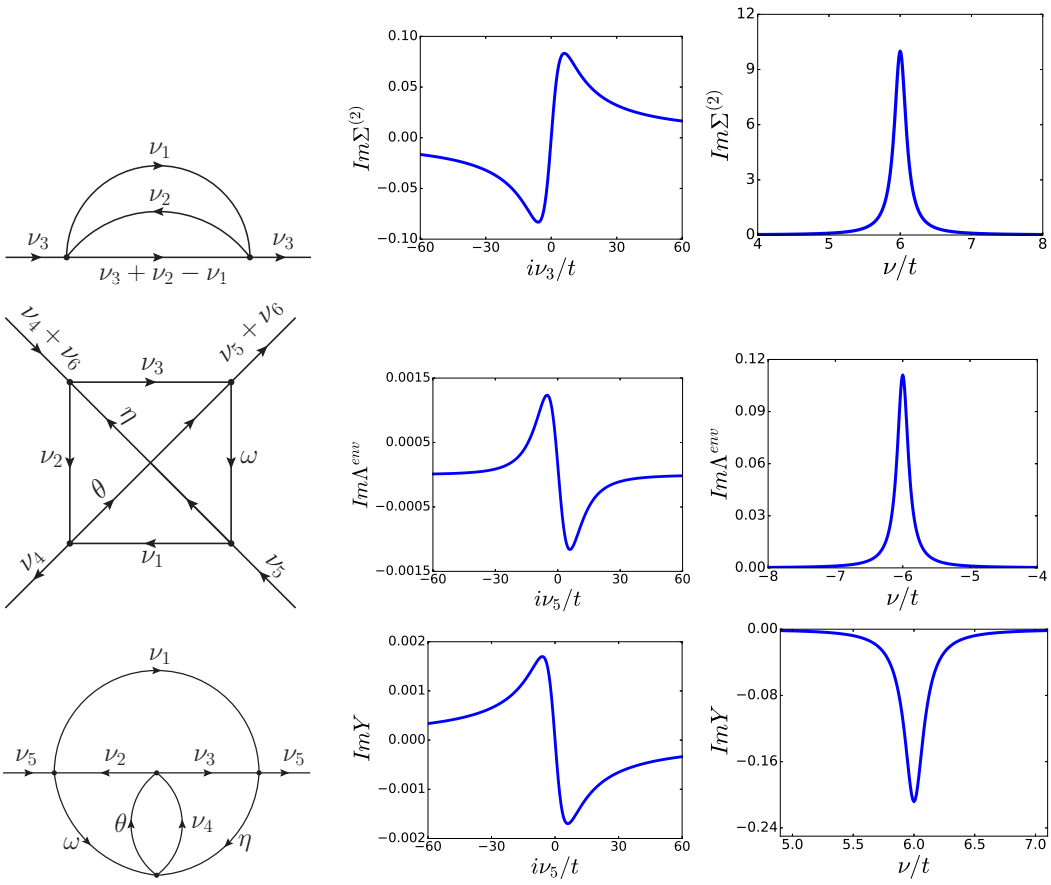

Figure 3.1: *First column*: Feynman diagram; *Second column*: Imaginary part vs. Matsubara frequency; *Third column* Imaginary part vs. real frequency. Data for $\beta t = 10$, and $\mu/t = 0$ (half-filled) for a 2D square lattice tight-binding dispersion. *Top Row*: $\Sigma^{(2)}$ at crystal momenta $\vec{k}_1 = (0,0)$, $\vec{k}_2 = \vec{k}_3 = (\frac{\pi}{a}, \frac{\pi}{3a})$; *Middle Row*: Λ^{env} at crystal momenta $\vec{k}_1 = (0,0)$, $\vec{k}_2 = \vec{k}_3 = \vec{k}_4 = \vec{k}_5 = \vec{k}_6 = (\frac{\pi}{a}, \frac{\pi}{3a})$ with $\nu_4 = \frac{\pi}{\beta}$ and $\nu_6 = 0$ in Matsubara space (second column) and $\nu_4 = \nu_6 = 0$ on the real frequency axis (third column); *Bottom Row*: Y at crystal momenta $\vec{k}_1 = (0,0)$, $\vec{k}_2 = \vec{k}_3 = \vec{k}_4 = \vec{k}_5 = (\frac{\pi}{a}, \frac{\pi}{3a})$. We set $\delta = 0.1$ in the analytic continuation process $i\nu_n \to \nu + i\delta$.

with tight-binding dispersion $\epsilon_{\vec{k}} = -2t(\cos(k_x a) + \cos(k_y a)) - \mu$ where t is the hopping amplitude, a is the lattice constant and $\mu = 0$ for simplicity. The three diagrams are: $\Sigma^{(2)}$, a second-order self energy diagram with a single external line; Λ^{env} a highly connected fourth-order irreducible diagram [20] with multiple external frequencies and three independent Matsubara frequencies; Y a fourth-order example including four independent frequencies. The diagrams are translated, save for factors of U^{n_v}, as

$$\Sigma^{(2)} = \frac{1}{\beta^2} \sum_{\nu_1,\nu_2} G(i\nu_1)G(i\nu_2)G(i\nu_3 + i\nu_2 - i\nu_1), \tag{3.30}$$

$$\Lambda^{env} = \frac{1}{\beta^3} \sum_{\nu_1,\nu_2,\nu_3} G(i\nu_1)G(i\nu_2)G(i\nu_3)G(i\omega)G(i\eta)G(i\theta), \tag{3.31}$$

$$Y = \frac{1}{\beta^4} \sum_{\{\nu_i\}_{i=1}^4} G(i\nu_1)G(i\nu_2)G(i\nu_3)G(i\nu_4)G(i\omega)G(i\theta)G(i\eta). \tag{3.32}$$

The AMI algorithm produces symbolic results in the form of P_p, S_p and R_n (see Supplemental Material [21] for explicit forms) which are used to evaluate each diagram,

$$\Sigma^{(2)} \to (S_1 * f(P_1)) \times (S_2 * f(P_2)) \cdot R_2^{\Sigma} \tag{3.33}$$

$$\Lambda^{env} \to (S_1 * f(P_1)) \times (S_2 * f(P_2)) \times (S_3 * f(P_3)) \cdot R_3^{\Lambda} \tag{3.34}$$

$$\begin{aligned} Y \quad \to (S_1 * f(P_1)) \times (S_2 * f(P_2)) \times (S_3 * f(P_3)) \times \\ (S_4 * f(P_4)) \cdot R_4^{Y} \end{aligned} \tag{3.35}$$

There are 4, 32, and 82 terms for R_2^{Σ}, R_3^{Λ} and R_4^{Y} respectively. These are then evaluated for a choice of internal and external momenta $\{k_n\}$ and external frequencies $\{\nu_\gamma\}$, on either the Matsubara axis or on the real axis via $i\nu_\gamma \to \nu_\gamma + i\delta$ for a choice of small δ. Results are shown in Fig. 3.1 on both the Matsubara and real frequency axes for specific choices of $\{k_n\}$ (which would be integrated to evaluate the full diagram).

Computing higher order Feynman graphs using AMI is straightforward. We provide in the Supplementary Information [21] a particularly complex example of a ninth-order diagram which contains 337982 terms assuming simple poles, but the number of terms when treated for poles with multiplicity via Eq. (3.27) increases to the order of 10^9. We note that in general the times t_c and t_e both scale linearly with the number of terms, $\zeta = \prod_p r_p$, where r_p is the number of poles with respect to each integration variable. This results in ζ increasing exponentially with expansion order but its details depend on the pole structure of a given diagram.

Concluding Remarks: Our approach has two main features. First, the result of AMI, once stored, is equivalent to an analytic result, and is therefore evaluated to machine precision. Furthermore, one can impose analytic continuation symbolically and move to real frequency space without any ill-defined numerical procedure. Second, once S, P and R_n are constructed the computational expense for generating the analytic function is small, and the total evaluation time reflects primarily the direct evaluation of the analytic function. Once constructed and stored, the function can be evaluated for any set of external variables ($\{\nu_\gamma\}$, $\{k_n\}$, $\{k_\gamma\}$, U, β, and μ) without accumulating error, unlike in DiagMC where one would observe a growth in variance for increasing frequency which worsens for increasing β. In this sense, with AMI the temporal parts of the Feynman integral are solved not only exactly (to machine precision), but also with the lowest possible computational expense, *i.e.* the evaluation of the analytic result. In addition, because the AMI result is an analytic expression in terms of the external variables, T-U-μ phase space can be explored, including the $T = 0$ limit, which is unreachable in the standard DiagMC methods.

In our three examples we have evaluated each diagram for a particular set of internal $\{k_n\}$ and external momenta $\{k_\gamma\}$. Generally, the evaluation of the remaining spatial integrals can be performed with continuous momentum-space resolution, as

in the case for DiagMC. Our results suggest that AMI is able to evaluate diagrams at an order relevant to other state-of-the-art methods while incurring a competitive computational cost. In addition, the symbolic result of AMI for each diagram, once constructed, can be applied to any diagram with the same topology given the initial set of ϵ^j dispersions. This leads to an interesting possibility that each configuration could be systematically evaluated and stored without need to reconstruct the S, P, and R_n arrays. Once stored, those arrays can be loaded into memory and systematically evaluated for an arbitrary Hubbard-like problem of arbitrary spatial dimension and dispersion.

What remains is to combine AMI with DiagMC (AMI+DiagMC). Such an extension will open new avenues to DiagMC, especially at $T = 0$, because AMI reduces the size of phase space by eliminating the need for probing the internal frequencies or the internal imaginary times in DiagMC. Consequently, this will reduce computational uncertainties and might improve convergence properties. However, there exist some technical hurdles which must be first overcome before AMI+DiagMC will be competitive. First, developing a general tool to provide the set of $\{\alpha\}$ values (set of momentum/energy conserving labels) for an arbitrary Feynman diagram topology is nontrivial. This can be overcome for restricted topologies such as those diagrams with only one external leg. Second, the standard DiagMC updates no longer apply, since the AMI result for a topology is an analytic function, and not an amplitude. With AMI one has a entirely new opportunity to use the analytic properties of the AMI result to further improve Monte Carlo importance sampling.

We have presented only the most straightforward algorithm but appreciate that optimizations likely exist. These might include improved routines for manipulating and storing the matrices of typically sparse α_p^j vectors, or approximation schemes whereby terms with small contributions are identified and never evaluated. While

in this work we applied the method to single-band systems with constant vertices, extension to non-constant vertices or multi-band systems should be explored. [22–25]

3.3 Acknowledgments

JPFL would like to thank Phillip E.C. Ashby for discussions leading to this work. This project was supported by the Simons collaboration on the many-electron problem and by the Natural Sciences and Engineering Research Council of Canada (NSERC). Computational resources were provided by Compute Canada via AceNet and Calcul-Quebec.

3.4 Supplemental material

3.4.1 Algebraic Operations

The objects required to construct the full analytic result for the multi-summation over Matsubara frequencies of bare Green's functions are the S, P and R_n arrays. Knowing these arrays we need only perform three algebraic operations '$*$', '$\times$', and '$\cdot$' to obtain the analytic result of the summation as described in the main text. In this section we aim to elucidate the definitions of these operations. We consider three arrays, H, C and D with length ℓ given by:

$$H = [h_1, h_2, ..., h_\ell] \tag{3.36}$$

$$C = \left[[c_1^1, c_1^2, ..., c_1^{m_1}], [c_2^1, c_2^2, ..., c_2^{m_2}], ..., [c_\ell^1, c_\ell^2, ..., c_\ell^{m_\ell}] \right] \tag{3.37}$$

and

$$D = \left[[d_1^1, d_1^2, ..., d_1^{m_1}], [d_2^1, d_2^2, ..., d_2^{m_2}], ..., [d_\ell^1, d_\ell^2, ..., d_\ell^{m_\ell}] \right] \tag{3.38}$$

The lengths of the ith element of C and D are equal to m_i.

First, we define the distribution function f operator on an array by its evaluation of every element of the array, for example:

$$\begin{aligned} f(C) =& f(\left[[c_1^1, c_1^2, ..., c_1^{m_1}], [c_2^1, c_2^2, ..., c_2^{m_2}], ..., [c_\ell^1, c_\ell^2, ..., c_\ell^{m_\ell}] \right]) \\ =& \left[[f(c_1^1), f(c_1^2), ..., f(c_1^{m_1})], [f(c_2^1), f(c_2^2), ..., f(c_2^{m_2})], ..., [f(c_\ell^1), f(c_\ell^2), ..., f(c_\ell^{m_\ell})] \right]. \end{aligned} \tag{3.39}$$

One may write down (3.39) in a compact form:

$$f(C)_i^j = f(C_i^j). \tag{3.40}$$

The operation '$*$' is defined by

$$\begin{aligned} C * D =& \left[[c_1^1, c_1^2, ..., c_1^{m_1}], [c_2^1, c_2^2, ..., c_2^{m_2}], ..., [c_\ell^1, c_\ell^2, ..., c_\ell^{m_\ell}] \right] * \\ & \left[[d_1^1, d_1^2, ..., d_1^{m_1}], [d_2^1, d_2^2, ..., d_2^{m_2}], ..., [d_\ell^1, d_\ell^2, ..., d_\ell^{m_\ell}] \right] \\ =& \left[[c_1^1 d_1^1, c_1^2 d_1^2, ..., c_1^{m_1} d_1^{m_1}], [c_2^1 d_2^1, c_2^2 d_2^2, ..., c_2^{m_2} d_2^{m_2}], ..., [c_\ell^1 d_\ell^1, c_\ell^2 d_\ell^2, ..., c_\ell^{m_\ell} d_\ell^{m_\ell}] \right], \end{aligned} \tag{3.41}$$

or

$$(C * D)_i^j = C_i^j D_i^j. \tag{3.42}$$

The operation '$\times$' is also introduced:

$$\begin{aligned} H \times C =& [h_1, h_2, ..., h_\ell] \times \left[[c_1^1, c_1^2, ..., c_1^{m_1}], [c_2^1, c_2^2, ..., c_2^{m_2}], ..., [c_\ell^1, c_\ell^2, ..., c_\ell^{m_\ell}] \right] \\ =& [h_1 c_1^1, h_1 c_1^2, ..., h_1 c_1^{m_1}, h_2 c_2^1, h_2 c_2^2, ..., h_2 c_2^{m_2}, ..., h_\ell c_\ell^1, h_\ell c_\ell^2, ..., h_\ell c_\ell^{m_\ell}], \end{aligned} \tag{3.43}$$

or

$$(H \times C)_i^j = H_i C_i^j. \tag{3.44}$$

Lastly, we define the '$\cdot$' operation:

$$\begin{aligned} H \cdot C =& [h_1, h_2, ..., h_\ell] \cdot \left[[c_1^1, c_1^2, ..., c_1^{m_1}], [c_2^1, c_2^2, ..., c_2^{m_2}], ..., [c_\ell^1, c_\ell^2, ..., c_\ell^{m_\ell}] \right] \\ =& h_1 [c_1^1, c_1^2, ..., c_1^{m_1}] + h_2 [c_2^1, c_2^2, ..., c_2^{m_2}] + ... + h_\ell [c_\ell^1, c_\ell^2, ..., c_\ell^{m_\ell}], \end{aligned} \tag{3.45}$$

or

$$H \cdot C = \sum_i H_i C_i. \tag{3.46}$$

3.4.2 Examples

In this section we present three examples with explicit results for the arrays S, P, and R_n and demonstrate how to construct the full analytic result using AMI. In all examples, the summations will be performed in the order ν_1, ν_2,..., ν_n.

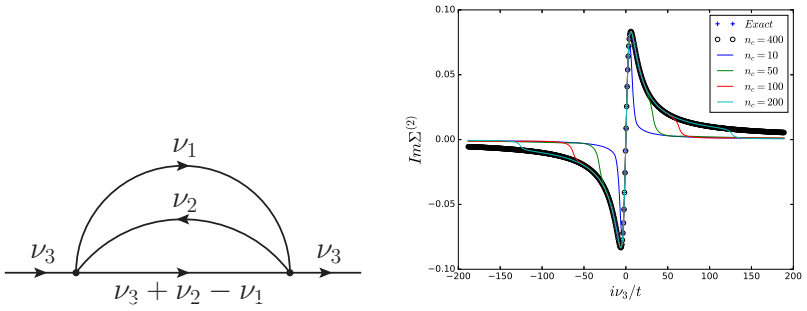

Figure 3.2: *Left*: Feynman diagram of $\Sigma^{(2)}$ corresponding to Eq. (3.30). ν_1, and ν_2 are independent fermionic frequencies, and ν_3 is a fermionic external frequency. *Right*: Imaginary part of $\Sigma^{(2)}$ as a function of ν_3 for crystal momentum point given in Eq. (3.48). The crosses show the result obtained from Eq. (3.51) while other lines are calculated using a finite summation with different cut-off numbers, n_c. As the cut-off increases the result of the finite summation converges to the exact curve calculated using AMI.

Self Energy $\Sigma^{(2)}$

We first evaluate a simple object, the second order Feynman diagram shown in Fig. 3.2. It is defined by the summation

$$\Sigma^{(2)} = \frac{1}{\beta^2} \sum_{\nu_1,\nu_2} G(i\nu_1)G(i\nu_2)G(i\nu_3 + i\nu_2 - i\nu_1) \tag{3.47}$$

where ν_1, ν_2, and ν_3 are fermionic Matsubara frequencies and $G(i\nu) = \frac{1}{i\nu - \epsilon_k}$ where ϵ_k is defined by the tight binding Hamiltonian on a two-dimensional square lattice. We (arbitrarily) select a point in the crystal momentum at:

$$\begin{aligned} \vec{k}_1 &= (0, 0) \\ \vec{k}_2 &= \vec{k}_3 = (\frac{\pi}{a}, \frac{\pi}{3a}). \end{aligned} \tag{3.48}$$

Eq. (3.47) can then be written as

$$\Sigma^{(2)} = \frac{1}{\beta^2} \sum_{\nu_1,\nu_2} \frac{1}{-4 + i\nu_1} \frac{1}{1 + i\nu_2} \frac{1}{-1 - i\nu_1 + i\nu_2 + i\nu_3} \tag{3.49}$$

where we have explicitly evaluated ϵ_{k_1}, ϵ_{k_2} and $\epsilon_{k_3+k_2-k_1}$ in units of the hopping amplitude, t. In the array representation of Green's functions this is written as

$$\Sigma^{(2)} \to \frac{1}{\beta^2} \sum_{\nu_1,\nu_2} \Big[[-4, 1, 0, 0]; [1, 0, 1, 0]; [-1, -1, 1, 1] \Big]. \tag{3.50}$$

Applying AMI we obtain the final analytic result:

$$\Sigma^{(2)} \to (S_1 * f(P_1)) \times (S_2 * f(P_2)) \cdot R_2^{\Sigma} \tag{3.51}$$

with

$$\begin{aligned} S_1 &= [1, -1] \\ S_2 &= \Big[[1, 1], [1, 1] \Big] \\ P_1 &= [4, -1 + i\nu_2 + i\nu_3] \\ P_2 &= \Big[[-1, 5 - i\nu_3], [5 - i\nu_3, -1] \Big] \\ R_2^{\Sigma} &= \Big[[-6, 0, 0, 1], [6, 0, 0, -1], [6, 0, 0, -1], [-6, 0, 0, 1] \Big] \end{aligned} \tag{3.52}$$

The construction of Eq. (3.51) is equivalent to the full analytic result in the usual representation:

$$\begin{aligned}\Sigma^{(2)} =& \frac{f(4)f(-1)}{-6+i\nu_3} + \frac{f(4)f(5-i\nu_3)}{6-i\nu_3} + \\ & \frac{-f(-1+i\nu_2+i\nu_3)f(5-i\nu_3)}{6-i\nu_3} + \\ & \frac{-f(-1+i\nu_2+i\nu_3)f(-1)}{-6+i\nu_3}.\end{aligned} \tag{3.53}$$

In Fig. 3.2 we plot $\Sigma^{(2)}$ versus external frequency, ν_3 at $\beta = 10$ and $\mu = 0$ using AMI and by direct summation of Eq. (3.30) over internal Matsubara frequencies. As expected, by increasing the cut-off number n_c, the finite summation approximation results converge to the exact result computed by AMI.

Multi-Leg Diagram, Λ^{env}

The second object we investigate is Λ^{env} shown in Fig. 3.3:

$$\Lambda^{env} = \frac{1}{\beta^3} \sum_{\nu_1,\nu_2,\nu_3} G(i\nu_1)G(i\nu_2)G(i\nu_3)G(i\omega)G(i\eta)G(i\theta) \tag{3.54}$$

with independent frequencies $i\nu_1 ... i\nu_6$ and fully dependent frequency labels

$$\begin{aligned}\omega &= \nu_1 + \nu_2 + \nu_3 - \nu_4 - \nu_5 - \nu_6 \\ \eta &= \nu_2 + \nu_3 - \nu_4 - \nu_6 \\ \theta &= \nu_1 + \nu_2 - \nu_4\end{aligned} \tag{3.55}$$

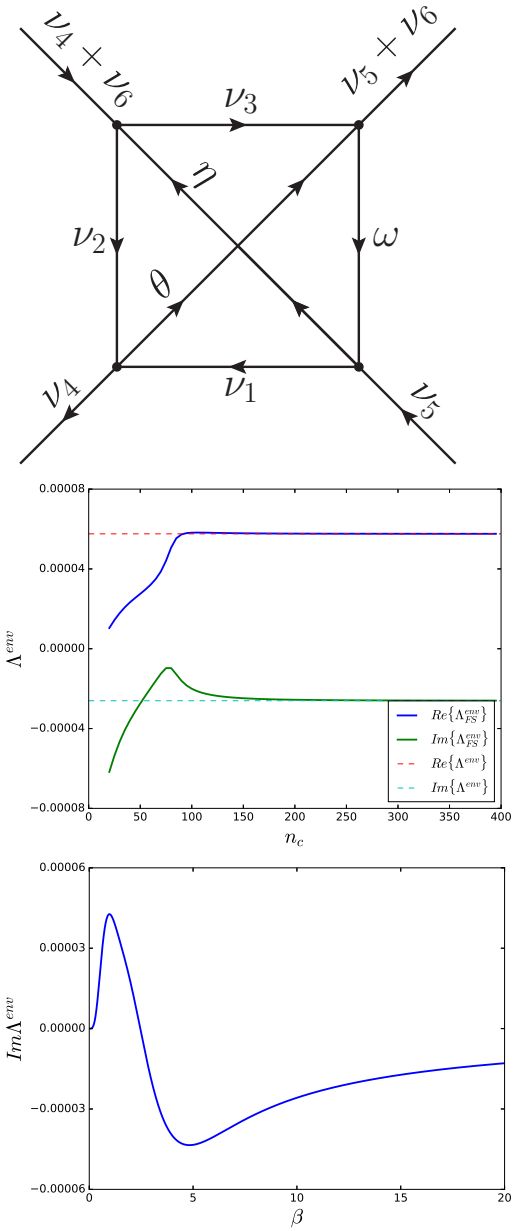

Figure 3.3: *Top*: Feynman diagram of Λ^{env} given by Eq. (3.31). *Middle*: Imaginary and real parts of Λ^{env} calculated using AMI (dashed lines) and by finite summation for various cut-offs evaluated at the momenta in Eq. (3.56). We fix $\beta = 10$, $\mu = 0$ and the external frequencies have been set to $\nu_4 = \frac{\pi}{\beta}$, $\nu_5 = 161\frac{\pi}{\beta}$, and $\nu_6 = 0$. *Bottom*: Temperature dependence of the imaginary part of Λ^{env} calculated using AMI, which approaches zero as $\beta \to \infty$.

where all the ν_i Matsubara frequencies are fermionic except for ν_6 which is bosonic. We (arbitrarily) select a point in the crystal momentum at

$$\begin{aligned} \vec{k}_1 &= (0,0) \\ \vec{k}_2 = \vec{k}_3 = \vec{k}_4 = \vec{k}_5 = \vec{k}_6 &= (\frac{\pi}{a}, \frac{\pi}{3a}) \end{aligned} \tag{3.56}$$

Applying AMI we immediately achieve the full analytic result,

$$\Lambda^{env} \to (S_1 * f(P_1)) \times (S_2 * f(P_2)) \times (S_3 * f(P_3)) \cdot R_3^{\Lambda} \tag{3.57}$$

where the arrays of signs are given by

$$\begin{aligned} S_1 &= [1,1,1] \\ S_2 &= \Big[[1,1,1,1],[-1,1,1],[-1,1,1]\Big] \\ S_3 &= \Big[[1,1,1],[-1,1,-1],[-1,1,-1],[1,1,1],[-1,1,-1], \\ &[-1,1,1,-1],[-1,1,-1],[1,1,1],[1,1,1],[1,-1,1,1]\Big] \end{aligned} \tag{3.58}$$

and the arrays of poles are

$$P_1 = [4, -1 - i\nu_2 - i\nu_3 + i\nu_4 + i\nu_5 + i\nu_6, 4 - i\nu_2 + i\nu_4] \tag{3.59}$$

$$P_2 = \Big[[-1, -5 - i\nu_3 + i\nu_4 + i\nu_5 + i\nu_6, 4 - i\nu_3 + i\nu_4 + i\nu_6, i\nu_4],$$

$$[-5 - i\nu_3 + i\nu_4 + i\nu_5 + i\nu_6, -1, 4 - i\nu_3 + i\nu_4 + i\nu_6], [i\nu_4, -1, 4 - i\nu_3 + i\nu_4 + i\nu_6]\Big]$$

$$P_3 = \Big[[-1, -4 + i\nu_4 + i\nu_5 + i\nu_6, 5 + i\nu_4 + i\nu_6], [-4 + i\nu_4 + i\nu_5 + i\nu_6, -1, -5 + i\nu_5 + i\nu_6],$$

$$[5 + i\nu_4 + i\nu_6, -1, 4 + i\nu_6], [-1, -5 + i\nu_5 + i\nu_6, 4 + i\nu_6],$$

$$[-4 + i\nu_4 + i\nu_5 + i\nu_6, -1, -5 + i\nu_5 + i\nu_6], [-4 + i\nu_4 + i\nu_5 + i\nu_6, -1, 5 + i\nu_4 + i\nu_6, -5 + i\nu_5 + i\nu_6],$$

$$[5 + i\nu_4 + i\nu_6, -1, -5 + i\nu_5 + i\nu_6], [-1, -5 + i\nu_5 + i\nu_6, 4 + i\nu_6], [-1, -5 + i\nu_5 + i\nu_6, 5 + i\nu_4 + i\nu_6],$$

$$[4 + i\nu_6, 5 + i\nu_4 + i\nu_6, -1, -5 + i\nu_5 + i\nu_6]\Big]$$

We also present the entries of the array R_3^Λ in analytic form:

$$\begin{aligned}
R_3^1 &= \frac{1}{3 - i\nu_4 - i\nu_5 - i\nu_6}\frac{1}{-6 - i\nu_4 - i\nu_6}\frac{1}{-1 - i\nu_4} \\
R_3^2 &= \frac{1}{-3 + i\nu_4 + i\nu_5 + i\nu_6}\frac{1}{-9 + i\nu_5}\frac{1}{-1 - i\nu_4} \\
R_3^3 &= \frac{1}{6 + i\nu_4 + i\nu_6}\frac{1}{9 - i\nu_5}\frac{1}{-1 - i\nu_4} \\
R_3^4 &= \frac{1}{-3 + i\nu_4 + i\nu_5 + i\nu_6}\frac{1}{-9 + i\nu_5}\frac{1}{-1 - i\nu_4} \\
R_3^5 &= \frac{1}{-3 + i\nu_4 + i\nu_5 + i\nu_6}\frac{1}{-9 + i\nu_5}\frac{1}{-4 + i\nu_5 + i\nu_6} \\
R_3^6 &= \frac{1}{1 + i\nu_4}\frac{1}{-4 + i\nu_5 + i\nu_6}\frac{1}{-9 + i\nu_5} \\
R_3^7 &= \frac{1}{6 + i\nu_4 + i\nu_6}\frac{1}{9 - i\nu_5}\frac{1}{-1 - i\nu_4} \\
R_3^8 &= \frac{1}{6 + i\nu_4 + i\nu_6}\frac{1}{9 - i\nu_5}\frac{1}{5 + i\nu_6}
\end{aligned} \tag{3.60}$$

$$R_3^9 = \frac{1}{1+i\nu_4}\frac{1}{5+i\nu_6}\frac{1}{9-i\nu_5}$$
$$R_3^{10} = \frac{1}{1+i\nu_4}\frac{1}{4-i\nu_5-i\nu_6}\frac{1}{-5-i\nu_6}$$
$$R_3^{11} = \frac{1}{1+i\nu_4}\frac{1}{-4+i\nu_5+i\nu_6}\frac{1}{-9+i\nu_5}$$
$$R_3^{12} = \frac{1}{1+i\nu_4}\frac{1}{5+i\nu_6}\frac{1}{9-i\nu_5}$$
$$R_3^{13} = \frac{1}{-3+i\nu_4+i\nu_5+i\nu_6}\frac{1}{-9+i\nu_5}\frac{1}{-1-i\nu_4}$$
$$R_3^{14} = \frac{1}{-3+i\nu_4+i\nu_5+i\nu_6}\frac{1}{-9+i\nu_5}\frac{1}{-4+i\nu_5+i\nu_6}$$
$$R_3^{15} = \frac{1}{1+i\nu_4}\frac{1}{-4+i\nu_5+i\nu_6}\frac{1}{-9+i\nu_5}$$
$$R_3^{16} = \frac{1}{-3+i\nu_4+i\nu_5+i\nu_6}\frac{1}{-9+i\nu_5}\frac{1}{-1-i\nu_4}$$
$$R_3^{17} = \frac{1}{-3+i\nu_4+i\nu_5+i\nu_6}\frac{1}{-6-i\nu_4-i\nu_6}\frac{1}{-4+i\nu_5+i\nu_6}$$
$$R_3^{18} = \frac{1}{-9+i\nu_5}\frac{1}{6+i\nu_4+i\nu_6}\frac{1}{-10-i\nu_4+i\nu_5}$$
$$R_3^{19} = \frac{1}{1+i\nu_4}\frac{1}{-4+i\nu_5+i\nu_6}\frac{1}{-10-i\nu_4+i\nu_5}$$
$$R_3^{20} = \frac{1}{-9+i\nu_5}\frac{1}{6+i\nu_4+i\nu_6}\frac{1}{-10-i\nu_4+i\nu_5}$$
$$R_3^{21} = \frac{1}{-9+i\nu_5}\frac{1}{6+i\nu_4+i\nu_6}\frac{1}{-4+i\nu_5+i\nu_6}$$
$$R_3^{22} = \frac{1}{-9+i\nu_5}\frac{1}{10+i\nu_4-i\nu_5}\frac{1}{-4+i\nu_5+i\nu_6}$$
$$R_3^{23} = \frac{1}{1+i\nu_4}\frac{1}{4-i\nu_5-i\nu_6}\frac{1}{-5-i\nu_6}$$
$$R_3^{24} = \frac{1}{1+i\nu_4}\frac{1}{-4+i\nu_5+i\nu_6}\frac{1}{-9+i\nu_5}$$
$$R_3^{25} = \frac{1}{1+i\nu_4}\frac{1}{5+i\nu_6}\frac{1}{9-i\nu_5}$$
$$R_3^{26} = \frac{1}{1+i\nu_4}\frac{1}{4-i\nu_5-i\nu_6}\frac{1}{-6-i\nu_4-i\nu_6}$$
$$R_3^{27} = \frac{1}{1+i\nu_4}\frac{1}{-4+i\nu_5+i\nu_6}\frac{1}{-10-i\nu_4+i\nu_5}$$
$$R_3^{28} = \frac{1}{1+i\nu_4}\frac{1}{6+i\nu_4+i\nu_6}\frac{1}{10+i\nu_4-i\nu_5}$$

$$
\begin{aligned}
R_3^{29} &= \frac{1}{1+i\nu_4}\frac{1}{5+i\nu_6}\frac{1}{9-i\nu_5} \\
R_3^{30} &= \frac{1}{1+i\nu_4}\frac{1}{6+i\nu_4+i\nu_6}\frac{1}{10+i\nu_4-i\nu_5} \\
R_3^{31} &= \frac{1}{-5-i\nu_6}\frac{1}{6+i\nu_4+i\nu_6}\frac{1}{4-i\nu_5-i\nu_6} \\
R_3^{32} &= \frac{1}{-9+i\nu_5}\frac{1}{10+i\nu_4-i\nu_5}\frac{1}{-4+i\nu_5+i\nu_6}
\end{aligned}
\tag{3.61}
$$

Fig. 3.3 compares the convergence of the finite summation procedure to the exact result calculated by AMI for the real and imaginary parts of Λ^{env}. The temperature dependence of imaginary part of Λ^{env} is shown in the bottom figure.

We notice that the first element of the last entry of P_2 is purely fermionic with zero energy, and the evaluation of Fermi (bose) distribution function at this pole is formally divergent. To get around this issue one has to add a small regulator to such a pole, in this case $i\nu_4 \to i\nu_4 + \Gamma$ where $\Gamma \to 0$. In Fig. 3.4 we present the dependence of Λ^{env} to the regulator Γ. As shown the result is largely independent of Γ (except when Γ becomes very large) and the result converges to the value obtained by direct summation.

9th Order Diagram, J

As a final example we consider the high order diagram J shown in Fig. 3.5. [26] This diagram is chosen to be intentionally complicated, as a test of the AMI method, and has nine vertices (nine integration variables) with 17 Green's functions. The

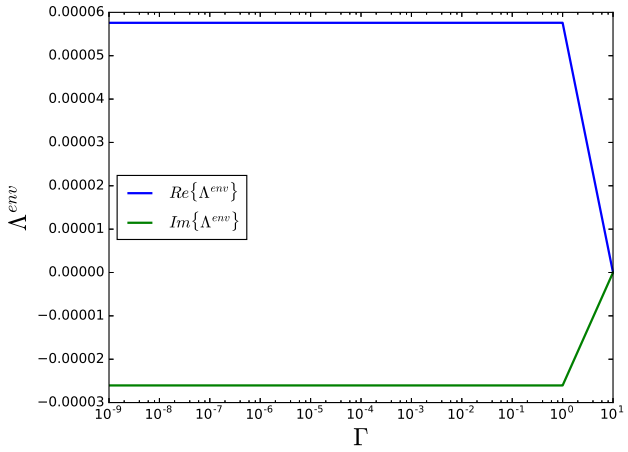

Figure 3.4: Imaginary and real parts of Λ^{env} vs. the regulator Γ computed using AMI. We fix $\beta = 10$, $\mu = 0$, the momenta are defined by Eq. (3.56) and the external frequencies have been set to $\nu_4 = \frac{\pi}{\beta}$, $\nu_5 = 161\frac{\pi}{\beta}$, and $\nu_6 = 0$. For small enough values of Γ both real and imaginary parts of the object do not depend on the choice of the regulator.

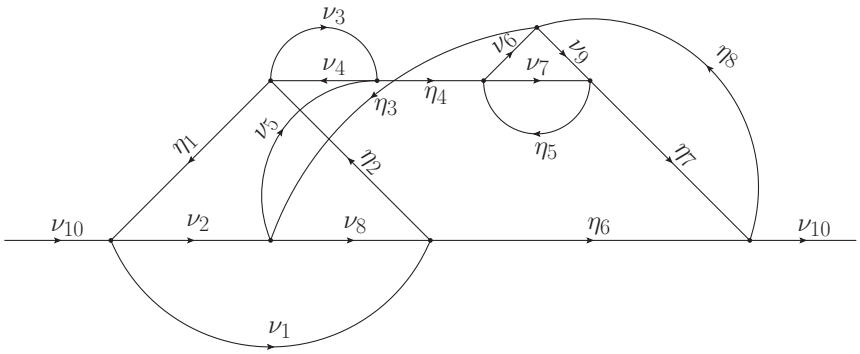

Figure 3.5: Feynman Diagram of J defined by Eq. (3.62) as a ninth order diagram.

summation is

$$J = \frac{1}{\beta^9} \sum_{\{\nu_i\}_{i=1}^9} \Big\{ G(i\nu_1)G(i\nu_2)G(i\nu_3)G(i\nu_4)G(i\nu_5)G(i\nu_6) \\ G(i\nu_7)G(i\nu_8)G(i\nu_9)G(i\eta_1)G(i\eta_2)G(i\eta_3) \\ G(i\eta_4)G(i\eta_5)G(i\eta_6)G(i\eta_7)G(i\eta_8) \Big\} \tag{3.62}$$

Table 3.1: Number of terms at each stage of the summation for diagram J. Column N_{sp} is the result when it is assumed (incorrectly) that all poles are simple poles. Column N_{mp} is the correct result, which takes into account the higher multiplicity of poles.

summation stage	N_{sp}	N_{mp}
ν_1	3	3
ν_2	16	16
ν_3	110	110
ν_4	298	538
ν_5	1538	11886
ν_6	6978	205427
ν_7	20224	1944668
ν_8	92780	56109709
ν_9	337982	$\sim 10^9$

with

$$\begin{aligned}
\eta_1 &= \nu_1 + \nu_2 - \nu_{10} \\
\eta_2 &= \nu_1 + \nu_2 + \nu_3 - \nu_4 - \nu_{10} \\
\eta_3 &= \nu_5 + \nu_8 - \nu_2 \\
\eta_4 &= \nu_5 + \nu_3 - \nu_4 \\
\eta_5 &= \nu_6 + \nu_7 - \nu_5 - \nu_3 + \nu_4 \\
\eta_6 &= \nu_8 - \nu_2 + \nu_{10} - \nu_3 + \nu_4 \\
\eta_7 &= \nu_9 - \nu_6 + \nu_5 + \nu_3 - \nu_4 \\
\eta_8 &= \nu_5 + \nu_8 - \nu_2 + \nu_9 - \nu_6
\end{aligned} \tag{3.63}$$

which we evaluate at the crystal momenta given by

$$\vec{k}_1 = (0,0) \tag{3.64}$$
$$\vec{k}_2 = \vec{k}_3 = \vec{k}_4 = \vec{k}_5 = \vec{k}_6 = \vec{k}_7 = \vec{k}_8 = \vec{k}_9 = (\frac{\pi}{a}, \frac{\pi}{3a}).$$

We find from the third stage onwards that non-simple poles with multiplicity $M > 1$ emerge. We then construct an appropriate representation for the full analytic expression by considering the general residues for poles with multiplicity as described in the main text. As shown in Table 3.1, when poles with $M > 1$ emerge the number of terms increases dramatically from the fourth summation stage onward, and by the end of the procedure the total number of terms is on the order of 10^9. Table 3.1 implies that although our approach can be applied to any diagram of arbitrary complexity, in practice the presence of poles with high multiplicities (especially in the first stages of the summation) causes the computational cost to grow significantly. In these cases, identifying where in $\{k_n\}$ space multiplicities arise will be essential to determining if evaluating a given diagram is tractable using this method.

Bibliography

[1] Kris Van Houcke, Evgeny Kozik, N. Prokof'ev, and B. Svistunov. Diagrammatic Monte Carlo. *Phys. Proc.*, 6:95 – 105, 2010.

[2] K. Van Houcke, F. Werner, E. Kozik, N. Prokof'ev, B. Svistunov, M. J. H. Ku, A. T. Sommer, L. W. Cheuk, A. Schirotzek, and M. W. Zwierlein. *Nature Phys.*, 8:366, 2012.

[3] E. Kozik, K. Van Houcke, E. Gull, L. Pollet, N. Prokof'ev, B. Svistunov, and M. Troyer. Diagrammatic Monte Carlo for correlated fermions. *Europhys. Lett.*,

90(1):10004, 2010.

[4] Riccardo Rossi. Determinant Diagrammatic Monte Carlo Algorithm in the Thermodynamic Limit. *Phys. Rev. Lett.*, 119:045701, 2017.

[5] Amir Taheridehkordi, S. H. Curnoe, and J. P. F. LeBlanc. Algorithmic Matsubara integration for Hubbard-like models. *Phys. Rev. B*, 99:035120, 2019.

[6] J. P. F. LeBlanc, Andrey E. Antipov, Federico Becca, Ireneusz W. Bulik, Garnet Kin-Lic Chan, Chia-Min Chung, Youjin Deng, Michel Ferrero, Thomas M. Henderson, Carlos A. Jiménez-Hoyos, E. Kozik, Xuan-Wen Liu, Andrew J. Millis, N. V. Prokof'ev, Mingpu Qin, Gustavo E. Scuseria, Hao Shi, B. V. Svistunov, Luca F. Tocchio, I. S. Tupitsyn, Steven R. White, Shiwei Zhang, Bo-Xiao Zheng, Zhenyue Zhu, and Emanuel Gull. Solutions of the Two-Dimensional Hubbard Model: Benchmarks and Results from a Wide Range of Numerical Algorithms. *Phys. Rev. X*, 5:041041, 2015.

[7] A. Toschi, A. A. Katanin, and K. Held. Dynamical vertex approximation: A step beyond dynamical mean-field theory. *Phys. Rev. B*, 75:045118, 2007.

[8] A. N. Rubtsov, M. I. Katsnelson, and A. I. Lichtenstein. Dual fermion approach to nonlocal correlations in the Hubbard model. *Phys. Rev. B*, 77:033101, 2008.

[9] A. N. Rubtsov, M. I. Katsnelson, A. I. Lichtenstein, and A. Georges. Dual fermion approach to the two-dimensional Hubbard model: Antiferromagnetic fluctuations and Fermi arcs. *Phys. Rev. B*, 79:045133, 2009.

[10] Nikolay Prokof'ev and Boris Svistunov. Bold Diagrammatic Monte Carlo Technique: When the Sign Problem Is Welcome. *Phys. Rev. Lett.*, 99:250201, 2007.

[11] S. A. Kulagin, N. Prokof'ev, O. A. Starykh, B. Svistunov, and C. N. Varney. Bold Diagrammatic Monte Carlo Method Applied to Fermionized Frustrated Spins. *Phys. Rev. Lett.*, 110:070601, 2013.

[12] Evgeny Kozik, Michel Ferrero, and Antoine Georges. Nonexistence of the Luttinger-Ward Functional and Misleading Convergence of Skeleton Diagrammatic Series for Hubbard-Like Models. *Phys. Rev. Lett.*, 114:156402, 2015.

[13] Walter Tarantino, Pina Romaniello, J. A. Berger, and Lucia Reining. Self-consistent Dyson equation and self-energy functionals: An analysis and illustration on the example of the Hubbard atom. *Phys. Rev. B*, 96:045124, 2017.

[14] Fedor Šimkovic and Evgeny Kozik. Determinant Monte Carlo for irreducible Feynman diagrams. *arXiv:1712.10001*, 2017.

[15] Alice Moutenet, Wei Wu, and Michel Ferrero. Determinant Monte Carlo algorithms for dynamical quantities in fermionic systems. *Phys. Rev. B*, 97:085117, 2018.

[16] Dominic Bergeron and A.-M. S. Tremblay. Algorithms for optimized maximum entropy and diagnostic tools for analytic continuation. *Phys. Rev. E*, 94:023303, 2016.

[17] R. Levy, J. P. F. LeBlanc, and E. Gull. Implementation of the Maximum Entropy Method for Analytic Continuation. *Comp. Phys. Comm.*, 215:149, 2017.

[18] B Bauer, L D Carr, H G Evertz, A Feiguin, J Freire, S Fuchs, L Gamper, J Gukelberger, E Gull, S Guertler, A Hehn, R Igarashi, S V Isakov, D Koop, P N Ma, P Mates, H Matsuo, O Parcollet, G Pawłowski, J D Picon, L Pollet, E Santos, V W Scarola, U Schollwöck, C Silva, B Surer, S Todo, S Trebst,

M Troyer, M L Wall, P Werner, and S Wessel. The ALPS project release 2.0: open source software for strongly correlated systems. *J. Stat. Mech.: Theo. and Exp.*, 2011(05):P05001, 2011.

[19] A. Gaenko, A.E. Antipov, G. Carcassi, T. Chen, X. Chen, Q. Dong, L. Gamper, J. Gukelberger, R. Igarashi, S. Iskakov, M. Könz, J.P.F. LeBlanc, R. Levy, P.N. Ma, J.E. Paki, H. Shinaoka, S. Todo, M. Troyer, and E. Gull. Updated core libraries of the ALPS project. *Comp. Phys. Comm.*, 213:235 – 251, 2017.

[20] G. Rohringer, A. Valli, and A. Toschi. Local electronic correlation at the two-particle level. *Phys. Rev. B*, 86(12):125114, 2012.

[21] See Supplemental Material, for details of the examples given in the text.

[22] Sergei Iskakov, Hanna Terletska, and Emanuel Gull. Momentum-space cluster dual-fermion method. *Phys. Rev. B*, 97:125114, 2018.

[23] Sergei Iskakov, Andrey E. Antipov, and Emanuel Gull. Diagrammatic Monte Carlo for dual fermions. *Phys. Rev. B*, 94:035102, 2016.

[24] Jan Gukelberger, Evgeny Kozik, and Hartmut Hafermann. Diagrammatic Monte Carlo approach for diagrammatic extensions of dynamical mean-field theory: Convergence analysis of the dual fermion technique. *Phys. Rev. B*, 96:035152, 2017.

[25] Guy Cohen, Emanuel Gull, David R. Reichman, and Andrew J. Millis. Taming the Dynamical Sign Problem in Real-Time Evolution of Quantum Many-Body Problems. *Phys. Rev. Lett.*, 115:266802, 2015.

[26] Riccardo Rossi, Takahiro Ohgoe, Kris Van Houcke, and Félix Werner. *arXiv preprint arXiv:1802.07717*, 2017.

Chapter 4

Optimal grouping of arbitrary diagrammatic expansions via analytic pole structure

In Chapter 3 we presented a systematic way to evaluate the Matsubara sums of a given Feynman diagram. However, as mentioned before, to complete the evaluation of each diagram in the perturbative expansion the momenta sums should be evaluated as well.

In this chapter we complete our machinery by first providing a general algorithm to construct the diagram topologies in the expansion. We then present an automatic procedure which translates each diagram to its corresponding mathematical expression. Finally, we propose a combination of AMI and Monte Carlo integration routines to evaluate arbitrary Feynman diagrammatic expansions.

One of the most challenging tasks in Monte Carlo integration is to handle the 'sign problem', which is the near cancellation of contributions with opposite signs and the large error which appears as a consequence [2, 3]. In order to suppress the

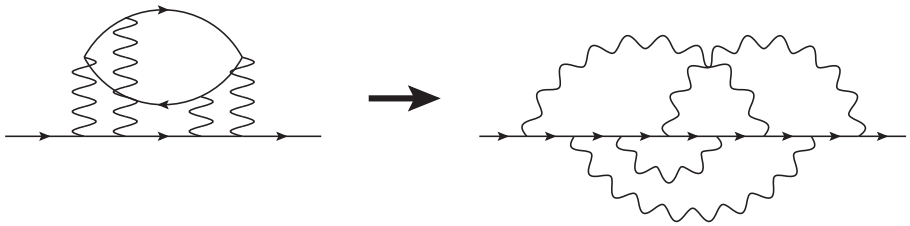

Figure 4.1: *Left*: a Hubbard self-energy diagram. *Right*: the result of applying a crossing symmetry operation to this diagram following the procedure described in Ref. [1]. This transformation results in the non-Hubbard diagram shown in the right panel.

issue it has been recently proposed to sort the diagrams into so-called sign-blessed groups by taking advantage of *crossing symmetry* [1]. Since each sign-blessed group is assumed to contain (nearly) canceling diagrams, one could suppress the sign problem and enhance the efficiency of Monte Carlo routines by group-by-group sampling of diagrams. However, it turns out that such an approach is extremely inefficient for the Hubbard model since the application of crossing symmetry operations typically transforms a Hubbard-type diagram to a non-Hubbard-type graph *. An example of such an operation is shown in Fig. 4.1.

Our main goal in this chapter is to invent and develop a systematic procedure to construct sign-blessed groups for the Hubbard model. Instead of using crossing symmetry, we present a general grouping procedure based upon the *analytic pole structure* of the diagrams. We introduce graph invariant transformations (GITs) to precisely determine (nearly) canceling and (nearly) equal diagrams. This enables us to construct optimally sign-blessed groups, and as the result, reduce the sign problem.

Although our method is applicable to any diagrammatic expansion composed of bare Green's functions, we take the self-energy function as an example and benchmark our results on both the Matsubara and real frequency axes.

In the rest of this chapter we reproduce Ref. [4], Amir Taheridehkordi, Stephanie

*See Chapter 2 for definition of Hubbard-type diagrams.

H. Curnoe, and James P. F. LeBlanc, doi: 10.1103/PhysRevB.101.125109; License number: RNP/20/OCT/031577; reproduced with kind permission of the publishers of Physical Review B. The manuscript is followed by Supplemental Material.

4.1 Abstract

We present a general method to optimize the evaluation of Feynman diagrammatic expansions which uses an automated symbolic assignment of momentum/energy conserving variables to each diagram. With this symbolic representation, we utilize the pole structure of each diagram to sort the Feynman diagrams into groups that are likely to contain nearly equal or nearly canceling diagrams, and we show that for some model parameters this cancellation is *exact*. This allows for a potentially massive cancellation during the numerical integration of internal momenta variables, leading to an optimal suppression of the 'sign problem' and hence reducing the computational cost. Although we define these groups using a frequency space representation, the equality or cancellation of diagrams within the group remains valid in other representations such as imaginary time used in standard diagrammatic Monte Carlo. As an application of the approach we apply this method, combined with algorithmic Matsubara integration (AMI) [A. Taheridehkordi, S. H. Curnoe, and J. P. F. LeBlanc, Phys. Rev. **B** 99, 035120 (2019)] and Monte Carlo methods, to the Hubbard model self-energy expansion on a 2D square lattice, which we evaluate and compare with existing benchmarks.

4.2 Introduction

One of the most challenging problems in condensed matter physics is correctly evaluating electronic interactions for free particle or lattice systems with many electrons.

This problem is of course a subset of a more general problem, that of fermionic particles interacting through bosonic exchange. In one sense, this problem is addressed by many-body perturbation theory using the formalism of Feynman diagrammatics, which allows one to construct in an intuitive manner the contributions at each order in perturbation theory. [5–7] In practice, however, it is extraordinarily difficult to handle more than just the lowest order diagrams due to the factorial increase in the number of diagrams at each order, [8] and this is further exacerbated by the high dimensional integrals that must be performed in order to evaluate each Feynman diagram.

Diagrammatic Monte Carlo (DiagMC) is a powerful method for numerically evaluating such diagrammatic expansions. [9–13] However, there is in general a Monte Carlo sign problem [2, 3] with multiple origins. The first, warmly referred to as the 'sign blessing', is the huge cancellation that must exist between different Feynman diagrams at each order in order for the series to converge. [14] The second sign problem occurs during the integration of each individual diagram, since the integrand in frequency space does not have a definite sign. One can devise methods to mitigate the second problem, but the first, the cancellation between topologically distinct diagrams, is disastrous to standard DiagMC. Recently, a number of proposals to address this have surfaced, such as grouping diagrams that may partially cancel, [1] or reconstructing the expansion in the form of a determinant. [13, 15, 16] These methods rely on the Matsubara formalism in that final results are evaluated for Matsubara (imaginary) frequencies ($i\nu_n$) or imaginary times (τ) and not on the real frequency axis. This has excellent utility for thermodynamic properties, where the temporal degree of freedom is integrated, but is problematic for direct frequency dependent observables such as the density of states, since the analytic continuation $i\nu_n \to \nu + i0^+$ cannot be uniquely performed for numerical data and requires an ill-posed inversion via methods such as maximum entropy inversion. [17, 18] Performing such procedures

ultimately dominates the uncertainty in the result and undermines any attempt at precision numerics. [19] Worse still is the compression of Matsubara frequencies in the low temperature limit where numerical Monte Carlo methods become effectively non-ergodic, leading to poor convergence.

The entirety of this problem can be sidestepped by simply following standard many-body perturbation theory and evaluating the internal Matsubara sums analytically. The only roadblock to doing so is the complexity of the analytic expressions. This roadblock has recently been overcome by the method of algorithmic Matsubara integration (AMI) [20] that in principle allows for the symbolic evaluation of the Matsubara sums for arbitrarily complex Feynman diagrams with minimal computational expense. The analytic result of AMI can be evaluated at *any* temperature and the analytic continuation is trivialized since it can be imposed symbolically: $i\nu_n \to \nu + i0^+$. What remains is to sample a factorially growing space of diagram topologies and perform the spatial integrals, a problem typically reserved for DiagMC. However, since AMI is formulated on the frequency axis, standard DiagMC will suffer a severe sign problem, and cannot be directly implemented.

In this manuscript we take a new approach to the sign problem. By considering Feynman diagrams in the Matsubara frequency representation we define a general procedure based on the analytic structure of each integrand that allows us to identify sets of topologically distinct Feynman graphs that *exactly cancel* or are *exactly equal* and further to identify other diagrams that can be trivially evaluated to be zero. In systems where the cancellation is not exact our method can identify and pair *nearly* canceling diagrams, i.e., we systematically construct optimally sign-blessed groups. By pairing such diagrams during the numeric evaluation of momenta integrals we guarantee a huge cancellation, which suppresses the sign problem. Our procedure is general in that it can be applied to any Feynman diagrammatic expansion with any

interaction. As proof of principle we evaluate the numerical results for a particular perturbative expansion, the Hubbard model [21, 22] on a two-dimensional square lattice. We construct the self-energy perturbative expansion up to sixth order at and away from half-filling. We then systematically group diagrams to provide what we believe to be the optimal set of diagrams to be evaluated using AMI and Monte Carlo methods and compare low order results to other numerical methods and benchmarks.

4.3 Methods

In this section we outline each step required to group and evaluate diagrammatic expansions. What we propose is in fact conceptually simple but notationally complicated and for this reason we take a pedantic approach and describe in detail how to: generate and store diagrams symbolically; automate the evaluation of Matsubara sums analytically via AMI; systematically classify diagrams; and construct the optimal groups of diagrams for a particular problem.

Central to this method is the pre-generation of diagrams and assignment of symbolic momentum conserving variables, the first step in the standard procedure for translating Feynman graphs to integrals. This is not typically done in DiagMC, which instead probes energy/momentum configurations via the propagation of worms. [23] We will see that while the assignment of momentum conserving variables is not unique, each diagram has a pole structure that is fundamental and cannot be hidden by any particular choice of momentum conserving variables. We therefore base our diagram classification on these fundamental and physical poles. We apply the procedure to the self-energy expansion, but the same procedures can be applied to other multileg or bosonic particle expansions.

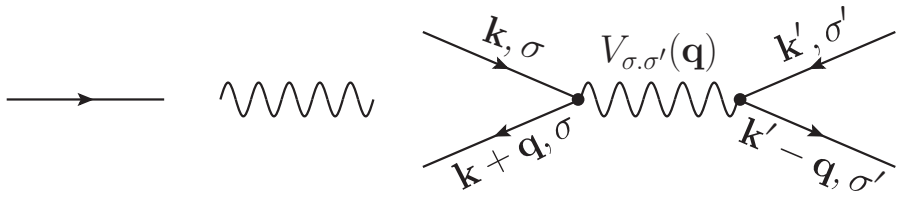

Figure 4.2: Diagrammatic representation of *Left*: Fermionic line, *Middle*: Interaction line, and *Right*: Two-body interaction $V_{\sigma,\sigma'}(\mathbf{q})$ between two fermionic lines with spins σ and σ'. Each line should be assigned with momentum/energy conserving variables.

4.3.1 Constructing Diagrams and Integrands

The building blocks of a Feynman diagram are fermionic (solid) and bosonic (wavy) lines (see Figure 4.2). If there is a boson mediated two-body interaction $V_{\sigma,\sigma'}(\mathbf{q})$ in the system one can represent the interaction between two fermionic lines as shown in Figure 4.2, which additionally contains two factors of the bare vertex. Assuming one knows the free particle dispersion of each propagator and how they couple (the bare vertex) then we have all the information required to convert the diagram into an integral. If one can first draw all possible topologically distinct diagrams up to a given interaction order (or number of loops) then the problem is essentially reduced to the evaluation of a set of integrals with known integrands. While stating this is simple, as already mentioned this is extremely challenging primarily due to the high dimensionality of the integrals.

In order to systematically produce all terms in an expansion one requires a set of processes to change the order and topology of the diagrams. The two simplest processes increase the order of a diagram by one: add an interaction line (AIL); and add a tadpole (AT) (see Figure 4.3). Without loss of generality, in what follows we will consider $V_{\sigma,\sigma'}(\mathbf{q})$ to be a Coulomb interaction but note that a general bosonic propagator $\mathcal{D}_0(i\Omega_m, \mathbf{q})$ can be similarly treated. Further, we restrict our discussion to the diagram space with 2-external legs, with the intent of constructing the set of

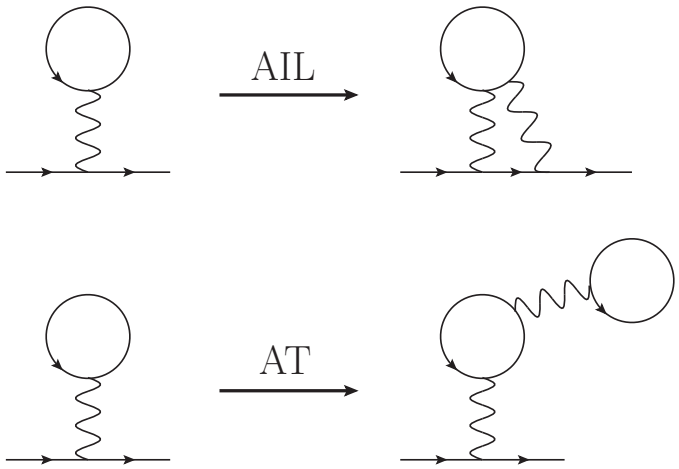

Figure 4.3: Diagrammatic illustration of *Top*: AIL and *Bottom*: AT procedures in generation of the diagrammatic expansion described in the text. In AIL one interaction (wavy) line is added to the diagram while in AT a tadpole (simple fermionic loop with a wavy tail) is added to the diagram.

self-energy diagrams (the set of one-particle irreducible diagrams) but the procedure remains unchanged for other diagrammatic series. To generate the series we start with diagrams of order m and by systematically applying AIL and AT we generate all the possible diagrams of order $m+1$. Double counting of topologically equivalent graphs is not allowed and one therefore needs to discard duplicate graphs through explicit graph-isomorphism comparison. For this, the formal graph representation of diagrams is essential and the isomorphism checks can be aided by a tree decomposition of the graph [24]. We then store all of the topologically distinct, non-isomorphic diagrams. We then iterate the procedure at each order to generate all diagrams in the expansion up to an arbitrary order.

For each diagram D_{ζ_m} of order m with topology ζ_m we follow the Feynman rules to construct a corresponding mathematical expression. These rules of course are well known. We emphasize that our goal in this manuscript is not only to apply those rules, but in fact to automate the entirety of the process. Therefore, we carefully express here those rules, to orient the reader:

1. We assign frequency-momenta variables to each line such that conservation at each vertex is satisfied. We call a set of such variables for a given diagram a 'label' and store it as an array. This procedure is outlined in Sec. 4.3.3 and its result is not unique: there are a number of distinct, but mathematically equivalent representations of the diagram integrand. The non-uniqueness of labels is an issue that we will discuss in detail in Sec. 4.3.3.

2. We assign a bare Green's function $\mathcal{G}_0^j = \frac{1}{X^j - \epsilon^j}$ to each solid line j with $j = 1, 2, ..., N$, where N is the number of solid lines, X^j represents the frequency, and ϵ^j the energy (see Sec. 4.3.2).

3. Each interaction line connecting two solid lines with spins σ and σ' should be directed and associated with $V_{\sigma,\sigma'}(\mathbf{q})$, where $\mathbf{q}$ is determined via conservation rules at each vertex and is not an independent variable.

4. Each internal Matsubara frequency and momentum is integrated.

5. We note that each fermionic loop has a well-defined spin, which can be any half-integer number between $-s$ and $+s$, where s is the total spin. It means that for a diagram with F_{ζ_m} loops one should multiply the integrand by $(2s+1)^{F_{\zeta_m}}$. Thus, the result should be multiplied by $\frac{(-1)^{m+F_{\zeta_m}}(2s+1)^{F_{\zeta_m}}}{(2\pi)^{nd}\beta^n}$ where m is the order (number of interaction lines) of the diagram, F_{ζ_m} is the number of fermionic loops in the diagram, d is the dimensionality of the system, n is the number of independent frequencies, and β is the inverse temperature. [25]

6. If the jth solid line closes on itself, i.e., a tadpole occurs, we insert a convergence factor, $e^{X^j 0^+}$.

These rules are applied to each diagram resulting in (up to convergence factors) the

Feynman integral of the form

$$D_{\zeta_m} = \frac{1}{(2\pi)^{nd}\beta^n} \sum_{\{\mathbf{k}_n\}} \sum_{\{\nu_n\}} A(m, s, F_{\zeta_m}) \prod_{j=1}^{N} \mathcal{G}_0^j(\epsilon^j, X^j) \prod_{m=1}^{M} V_{\sigma,\sigma'}(\mathbf{q}_m), \tag{4.1}$$

where N and M are the number of fermionic (solid) and bosonic (wavy) lines in the diagram, respectively, and $A(m, s, F_{\zeta_m}) = (-1)^{m+F_{\zeta_m}}(2s+1)^{F_{\zeta_m}}$. Finally, an arbitrary diagrammatic expansion Q can be written as the sum of each distinct diagram at each order

$$Q(x_{ext}) = \sum_{m=0}^{\infty} \sum_{\zeta_m} D_{\zeta_m}, \tag{4.2}$$

where the sum over ζ_m is over all unique topologies of order m. The result only depends on a set of external parameters, x_{ext}, which includes external frequencies, external momenta, chemical potential, and the temperature of the system.

4.3.2 Evaluation of Matsubara Frequency Summations

Each diagram in the perturbative expansion defined by Eq. (4.1) consists of summations over Matsubara frequencies and over momenta within the first Brillouin zone. We perform the (unbounded) Matsubara sums using algorithmic Matsubara integration (AMI) introduced in Ref. [20]. The Matsubara summations of a given Feynman diagram D_{ζ_m} are contained in the factor

$$I_{\zeta_m} = \frac{1}{\beta^n} \sum_{\{\nu_n\}} \prod_{j=1}^{N} \mathcal{G}_0^j(\epsilon^j, X^j) \tag{4.3}$$

of Eq. (4.1). Essentially, AMI is a procedure that evaluates the Matsubara sums by iteratively applying residue theorem to Eq. (4.3). We briefly review AMI here.

Symbolic Array Representation of the Bare Green's Functions

The first step in AMI is to represent the bare Green's functions $\mathcal{G}_0^j(\epsilon^j, X^j)$ in a symbolic array form. We use the self-energy function as an example, which has one external frequency and one external momentum.

For a given diagram D_{ζ_m} with n independent (internal) Matsubara frequencies we define the frequency of each line as the linear combination $X^j = \sum_{\ell=1}^{n+1} i\alpha_\ell^j \nu_\ell$, where the allowed values for the coefficients α_ℓ^j are zero, plus one, or minus one. We store these coefficients as an array of length n, $\vec{\alpha}^j = (\alpha_1^j, ..., \alpha_n^j)$ for the j-th solid line of the diagram. Similarly the free particle energy is $\epsilon^j = \epsilon(\mathbf{k}_j)$, where $\mathbf{k}_j = \sum_{\ell=1}^{n+1} \alpha_\ell^j \mathbf{k}_\ell$. In this notation ν_{n+1} and $\mathbf{k}_{n+1}$ are the external frequency and momenta, respectively.

We will also need to express ϵ^j in an array form. For a given diagram, the jth line (out of N total solid lines) has an energy ϵ^j, which will be one of r symbolically different energies e_ℓ, where $\ell \leq r$. This allows us to represent ϵ^j as an array $\vec{E}_\ell$ with length N, where the ℓth entry takes the value 1 and the rest are zero:

$$\epsilon^j = e_\ell \rightarrow \vec{E}_\ell = (\delta_{\ell,1}, \delta_{\ell,2}, ..., \delta_{\ell,N}), \tag{4.4}$$

where $\delta_{\ell,j}$ is a Kronecker delta. We are now able to represent each Green's function, $\mathcal{G}_0^j$, as an array with length $N + n$: *

$$\mathcal{G}_0^j(\epsilon^j, X^j) \rightarrow [\vec{E}_\ell, \vec{\alpha}^j]. \tag{4.5}$$

The array representation (4.5) is equivalent to a full symbolic representation of the bare Green's functions in the frequency-momenta space.

*Note that the this array representation enables us to store both frequency and dispersions symbolically, while in Ref. [20] only frequency part is stored symbolically.

AMI Procedure

Eq. (4.5) enables us to represent the product of the bare Green's functions in Eq. (4.3) as a nested array of size $N \times (N+n)$:

$$\prod_{j=1}^{N} \mathcal{G}_0^j(\epsilon^j, X^j) \to \left[[\vec{E}_{\ell_1}, \vec{\alpha}^1]; [\vec{E}_{\ell_2}, \vec{\alpha}^2]; ...; [\vec{E}_{\ell_N}, \vec{\alpha}^N] \right]. \tag{4.6}$$

To clarify this, we provide in the Supplemental Material [26] the array representation of a particular third order self-energy diagram as an example.

Starting with the array representation (4.6) and following the AMI procedure [20] we construct and store the AMI result. A typical AMI result contains many terms, which are represented as nested arrays. Each array contains two entries. The first entry is the energy (momenta) part E, which is represented by an array $\vec{\mathcal{E}}$ which is a linear combination of $\vec{E}_\ell$ arrays defined by Eq. (4.4). The symbolic energy in general is constructed by $E = \sum_\ell \mathcal{E}_\ell e_\ell$, where the allowed values for $\mathcal{E}_\ell$, the elements of $\vec{\mathcal{E}}$, are zero, plus one, or minus one. The second entry of the array is the frequency part, which is a linear combination of the $\vec{\alpha}^j$ arrays. From the AMI result the full symbolic result for Matsubara sums (I_{ζ_m} in Eq. (4.3)) is obtained. Thus, for each diagram we have reduced the original problem of Eq. (4.1) to a sum over momenta:

$$D_{\zeta_m} = \frac{1}{(2\pi)^{nd}} \sum_{\{\mathbf{k}_n\}} \mathfrak{D}_{\zeta_m}(i\nu_{n+1}, \{\mathbf{k}_{n+1}\}, \beta, \mu), \tag{4.7}$$

where

$$\mathfrak{D}_{\zeta_m} = A(m, s, F_{\zeta_m}) I_{\zeta_m}(i\nu_{n+1}, \{\mathbf{k}_{n+1}\}, \beta, \mu) \prod_{m=1}^{M} V(\mathbf{q}_m). \tag{4.8}$$

In summary, AMI enables us to analytically evaluate the Matsubara sums of all Feynman diagrams.

4.3.3 Classifying Diagrams via Pole Structure

Typical diagrammatic methods evaluate the perturbation expansion on the imaginary time axis, where the diagrams are positive definite, and this makes the Monte Carlo sign problem more manageable. [14, 15, 27, 28] Evaluation in real time (or real frequency) will encounter a sign problem that is exacerbated by the existence of the canceling diagrams. We seek to address this issue in this and the following sections where we introduce a systematic approach that allows us to identify these canceling diagrams and remove them from the series. In addition, we find groups of equal diagrams, which provides us with a further reduction in computational cost.

Our goal is to evaluate Eq. (4.2) truncated at a cutoff order m_c. However, as we shall see, we do not really need in general to evaluate all the diagrams in the expansion; it turns out that some diagrams are individually vanishing. Furthermore, there exist diagrams that are exactly canceling or equal. To this end we provide a filtering process to systematically identify the individually vanishing, as well as canceling and equal diagrams, without any explicit evaluation of the frequency and momenta summations in Eq. (4.1). This allows us to substantially reduce the diagrammatic space of the problem leading to a significant reduction in the computational cost. In addition, since we eliminate the problematic vanishing and canceling diagrams we markedly suppress the sign problem.

There exist many expansions where *nearly* canceling diagrams appear, e.g., Hubbard self-energy diagrams away from half-filling. In order to manage the sign problem in these cases, we provide a general prescription in Sec. 4.4.2 to carefully treat the nearly canceling pairs.

Labeling Procedure

As mentioned, the label of a Feynman graph is not unique and we need to carefully consider the role of labeling in this challenging problem. It is possible to generate the set of all labels for each diagram in the expansion from which one would construct the corresponding mathematical expressions using the Feynman rules. In the case of self-energy diagrams of order m the number of independent (internal) Matsubara frequencies $n = m$, and the number of internal fermionic lines is $N = 2m - 1$. Thus, knowing the order of a diagram is sufficient to provide a complete accounting of possible labels.

In order to generate each label, we first assign the n independent frequencies to a set of internal fermionic lines. We then assign dependent frequencies via conservation of energy at each vertex. If the conservation law at each vertex is satisfied then a valid label has been found. We generate all the possible labels by systematically choosing n independent lines from N possible choices.

Of course the number of energy conserving labels grows very fast with order, for example, while this number for the fourth order diagrams is of order 10, it is of order 100 by sixth order diagrams making this process more difficult with increasing order. However, although expensive this labeling only needs to be performed once. Furthermore, having a symbolic representation of the labels enables us to analytically extract the poles in the Matsubara frequency space, which as we shall show, plays a crucial role in identifying equal and canceling diagrams.

Diagram Classes

We are interested in identifying diagrams that either are exactly equal or exactly cancel without performing the Matsubara and momenta sums. To begin, we propose to classify diagrams according to the pole structure of their integrands. One may recall

that poles of the Green's functions have a physical manifestation as quasiparticles. If two diagrams are to be analytically equivalent (up to a sign), then they must contain the same set of non-removable divergences (virtual quasiparticles) in order to produce the same integral result. This can only be true if the original integrands have the same pole structure.

We define the *pole configuration* of a diagram D_{ζ_m} to be a set of integers $(n_1, n_2, \cdots, n_{max})$, where n_i is the number of poles with multiplicity i in the Matsubara frequency space and max is the highest possible multiplicity of poles. Clearly, $\sum_{i=1}^{max} n_i = N$, the number of internal fermionic lines. It is important to note that the pole configuration does not depend on the choice of label of a diagram. In this way, we partition the set S^m of diagrams of order m into label-independent subsets C_i^m of diagrams with the same pole configuration. We refer to these subsets as diagram classes. We illustrate this schematically in the top part of Figure 4.4.

Since it is not possible for diagrams that belong to different classes to be equivalent (or cancel) we need only look *within* classes for equal or canceling diagrams.

Diagram Subclasses

Now that we have grouped diagrams according to their pole configuration into classes C_i^m, we search for subclasses containing equal or canceling diagrams. To this end, we now consider the distinct choices of a diagram's label, since how one chooses to label a given diagram might obscure its analytic equality or negation to another diagram in its class. Thus, we need a stronger condition in order to establish subclasses. We postulate then a *necessary* condition in order for two diagrams D_1 and D_2 to be equal or canceling:

- For *any* chosen label of D_1 there must exist a representation of D_2 for which the integrands of D_1 and D_2 are equivalent or canceling.

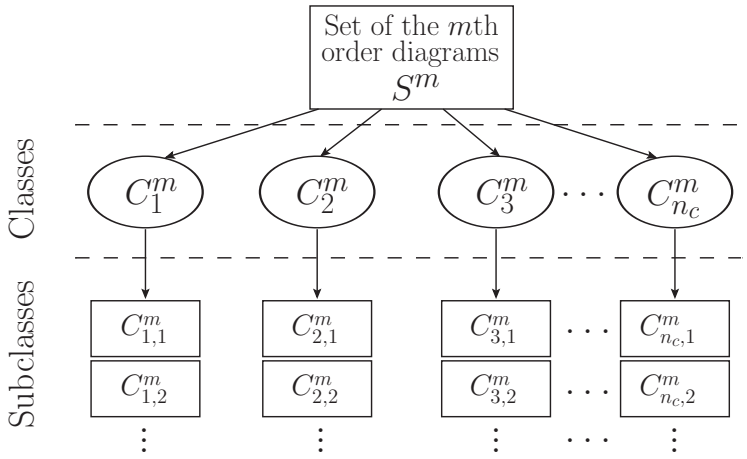

Figure 4.4: Schematic illustration of classes and subclasses of the set S_m of diagrams of order m. Diagrams in a class C_i^m have the same pole configuration, which are divided into subclasses of diagrams with similar characters.

This simple postulate leads to the logical conclusion that the total number of unique labels of D_1 and D_2 must be equal, or else the two diagrams cannot be equal or canceling in general. With this in mind we suggest a label-dependent identifier for a given integrand, which can be constructed by counting the number of poles with respect to each internal and external Matsubara frequency, $i\nu_i$, $x_i = \sum_{j=1}^{N} |\alpha_i^j|$. We then group these numbers into a set $(x_1, x_2, ..., x_{n+1})$, in which we then order the first n entries from highest to lowest as $x = (x_i, x_j, x_k, ..., x_{n+1})$ where $x_i \geq x_j \geq x_k$. (As above, we use self-energy diagrams, with one external frequency and n internal frequencies, as an example). We call this object, x, the *pole-ID* for a given integrand. We now define *diagram character* to be the complete set of pole-IDs generated by considering all possible labels of a diagram. Thus, the diagram character is label-independent. We can therefore safely divide each class C_i^m into subclasses $C_{i,j}^m$ of diagrams with the same diagram character. The bottom part of Figure 4.4 shows schematically the division of each class C_i^m into subclasses $C_{i,j}^m$.

As an example, we show in Figure 4.5 twelve of the diagrams that contribute to

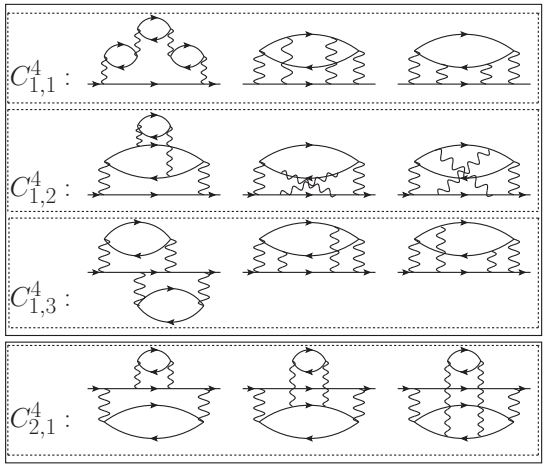

Figure 4.5: Four subclasses of fourth order self-energy diagrams. The diagrams in the top panel belong to class C_1^4 with pole configuration (7,0) and the diagrams in the bottom panel belong to class C_2^4 with pole configuration (5,1). Collecting pole-IDs for all possible labels, one finds out that the diagrams in each row have the same diagram character, i.e., they belong to the same subclass. Thus, one takes the diagrams in each row as candidates to be either equal or canceling.

the self-energy expansion at fourth order. These are divided into two classes, C_1^4 and C_2^4. Class C_1^4 is further divided into three subclasses. One notes that in each row we observe a pair of diagrams that are isomorphic when one neglects the direction of the fermionic lines. We call such (non-isomorphic) diagrams, 'almost isomorphic'. However, within each subclass there are also diagrams with wildly different topologies.

Since there can be no equal or canceling diagrams that do not belong to the same subclass we need only compare diagrams belonging to the same subclass. Thus, the diagram character acts as a unique barcode or fingerprint that can be used to quickly group diagrams. When the number of graphs in a subclass is large, further filtering can be helpful, which we discuss next.

4.3.4 Diagram Filter

Up to now we have only postulated that diagrams belonging to the same subclass are likely to be equal or canceling. We can identify those diagrams which are equal up to a sign by applying transformations to their integration variables such that their integrands remain equivalent. To this end, we introduce a filter, which we call *graph invariant transformations* (GIT). GIT identifies vanishing, canceling and equal diagrams within the subclasses.

Graph Invariant Transformations (GIT)

We begin the GIT procedure by selecting a pair of diagrams D_1 and D_2. We then choose *one* label for each of D_1 and D_2 with their integrands stored in the array representations described in Sec. 4.3.2, which we call L_1 and L_2. Next we apply transformations to one of the labeled integrands and look for equality/negation. These transformations must be such that they change the integrand but not the integral over internal parameters.

We identify three important transformation types. The set of transformations $\mathcal{T}_1$ swaps two of the independent Matsubara frequencies,

$$\mathcal{T}_1 : (i\nu_p, \mathbf{k}_p) \leftrightarrow (i\nu_{p'}, \mathbf{k}_{p'}). \tag{4.9}$$

We note that $\mathcal{T}_1$ is equivalent to a relabeling of the diagram that guarantees a new momentum conserving label. The second transformation $\mathcal{T}_2$ flips the sign of one of the internal fermionic frequencies and corresponding momentum,

$$\mathcal{T}_2 : (i\nu_p, \mathbf{k}_p) \to (-i\nu_p, -\mathbf{k}_p). \tag{4.10}$$

Finally, for many problems there is another transformation $\mathcal{T}_3$ under which the dispersion of (at least) one of the solid lines changes sign:

$$\mathcal{T}_3 : \epsilon^j \to -\epsilon^j. \tag{4.11}$$

We apply the group of all possible transformations (including combinations of $\mathcal{T}_1$, $\mathcal{T}_2$ and $\mathcal{T}_3$) to the integrand of the diagram, with each result stored as array representations. Diagram D_1 equals or cancels diagram D_2 if there is a transformation $\mathcal{T}$ such that $\mathcal{T} : L_1 = \eta L_2$ with $\eta = \pm 1$. In practice, our procedure compares $\mathcal{T} : L_1$ with L_2 after each transformation and stops when such a transformation is found.

GIT also enables us to identify the vanishing diagrams. To do so we start by selecting a diagram D with its integrand represented by the array L. Then we apply GIT to look for a transformation $\mathcal{T}$ such that $\mathcal{T} : L = -L$. If such a transformation is found the diagram D is trivially vanishing.

Application of GIT

In order to identify canceling and equal diagrams one needs to apply GIT to pairs of diagrams within each subclass. However, some considerations can substantially reduce the number of pairs to be investigated. For systems with particle-hole symmetry one can show that almost isomorphic diagrams are always either canceling or equal. Therefore, one should first apply GIT to almost isomorphic diagrams. As an example, we show in Figure 4.6 a pair of almost isomorphic third order diagrams which are found to be canceling by application of GIT. However, application of GIT also finds pairs of diagrams which are not 'almost isomorphic' which nevertheless are found to be equal or canceling. For example, the fourth order diagrams shown in Figure 4.5 are all equal to each other within each subclass.

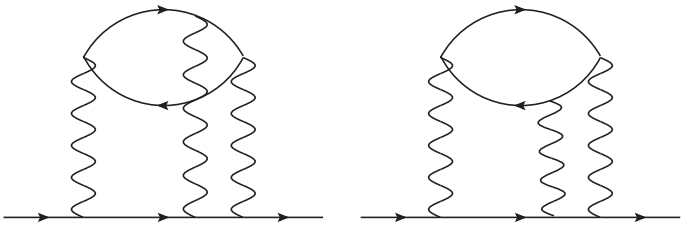

Figure 4.6: Two topologically distinct third order self-energy diagrams which are almost isomorphic. Application of GIT reveals that they are precisely canceling at half-filling.

In practice, to apply the GIT procedure we first select each diagram's label such that the number of times the external frequency appears in the label is maximized. We then investigate these two diagrams using the GIT procedure. This allows us to identify most (but not all) of the equal and canceling diagrams. We then cycle through all possible labels until we find a match (equal or canceling) or exhaust all possible labels, in which case the diagrams are not equal or canceling. In addition, because the comparison *is* label dependent it follows that if the pole-IDs of two labeled graphs are not equivalent then the GIT can not show the equality or negation of the graphs for these specific labels. Thus, it is sufficient to only apply GIT to pairs of labeled diagrams with equivalent pole-IDs.

We emphasize that our approach is fundamentally different from what is proposed in Ref. [1]. In this work we identify canceling/equal diagrams by systematically applying graph invariant transformations to symbolic representations of the diagrams while in Ref. [1], diagrams are presumed to cancel via crossing symmetry. Although some cancellations due to crossing symmetry can occur for special cases, the general application of that approach is almost guaranteed to pair diagrams with different pole structures - which precludes the diagrams from canceling in general. As we shall see in Sec. 4.4.2 identifying the labels and corresponding transformations that map diagrams to their canceling partners enables one to obtain the optimal cancellation

during momenta integration. We therefore believe that by applying GIT we construct the optimally sign-blessed groups for any Feynman diagrammatic expansion composed of the bare Green's functions.

4.3.5 Evaluation of Momenta Summations

The final step in evaluating the diagrams in a perturbative expansion is to perform the momenta integrations. Since these are high-dimensional integrals one typically uses Monte Carlo integration. This will be efficient if the number of diagrams in the expansion is not too large. In this approach we sample internal momenta points uniformly from $[-\pi, \pi]^d$ following standard Monte Carlo procedure. [29] We generate y samples in the internal momenta space each denoted by $\{\mathbf{p}_n\}_i$ and approximate each diagram D_{ζ_m} by

$$D_{\zeta_m} \simeq D^{(y)}_{\zeta_m} = \frac{(2\pi)^{nd}}{y} \sum_{i=1}^{y} \mathfrak{D}_{\zeta_m}(i\nu_{n+1}, \{\mathbf{p}_n\}_i, \mathbf{k}_{n+1}, \beta, \mu), \tag{4.12}$$

from which the series expansion of Q is calculated:

$$Q \simeq \sum_{m=0}^{\infty} \sum_{\{\zeta_m\}} D^{(y)}_{\zeta_m}(i\nu_{n+1}, \mathbf{k}_{n+1}, \beta, \mu). \tag{4.13}$$

For problems with a large diagrammatic space the direct evaluation of all the diagrams may be impractical and in that case one combines AMI with Metropolis-Hastings Monte Carlo (MHMC) [30] as in standard DiagMC [10] to numerically evaluate the momenta sums as well as to probe different topologies in the expansion (4.2). This approach is similar to standard DiagMC but with three significant differences. First, we work in the Matsubara frequency space, similar to recent works on the diagrammatic dual Fermion method, [31, 32] rather than imaginary time space. Second, we

generate all the diagrams and their corresponding mathematical expressions before the MC simulation instead of producing the diagrams during the simulation. This, as we shall see, trivializes the detailed balance equations of a MHMC simulation. Third, since we analytically compute and store the Matsubara sums before MC simulation we eliminate the need for probing internal Matsubara frequencies (or, equivalently, internal imaginary times).

To stochastically sample the diagrams we introduce a set of ergodic update procedures to probe diagram orders, diagram topologies, and internal momenta, fixing all other external variables. For each step of the Monte Carlo simulation one of the updates is randomly chosen and the proposed configuration is accepted or rejected according to the Metropolis-Hastings scheme. We note that each diagram is identified by two properties: order (m) and topology (ζ_m). We assume that at order m we have γ_m different topologies in the expansion (4.2). Now we introduce the following updates:

1. Change momenta: The current momenta $\{\mathbf{k}_n\}_c$ of the current diagram of order m are changed to proposed momenta $\{\mathbf{k}_n\}_p$ where the $\{\mathbf{k}_n\}_p$ are derived from the uniform distribution function $W(m)$.

2. Change topology: By this update a diagram topology is changed within a specific order, i.e., if the current diagram is of order m with topology ζ_m^c another diagram of order m with topology ζ_m^p from the stored diagrams is proposed.

3. Change order: The current diagram of order m_c and with topology $\zeta_{m_c}^c$ is changed to a diagram of order m_p and with topology $\zeta_{m_p}^p$.

Note that the proposed mth order topology is chosen uniformly from γ_m possible topologies with probability $\frac{1}{\gamma_m}$. Finally, the acceptance probability of these updates

in the Metropolis-Hastings scheme is expressed as

$$A = \mathrm{Min}\left[1, \frac{\gamma_{m_p}}{\gamma_{m_c}} \frac{|\mathfrak{D}^{re/im}_{\zeta^p_{m_p}}(i\nu_{n+1}, \{\mathbf{k}_{n+1}\}_p, \beta, \mu)| W(m_c)}{|\mathfrak{D}^{re/im}_{\zeta^c_{m_c}}(i\nu_{n+1}, \{\mathbf{k}_{n+1}\}_c, \beta, \mu)| W(m_p)}\right], \tag{4.14}$$

where $|\mathfrak{D}^{re/im}_{\zeta_m}|$ is the absolute value of the real/imaginary part of $\mathfrak{D}_{\zeta_m}$ and $W(m) = 1/(2\pi)^{md}$.

It is typical in MHMC to seek an update criterion that minimizes computational expense. Unfortunately, here one has no option but to evaluate the entire AMI integrand $\mathfrak{D}_{\zeta_m}$, which becomes expensive at high orders making it difficult to generate sufficient statistics.

4.4 Example: Self-Energy for the 2D Square Lattice Hubbard Model

As an application of our method, we calculate the self-energy for the Hubbard model on a two-dimensional square lattice up to sixth order in perturbation theory. We consider the nearest neighbor tight binding dispersion given by $\epsilon(\mathbf{k}) = -2t\Big(\cos k_x + \cos k_y\Big) - \mu$ where t is the hopping amplitude and μ is the chemical potential. In this model, the potential is the momentum-independent local Hubbard interaction, $V_{\sigma,\sigma'}(\mathbf{q}) = U\delta_{\sigma,-\sigma'}$. The self-energy is

$$\Sigma(\mathbf{k}_{n+1}, \nu_{n+1}) = \sum_{m=1}^{m_c} \left\{ \sum_{\{\zeta_m\}} \frac{(-1)^{m+F_{\zeta_m}} U^m}{(2\pi)^{2m}\beta^m} \sum_{\{\mathbf{k}_m\}} \sum_{\{\nu_m\}} \prod_{j=1}^{2m-1} \mathcal{G}_0^j(\epsilon^j, X^j) \right\} + O(U^{m_c+1}), \tag{4.15}$$

evaluated to a cutoff order, m_c. Here we remind the reader that a self-energy diagram of order m has $2m-1$ internal fermion lines and m independent frequencies and

Table 4.1: Diagrammatic space reduction by shifting the chemical potential for the Hubbard self-energy expansion up to sixth order. $N_{init}^{(m)}$: Total number of mth order Hubbard self-energy diagrams in the original expansion. $N^{(m)}$: Total number of mth order Hubbard self-energy diagrams neglecting all one-legged diagrams by applying a chemical potential shift.

m	1	2	3	4	5	6
$N_{init}^{(m)}$	1	2	8	44	296	2312
$N^{(m)}$	0	1	2	12	70	515

momenta.

Since the Hubbard interaction only occurs between fermionic lines with opposite spins, we construct and store only those connected one-particle irreducible diagrams that satisfy this criterion. The total number of diagrams at each order $N_{init}^{(m)}$ is given in the first row of Table 4.1. We then find all the possible labels (as explained in Sec. 4.3.3) for each stored diagram, which enables us to construct the classes and subclasses of the self-energy diagrams.

4.4.1 Diagrammatic Space Reduction for the Hubbard Self-Energy

We first note that the contribution of diagrams with tadpole insertions (one-legged diagrams) can be neglected because they are equivalent to shifting the chemical potential $\mu \to \mu - \bar{n}U/2$, where $\bar{n}$ is the number of electrons per site. [33, 34] In doing so we in fact redefine the chemical potential and self-energy function such that $\mu = 0$ corresponds to half-filling. [35] As shown in Table 4.1 this standard procedure substantially reduces the number of diagrams from $N_{init}^{(m)}$ to $N^{(m)}$. We then find all possible labels (as explained in Sec. 4.3.3) for each diagram in order to classify the diagrams into subclasses; then we apply the GIT procedure within each subclass to identify

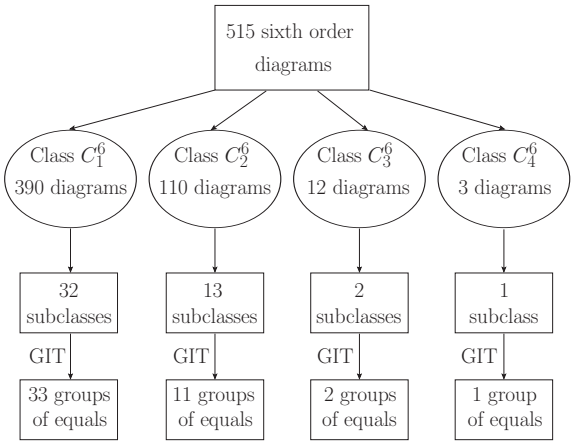

Figure 4.7: Schematic illustration of constructing groups of sixth order equal self-energy diagrams at half-filling. There are 515 diagrams after the chemical potential shift at sixth order. We first divide the diagrams into classes according to their pole configurations. Note that C_1^6, C_2^6, C_3^6, and C_4^6 are classes of diagrams with pole configurations $(11, 0, 0)$, $(9, 1, 0)$, $(7, 2, 0)$, and $(8, 0, 1)$, respectively. We then construct the subclasses for each class considering their diagram characters. Finally, the application of GIT within each subclass enables us to discard all the canceling diagrams and find groups of equal diagrams at half-filling.

vanishing, equal, and canceling diagrams at half-filling.

The transformations $\mathcal{T}_1$ and $\mathcal{T}_2$ are given by (4.9) and (4.10), respectively, and the transformation $\mathcal{T}_3$ is a (π, π) shift of internal momentum,

$$\mathcal{T}_3 : \mathbf{k}_p \to \mathbf{k}_p + (\pi, \pi), \tag{4.16}$$

which flips the sign of ϵ^j at half-filling if it depends on $\mathbf{k}_p$. Since the potential U is a constant and the momenta sums are performed over the first Brillouin zone the expansion (4.15) is invariant under any arbitrary combination of these transformations.

In the third order there are only two diagrams, shown in Figure 4.6. These two diagrams belong to the same subclass and the GIT procedure finds that they cancel. In the Supplemental Material [26], we explicitly present the transformations which relate

these two diagrams. The twelve fourth order diagrams are divided into two classes, which subdivide into a total of four subclasses containing three diagrams each (see Figure 4.5). The GIT procedure reveals that the diagrams within each subclass are precisely equal in agreement with what has been reported previously. [36–38] There are 70 fifth order diagrams divided into 11 subclasses; GIT reveals that all of the diagrams within each subclass exactly cancel. At sixth order we have 515 diagrams divided into four classes and 48 subclasses. Applying GIT, we identify 144 canceling diagrams at half-filling; the remaining 371 diagrams are collected into 47 sets of equal diagrams. The details of the diagrammatic space reduction for sixth order diagrams are illustrated in Figure 4.7. It is important to note that all precise cancellations found by the GIT procedure occur at half-filling only.

The diagrammatic space reduction for the Hubbard self-energy expansion up to sixth order is summarized in Table 4.2. There are no odd-order diagrams in the reduced space, since each diagram has a precisely canceling partner; i.e., at half-filling odd order diagrams do not contribute to the self-energy. [39] To calculate the self-energy at half-filling, one needs to evaluate one diagram from each group, multiplied by the number of diagrams in each group. Altogether this represents a huge reduction: at sixth order we began with 515 diagrams (not including one-legged diagrams); the GIT procedure reduces this number to only 47 nonequivalent diagrams.

4.4.2 Sampling Nearly canceling Diagrams Away from Half-Filling

In practice *all* diagrams within each subclass should be stored in order to evaluate a given quantity away from half-filling. Diagrams which cancel at half-filling will nearly cancel away from half-filling, and the identification of those nearly canceling pairs can increase the efficiency of Monte Carlo integration.

Table 4.2: Diagrammatic space reduction of the Hubbard self-energy up to sixth order at half-filling. In the second row, $n_{tot}^{(m)}$ is the number of subclasses at each order m, and $(N^{(m)})$ is the total number of diagrams (not including one-legged diagrams) at each order m (see Table 4.1). In the last row, $N_r^{(m)}$ is the number of groups of equal diagrams at each order m, and $(n_d^{(m)})$ is the total number of non-canceling diagrams at each order m.

m	1	2	3	4	5	6
$n_{tot}^{(m)}(N^{(m)})$	0(0)	1(1)	1(1)	4(12)	11(70)	48(515)
$N_r^{(m)}(n_d^{(m)})$	0(0)	1(1)	0(0)	4(12)	0(0)	47(371)

The most straightforward way to evaluate diagrams away from half-filling is to sample the diagrams in each subclass as a whole instead of sampling diagrams one-by-one. However, to use the full power of the GIT in Monte Carlo integration away from half-filling one should group each nearly canceling pair as a single integrand during the stochastic sampling. If a pair of diagrams D_1 and D_2 are exactly canceling at half-filling, we essentially have a transformation $\mathcal{T}$ found by GIT and the necessary array representations L_1 and L_2, such that $\mathcal{T} : L_1 \to -L_2$ for every set of internal variables. One should then evaluate the pair of diagrams by considering $(\mathcal{T} : L_1) + L_2$ as a whole in the Monte Carlo sampling away from half filling. This optimizes the cancellation between the two diagrams. Thus, instead of sampling the nearly canceling diagrams one-by-one, we sample them as a pair. This substantially improves the average sign and the uncertainty due to the huge cancellation.

4.4.3 Numerical Results

In this section we provide proof of concept results to illustrate the applicability of the method to the difficult problem of the Hubbard interaction. To do this we will first consider the order-by-order contributions for a point away from half-filling, on both the Matsubara and real frequency axes, in order to discuss the role of error

induced by truncating the series. Subsequently we will compare our AMI calculations at half-filling to results from dynamical cluster approximation (DCA) [22, 28, 40, 41] as well as compare the results from AMI on the real-frequency axis to those obtained via numerical analytic continuation of DCA data. Finally we will compare our results on the Matsubara axis throughout the Brillouin zone to numerically exact results.

A central issue in truncated diagrammatic expansions for Hubbard interactions is that for large enough value of U/t the truncated series is not convergent. [42] To avoid this there are methods to improve convergence that in essence re-weight each diagram order without changing the sum of the entire series. [15, 43, 44] Here, we would like to avoid any rescaling or resummation and instead we operate within the range of explicit convergence of the series. In order to do so, in each case we estimate our truncation errors (see Supplemental Material [26] for a derivation) by considering the behavior of coefficients at each order. We can then use this information to evaluate the series for values of U/t such that the truncation error is small.

As a first example, shown in Figure 4.8, we consider a case without particle-hole symmetry (i.e., away from half-filling), which means that all diagrams at each order (including odd orders) must be included. Ignoring one-legged diagrams, this requires the evaluation of $N^{(m)}$ diagrams at each order m (the last row of Table 4.1) where at each order the diagrams are grouped into $n_{tot}^{(m)}$ subclasses (see Table 4.2). The coefficients a_m in the self-energy expansion $\Sigma = \sum_m a_m U^m$ are evaluated for parameters $\beta t = 5$ and $\mu/t = -1.5$ at $\mathbf{k} = (\pi/8, \pi)$ for $U/t = 1$ to 4. We normalize each plot by the absolute value of the second order term. For $U/t \leq 2$ we see that the 4th, 5th and 6th order contributions are negligible; however for $U/t = 4$, these contributions are comparable to each other in magnitude. These findings are consistent with the truncation error, plotted in the inset to Figure 4.8. The fractional truncation error $err^{(m)}$ is the error estimate for truncating the series at order m, shown for $m = 4, 5$.

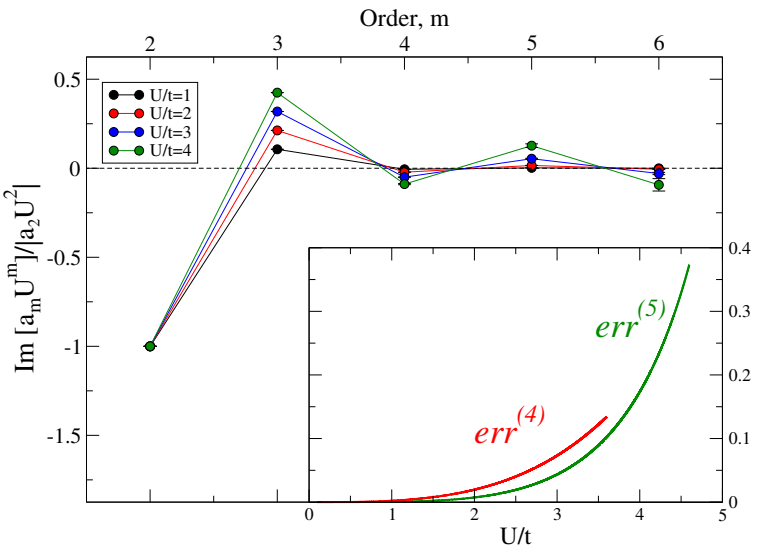

Figure 4.8: The contribution at each order to $\mathrm{Im}\Sigma_{\mathbf{k}}(i\nu_0)$ for $U/t = 1 \to 4$ normalized by the $m = 2$ contribution. Data are for parameters $\beta t = 5$ and $\mu/t = -1.5$ at $\mathbf{k} = (\pi/8, \pi)$. The AMI results were obtained with $\approx 10^6$ samples per diagram.

We see that up to $U/t = 2$ the truncation error is negligible ($err^{(5)} < 1\%$) while at $U/t = 4$ the error is $\approx 15\%$ and becomes divergent slightly above $U/t = 4$. The fourth order truncation error $err^{(4)}$ has only minor differences compared to $err^{(5)}$. This suggests that at this temperature ($\beta t = 5$) and values of U/t as large as 4, a diagrammatic series might be reasonably approximated by neglecting terms higher than 5th order. Actually, it is surprising that, for a wide range of U/t values, 4th or 5th order results should produce truncation errors $< 10\%$. Such behavior has been observed at strong coupling from ΣDDMC, [13, 15] where the results of the diverging series at higher order oscillate around the result such that the sum of all higher order terms is only a small contribution for weakly coupled cases, though this ceases to be the case for large values of U/t.

One should also note that to get reliable error bars for higher order contributions, grouping the diagrams into subclasses is essential. By measuring each group separately we effectively reduce the variance of each measurement. This is optimized when the diagrams in a group are equal and the variance represents sampling from the analytic

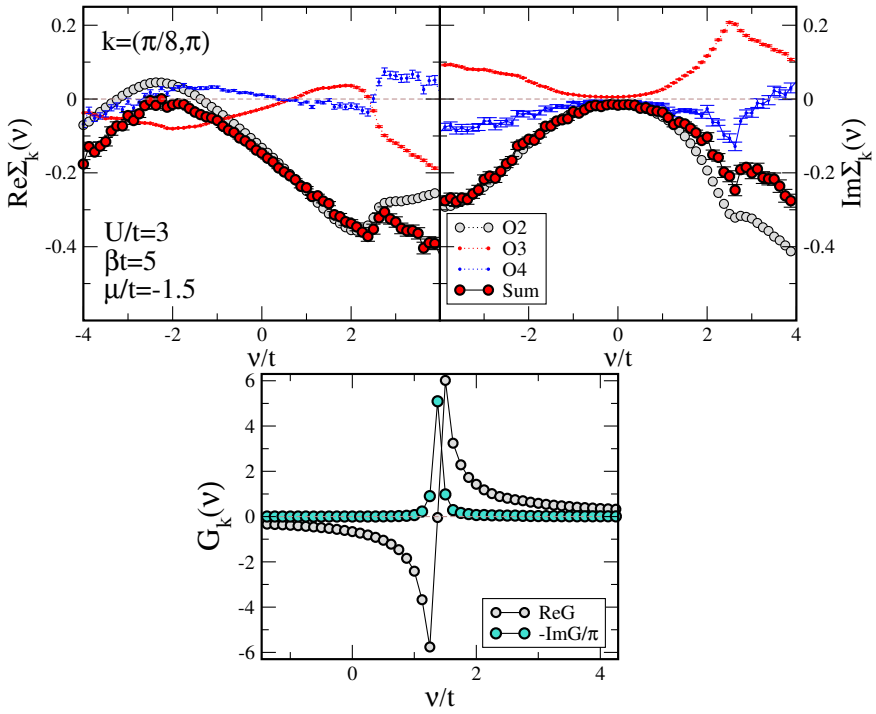

Figure 4.9: *Top*: Real and imaginary parts of the self-energy at second, third and fourth order as well as the result up to fourth order vs. real frequency ν, *Bottom*: Green's function up to fourth order vs. real frequency ν. Data are for parameters $U/t = 3$, $\mu/t = -1.5$, and $\beta t = 5$ at $\mathbf{k} = (\pi/8, \pi)$. We set $\Gamma/t = 0.05$ in the symbolic analytic continuation $i\nu_n \to \nu + i\Gamma$. The AMI results were obtained with $\approx 4 \times 10^7$ samples per diagram.

expression for a single diagram.

We show another example away from half-filling in Figure 4.9 but now evaluated on the real frequency axis at $U/t = 3$ for $\beta t = 5$ and $\mu/t = -1.5$. Since this parameter choice is within the convergence criteria mentioned in Figure 4.8 we expect small truncation errors, and our results up to 4th order illustrate the utility and rather high accuracy attainable with the method. For completeness we show the real and imaginary parts of the self-energy and each contribution from mth order (Om) as well as the sum up to 4th order. At each order the result is evaluated by forming subclasses and evaluating all diagrams of a subclass together. Of interest is the partial cancellation between 3rd and 4th order contributions for much of the frequency range.

As a result, by comparing the $O2$ result to the entire sum we find a wide range of frequencies ($\nu = -1$ to 2.5) where both the real and imaginary parts of the 2nd order diagram are nearly equivalent to the sum up to 4th order. Also shown in the lower panel are the real and imaginary parts of the Green's function resulting from the self-energy sum in the upper panels. One notes a typical form of the Green's function and can identify at which frequency ReG changes sign, which corresponds to the energy $\epsilon(\mathbf{k}) - \mathrm{Re}\Sigma_{\mathbf{k}}$. The Green's function is essentially independent of Σ far away from this boundary. Thus only self-energies near this boundary, here from $\nu \approx 0.5$ to 2, need to be evaluated to correctly represent the Green's function.

Essential in obtaining these results is managing the divergences of the AMI integrands that arise for evaluation on the real frequency axis. While analytically these divergences always have canceling terms, each individual term might cause numerical overflow that must be managed. To do so, we use two regulators: an intrinsic scattering rate Γ for the analytically continued frequency $i\nu_n \to \nu + i\Gamma$ that provides a width to the imaginary parts of the Green's functions; and a thermal regulator η which enters the bosonic distribution functions in the $E \to 0$ limit. The constraint on these regulators for numerical correctness is that they be much smaller than the dominant energy scale, $\Gamma \ll \nu$ and $\eta \ll k_B T$. Operating outside this constraint will typically result in overly smoothed results, or reduced numerical values. Our calculations are performed with $\Gamma/t = 0.05$ and $\eta = 10^{-5}$, though somewhat larger values can be used to improve statistical uncertainty without visible change to the result. In addition to these regulators, for some diagrams there may exist terms in the AMI integrand that have no external frequency in the denominator and only a linear combination of energies. This results in a large number of spurious poles inside the integration space of size mD for D dimensions that are not regulated by Γ nor by η. One needs only to avoid the direct evaluation of the integrand at these poles to obtain correct results.

To do so it is essential that the momentum integrals *not* be performed on a regular $L \times L$ grid. Doing so virtually guarantees evaluation of the integrand directly on a pole. Instead, sampling the space via MC methods by choosing random points in the integration space makes it unlikely to encounter these spurious poles. In addition, this extends the calculation to be effectively continuous in momentum space and provides results directly in the thermodynamic limit.

In a recent work, Vučičević and Ferrero [45] have devised an alternate method of diagram evaluation starting from Eq. (4.1) but they first replace the product of bare Green's functions with a summation by employing a generalization of a partial fractions decomposition. In that work they allude to a number of obstacles that we do not seem to encounter. We suspect that the process of breaking the integrand into partial fractions produces many canceling terms resulting in an unnecessary inclusion of many removable divergences. Avoiding this procedure as well as avoiding the use of a regular $L \times L$ grid, as we have done, has allowed us to use very small regulator in analytic continuation process ($\Gamma/t \approx 0.05$ to 10^{-4}) without particular difficulty. For the chosen parameter regimes we investigate the dependence of the results on Γ and observe that the result has only weak dependence on $\Gamma \leq 0.05t$, i.e., $\Gamma = 0.05t$ is effectively in the limit of $\Gamma \to 0$.

Moving forward, we restrict our calculations to the half-filled model where we make use of the full power of the GIT methodology described in Sec. 4.3.4. We present results truncated again at 4th order and use the sixth order contribution to estimate the truncation error. According to the last row of Table 4.2, we need to evaluate only $N_r^{(m)}$ diagrams for each order m. This amounts to only evaluating five diagrams in total, which can be accomplished extremely quickly. We also provide comparison to established numerical methods DCA and DDMC. [32, 40]

We show in the left-hand frame of Figure 4.10 the imaginary part of the self-

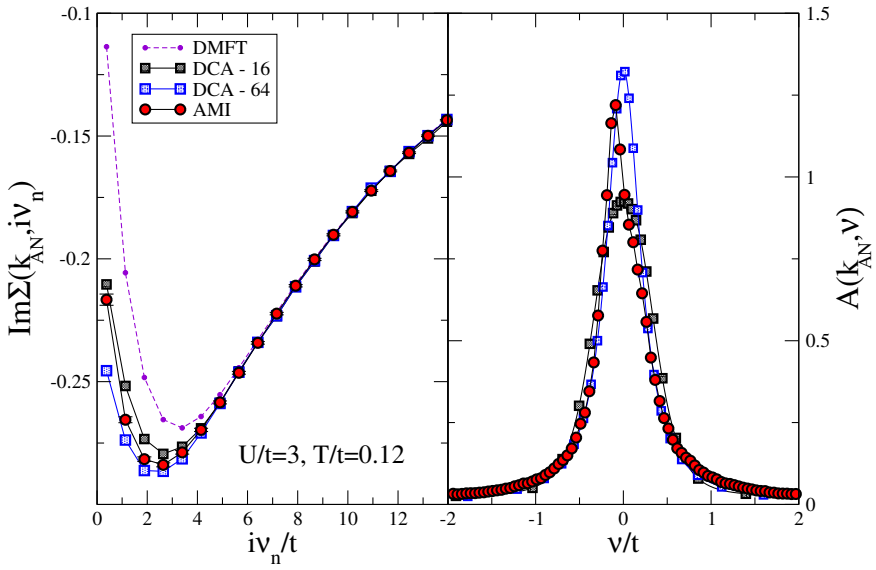

Figure 4.10: *Left*: Imaginary part of the self-energy on the Matsubara axis at $\mathbf{k}_{AN} = (\pi, 0)$ for $\mu = 0$, $U/t = 3$, and $\beta t = 8.33$. Results from DMFT are shown as well as DCA data for 16 and 64-site clusters. *Right*: Spectral function $A(\mathbf{k}_{AN}, \nu)$ on the real frequency axis. The DCA results were obtained via maximum entropy inversion. [17] The AMI results assume $\Gamma/t = 0.05$. The AMI results were obtained with $\approx 10^6$ samples per diagram.

energy vs. Matsubara frequency $i\nu_n$ obtained by the direct evaluation of the diagrams up to 4th order using AMI at the antinodal point $\mathbf{k}_{AN} = (\pi, 0)$ for $U/t = 3$ and $\beta t = 8.33$. The results are in perfect agreement with DCA after only a few frequencies, $(i\nu_n > i\nu_5)$. This is expected since larger values of $i\nu_n$ strongly suppress high order contributions, reducing the truncation error sharply. Comparison to DCA at low frequency shows that the 4th order truncated series is surprisingly competitive with 16→64-site DCA. [38, 46] In general we expect our truncation error to grow for decreasing $i\nu_n$ or decreasing temperature, and here the error bars only reflect statistical uncertainty and do not represent truncation errors.

The power of AMI becomes apparent in the right-hand frame of Figure 4.10 where we plot the real frequency spectral function at the antinodal point. Recall that for AMI the analytic continuation involves only a symbolic replacement of $i\nu_n \to \nu + i\Gamma$

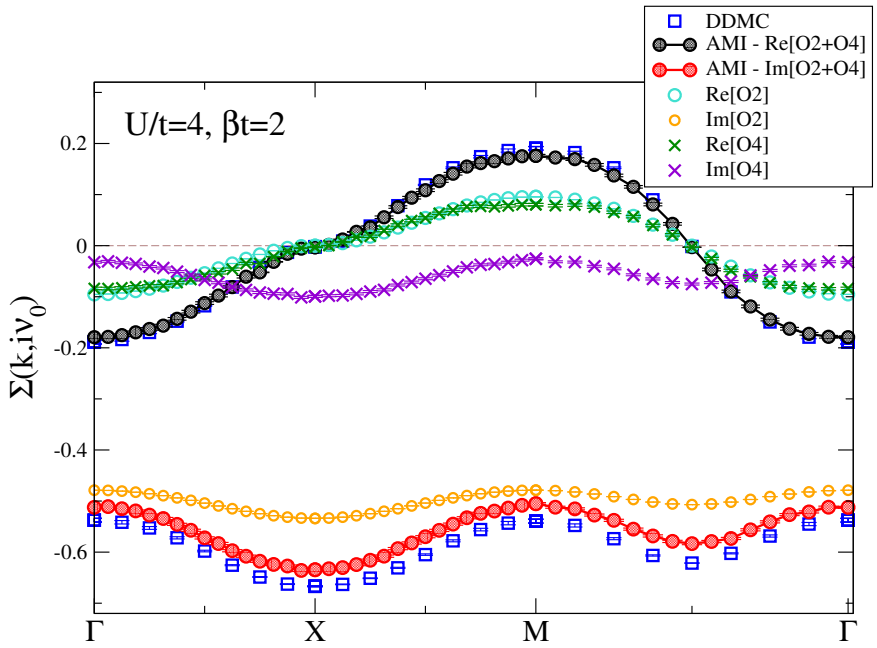

Figure 4.11: Real and imaginary parts of the self-energy at $i\nu_0$ through high-symmetry cuts in the $k_x - k_y$ plane for $\mu = 0$, $U/t = 4$, and $\beta t = 2$. The upper/lower blue squares are the real/imaginary DDMC results from Ref. [47]. The AMI results were obtained with $\approx 10^7$ samples per diagram.

for some sufficiently small value of Γ. The resulting AMI spectral density is shown in red circles. For comparison we perform the numerical analytic continuation [17] for the DCA Green's functions at the antinodal point. Surprisingly we see that the DCA result after numerical analytic continuation has the same broadening as determined by AMI directly on the real-frequency axis. One notes a slight asymmetry in the AMI result evaluated at $\mu = 0$. This is due to a small non-zero value of $\mathrm{Re}\Sigma(\mathbf{k}_F, 0)$. This truncated expansion is not particle-conserving and therefore this represents a density that is very close to, but not equal to, half-filling. Moreover, the AMI result as $\nu \to 0$ may be underestimated due to the energy and thermal regulators. One would need to maintain $\Gamma \ll \nu$ and further that $\Gamma \ll \mathrm{Im}\Sigma(\nu \to 0)$ in order to guarantee correctness. These considerations have not been addressed in this simple example.

As a further benchmark, we compare to DDMC results at half-filling. [47] In Fig-

ure 4.11 we show the real and imaginary parts of the self-energy at the first Matsubara frequency for high-symmetry cuts through the Brillouin zone. For discussion purposes we plot both the individual 2nd and 4th order AMI results as well as their sums. We see that the 2nd order contribution to the imaginary part of the self-energy (orange circles) is much larger than the 4th order contributions (purple crosses). This is not the case for the real part of the self-energy where the 2nd and 4th order contributions are nearly equal, suggesting that the convergent behavior of the real and imaginary parts of the coefficients need not be the same. In both cases the sum of these results are surprisingly similar to the DDMC results and both the real and imaginary parts have the correct qualitative momentum dependence. Visually it appears that the real-part is a better approximation. If we scrutinize the results at the Γ point where the real part has values (-0.179 ± 0.002) and (-0.188 ± 0.004) for AMI and DDMC respectively we find a $\approx 5\%$ discrepancy. Repeating this for the imaginary part with values (-0.511 ± 0.002) and (-0.537 ± 0.004) we find again a $\approx 5\%$ discrepancy, therefore the visual distinction is only a matter of scale, and we find that the relative truncation error is in practice much less than our numerical estimate. In each case, it must be true that the sum of terms of order $m \geq 6$ results only in these small differences. The results are not generally expected to be this accurate for all parameter choices and indeed at lower temperatures we find that the deviation increases. This behavior has also been observed in order-by-order expansions from a diagrammatic treatment of the dual Fermion method. [31, 47]

4.5 Conclusion

We have presented a general framework to evaluate Feynman diagrammatic expansions that can be applied to virtually any expansion with any interaction. Specifically,

our method is applicable to any diagrammatic expansion composed of the bare Green's functions with any frequency-independent two-body interaction.

As proof of concept we presented the application of this method to the self-energy expansion of the Hubbard model on a 2D square lattice with nearest neighbor tight-binding dispersion at and away from half-filling. The resulting diagram groups are provided in the Supplemental Material [26] up to 6th order and these groups are also valid for 1D or 3D systems as well for the imaginary time representation. As evidence of utility we provided a comparison of the low order expansion to other numerical methods and found excellent results when within the convergent range of the series.

While the procedure is a major advancement in evaluating diagrammatics on the real frequency axis, it does not address the factorially growing diagram space, which remains time consuming to evaluate. Further, it does not address the fundamental sign problem inherent in the analytic AMI results and in many cases the average sign remains small after AMI and is not always improved by grouping diagrams. Finally, while AMI allows for the evaluation of any Feynman diagram at any temperature it seems that at low temperature the contributions of higher order terms are larger.

Important features of our method can be summarized as follows. The Matsubara sums are performed analytically using AMI. [20] This allows for the symbolic analytic continuation $i\nu_n \to \nu + i0^+$ without any ill-defined numerical procedure. The full symbolic result of AMI in principle enables us to exactly (up to machine precision) evaluate Matsubara sums of each diagram in the expansion at any temperature, even at the $T = 0$ limit, which is not accessible in DiagMC methods. We also determine the pole structure of the diagrams, which enables us to divide diagrams into groups which contain nearly canceling pairs. We therefore sample pairs of nearly canceling diagrams as a whole in Monte Carlo integration instead of sampling the diagrams one-by-one, which leads to a substantial suppression to the sign problem. Further, in the

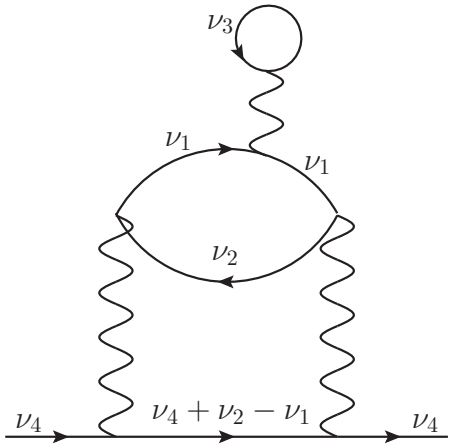

Figure 4.12: A third order diagram in the perturbative expansion of the Hubbard self-energy. We assign a frequency-momenta label to the diagram.

special case when there is particle-hole symmetry the cancellations are *exact*, while other diagrams within each group are exactly equal. Moreover, despite the factorially growing cost, the AMI result and diagram groups can be easily stored, i.e., one needs to solve the problem up to the momenta integrations only once.

4.6 Acknowledgments

JPFL and SHC acknowledge the support of the Natural Sciences and Engineering Research Council of Canada (NSERC) (RGPIN-2017-04253, and RGPIN-2014-057). Computational resources were provided by ACENET and Compute Canada. Our Monte Carlo codes make use of the open source ALPSCore framework [48, 49] and we have used the open source code Maxent [17] for numerical analytic continuation.

4.7 Supplemental material

4.7.1 Example: Array representation of diagrams

Essential to our method is to represent Feynman diagrams in an array form. In this section we provide an example to elucidate the array representation of the Hubbard self-energy diagrams. We consider a third order diagram shown in Figure 4.12. We first assign a frequency-momenta label to the diagram in order to construct the usual symbolic representation. We note that there is a double pole with respect to $i\nu_1$ while other poles are simple. The temporal part of the diagram is then given by (up to a convergence factor)

$$\begin{aligned} I^{(3)} = \frac{1}{\beta^3} \sum_{\nu_1,\nu_2,\nu_3} \mathcal{I}^{(3)} &= \frac{1}{\beta^3} \sum_{\nu_1,\nu_2,\nu_3} \mathcal{G}_0^1(i\nu_1)\mathcal{G}_0^2(i\nu_1)\mathcal{G}_0^3(i\nu_2)\mathcal{G}_0^4(i\nu_3)\mathcal{G}_0^5(i\nu_4 + i\nu_2 - i\nu_1) \\ &= \frac{1}{\beta^3} \sum_{\nu_1,\nu_2,\nu_3} \frac{1}{i\nu_1 - e_1} \frac{1}{i\nu_1 - e_1} \frac{1}{i\nu_2 - e_2} \frac{1}{i\nu_3 - e_3} \frac{1}{i\nu_4 + i\nu_2 - i\nu_1 - e_4}. \end{aligned} \tag{4.17}$$

The denominator of each Green's function in the summand has two terms: energy and linear combination of the frequencies, which can be extracted from the set of α values obtained from the labeling. We first represent the energies in the array form:

$$\begin{aligned} e_1 = \epsilon(\mathbf{k}_1) &\to (1,0,0,0,0), \\ e_2 = \epsilon(\mathbf{k}_2) &\to (0,1,0,0,0), \\ e_3 = \epsilon(\mathbf{k}_3) &\to (0,0,1,0,0), \\ e_4 = \epsilon(\mathbf{k}_4 + \mathbf{k}_2 - \mathbf{k}_1) &\to (0,0,0,1,0). \end{aligned} \tag{4.18}$$

The second part of the jth entry is the array representation of the frequency part of the jth Green's function, which is given by

$$\begin{aligned} i\nu_1 &\to (1,0,0,0), \\ i\nu_2 &\to (0,1,0,0), \\ i\nu_3 &\to (0,0,1,0), \\ i\nu_4 + i\nu_2 - i\nu_1 &\to (-1,1,0,1). \end{aligned} \tag{4.19}$$

We finally achieve the array representation of the summand:

$$\begin{aligned} \mathcal{I}^{(3)} \to \Big[&[(1,0,0,0,0),(1,0,0,0)];[(1,0,0,0,0),(1,0,0,0)];[(0,1,0,0,0),(0,1,0,0)]; \\ &[(0,0,1,0,0),(0,0,1,0)];[(0,0,0,1,0),(-1,1,0,1)]\Big]. \end{aligned} \tag{4.20}$$

Since there is a double pole the first two entries of the array (4.20) are identical, and there are four distinct energies and four Matsubara frequencies.

We recall that in the AMI full analytic result the dispersion and frequency parts in each term are linear combinations of the initial arrays in Eq. (4.18) and Eq. (4.19). The AMI result can be evaluated exactly (up to machine precision) using numeric momenta integration procedures.

4.7.2 Example: Application of GIT

In this section we aim to explicitly demonstrate how one can apply the GIT procedure to determine whether two given diagrams are equal or canceling at half-filling. We consider two third order diagrams, shown in Figure 4.13, arising from the perturbative expansion of self-energy function of the Hubbard model. The first step is to assign a conserving frequency-momenta label to each diagram. Finding the labels enables us

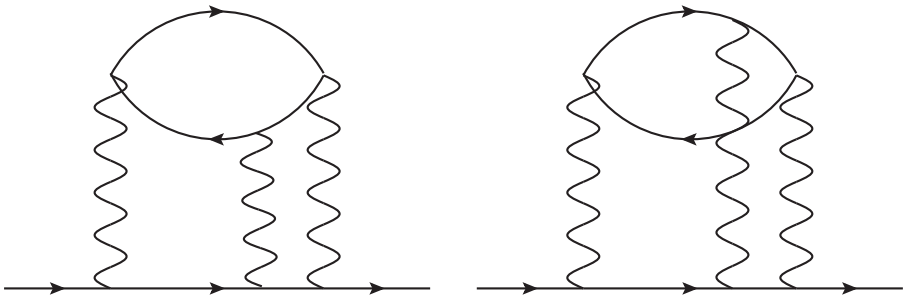

Figure 4.13: Two topologically distinct third order Hubbard self-energy diagrams, which we denote by $\Sigma_1^{(3)}$ and $\Sigma_2^{(3)}$. Since these two diagrams are almost isomorphic one expects them to be either equal or canceling at half-filling.

to construct mathematical expressions of the diagrams:

$$\Sigma_1^{(3)} = \frac{U^3}{\beta^3} \sum_{\{\mathbf{k}\}} \sum_{\{\nu\}} L_1^{(3)}, \tag{4.21}$$

where

$$\begin{aligned} L_1^{(3)} =& \frac{1}{i\nu_1 - \epsilon(\mathbf{k}_1)} \frac{1}{i\nu_2 - \epsilon(\mathbf{k}_2)} \frac{1}{i\nu_3 - \epsilon(\mathbf{k}_3)} \frac{1}{i\nu_4 - i\nu_1 + i\nu_2 - \epsilon(\mathbf{k}_4 - \mathbf{k}_1 + \mathbf{k}_2)} \times \\ & \frac{1}{i\nu_4 - i\nu_3 + i\nu_2 - \epsilon(\mathbf{k}_4 - \mathbf{k}_3 + \mathbf{k}_2)}, \end{aligned} \tag{4.22}$$

and

$$\Sigma_2^{(3)} = \frac{U^3}{\beta^3} \sum_{\{\mathbf{k}\}} \sum_{\{\nu\}} L_2^{(3)}, \tag{4.23}$$

where

$$\begin{aligned} L_2^{(3)} =& \frac{1}{i\nu_1 - \epsilon(\mathbf{k}_1)} \frac{1}{i\nu_2 - \epsilon(\mathbf{k}_2)} \frac{1}{i\nu_3 - \epsilon(\mathbf{k}_3)} \frac{1}{i\nu_4 + i\nu_1 - i\nu_2 - \epsilon(\mathbf{k}_4 + \mathbf{k}_1 - \mathbf{k}_2)} \times \\ & \frac{1}{i\nu_4 + i\nu_3 - i\nu_2 - \epsilon(\mathbf{k}_4 - \mathbf{k}_2 + \mathbf{k}_3)}, \end{aligned} \tag{4.24}$$

One notes that in this chosen representation diagrams have the same pole-ID. Starting with $L_1^{(3)}$, our task is to find a combination of GIT transformations $\mathcal{T}$ under which $\mathcal{T} : L_1^{(3)} = \pm L_2^{(3)}$. As the first transformation, we apply $\mathcal{T}_2$ on all the internal variables of $\Sigma_1^{(3)}$, i.e.:

$$\begin{aligned}\mathcal{T}_2 :&(i\nu_1, \mathbf{k}_1) \to (-i\nu_1, -\mathbf{k}_1),\\ &(i\nu_2, \mathbf{k}_2) \to (-i\nu_2, -\mathbf{k}_2),\\ &(i\nu_3, \mathbf{k}_3) \to (-i\nu_3, -\mathbf{k}_3).\end{aligned} \tag{4.25}$$

We then have

$$\begin{aligned}\mathcal{T}_2 : L_1^{(3)} =&\frac{1}{-i\nu_1 - \epsilon(\mathbf{k}_1)}\frac{1}{-i\nu_2 - \epsilon(\mathbf{k}_2)}\frac{1}{-i\nu_3 - \epsilon(\mathbf{k}_3)}\frac{1}{i\nu_4 + i\nu_1 - i\nu_2 - \epsilon(\mathbf{k}_4 + \mathbf{k}_1 - \mathbf{k}_2)}\times\\ &\frac{1}{i\nu_4 + i\nu_3 - i\nu_2 - \epsilon(\mathbf{k}_4 + \mathbf{k}_3 - \mathbf{k}_2)}.\end{aligned} \tag{4.26}$$

Next we impose:

$$\begin{aligned}\mathcal{T}_3 :&\mathbf{k}_1 \to \mathbf{k}_1 + (\pi, \pi),\\ &\mathbf{k}_2 \to \mathbf{k}_2 + (\pi, \pi),\\ &\mathbf{k}_3 \to \mathbf{k}_3 + (\pi, \pi),\end{aligned} \tag{4.27}$$

which leads to

$$\begin{aligned}\mathcal{T}_3\mathcal{T}_2 : L_1^{(3)} =&\frac{1}{-i\nu_1 + \epsilon(\mathbf{k}_1)}\frac{1}{-i\nu_2 + \epsilon(\mathbf{k}_2)}\frac{1}{-i\nu_3 + \epsilon(\mathbf{k}_3)}\frac{1}{i\nu_4 + i\nu_1 - i\nu_2 - \epsilon(\mathbf{k}_4 + \mathbf{k}_1 - \mathbf{k}_2)}\times\\ &\frac{1}{i\nu_4 + i\nu_3 - i\nu_2 - \epsilon(\mathbf{k}_4 + \mathbf{k}_3 - \mathbf{k}_2)}.\end{aligned} \tag{4.28}$$

i.e.,

$$\mathcal{T}_3\mathcal{T}_2 : L_1^{(3)} = -L_2^{(3)}, \tag{4.29}$$

then

$$\Sigma_1^{(3)} = -\Sigma_2^{(3)}. \tag{4.30}$$

Thus, the two third order diagrams in the diagrammatic expansion of the Hubbard self-energy with nearest neighbor hopping are canceling at half-filling.

4.7.3 Truncation error

When we truncate the self-energy series expansion at a specific order m_c, we need to estimate the error due to the truncation. For a series $\sum_{n=1}^{\infty} b_n$, the absolute truncation error is given by

$$e = \sum_{n=m_c+1}^{\infty} b_n. \tag{4.31}$$

Since in practice one could only evaluate finite terms of the expansion we have to estimate the truncation error under specific circumstances. We consider two different scenarios and present estimates for the upper bound of the truncation error.

Estimation of Truncation Error for Alternating Sign Series

An alternating sign series is a series where the terms alternate between positive and negative, i.e., $\sum_{n=1}^{\infty} b_n$ is alternating sign if $b_{n+1}/b_n < 0$. An alternating sign series $\sum_{n=1}^{\infty} b_n$ is convergent if it satisfies two criteria:

1. Its nth term converges to zero:

$$\lim_{n\to\infty} b_n = 0. \tag{4.32}$$

2. The absolute values of its terms are decreasing:

$$|\frac{b_{n+1}}{b_n}| < 1. \tag{4.33}$$

Under these conditions the upper bound of the absolute truncation error is estimated by

$$e \leq |b_{m_c+1}|, \tag{4.34}$$

where m_c is the truncation order.

Estimation of Truncation Error for Non-Alternating Sign Series

We start with Eq. (4.31) to determine an upper bound for the absolute error:

$$e \leq \sum_{n=m_c+1}^{\infty} |b_n| = |b_{m_c+1}|\left(1 + \sum_{n=1}^{\infty}\left|\frac{b_{m_c+n+1}}{b_{m_c+1}}\right|\right). \tag{4.35}$$

We now assume that the series $\sum_{n=1}^{\infty} b_n$ is not alternating sign, however, the sequence $\{r_n = |b_{n+1}/b_n|\}$ is decreasing and $r_n < 1$ for $n > m_c$. We then have

$$e \leq |b_{m_c+1}|\left[1 + \sum_{n=1}^{\infty}\left|\frac{b_{m_c+2}}{b_{m_c+1}}\right|^n\right]. \tag{4.36}$$

Calculating the power series in the bracket, we finally obtain an upper limit for the error:

$$e \leq \frac{|b_{m_c+1}|}{1 - \frac{|b_{m_c+2}|}{|b_{m_c+1}|}}. \tag{4.37}$$

Bibliography

[1] Kun Chen and Kristjan Haule. A combined variational and diagrammatic quantum Monte Carlo approach to the many-electron problem. *Nat. Comm.*, 10(1):3725, 2019.

[2] E. Y. Loh, J. E. Gubernatis, R. T. Scalettar, S. R. White, D. J. Scalapino, and R. L. Sugar. Sign problem in the numerical simulation of many-electron systems. *Phys. Rev. B*, 41:9301–9307, 1990.

[3] Shailesh Chandrasekharan and Uwe-Jens Wiese. Meron-Cluster Solution of Fermion Sign Problems. *Phys. Rev. Lett.*, 83:3116–3119, 1999.

[4] Amir Taheridehkordi, S. H. Curnoe, and J. P. F. LeBlanc. Optimal grouping of arbitrary diagrammatic expansions via analytic pole structure. *Phys. Rev. B*, 101:125109, 2020.

[5] R. P. Feynman. Space-Time Approach to Quantum Electrodynamics. *Phys. Rev.*, 76:769–789, 1949.

[6] Gordon Baym and Leo P. Kadanoff. Conservation Laws and Correlation Functions. *Phys. Rev.*, 124:287–299, 1961.

[7] J. M. Luttinger and J. C. Ward. Ground-State Energy of a Many-Fermion System. II. *Phys. Rev.*, 118:1417–1427, 1960.

[8] Fabian B. Kugler. Counting Feynman diagrams via many-body relations. *Phys. Rev. E*, 98:023303, 2018.

[9] Nikolai V. Prokof'ev and Boris V. Svistunov. Polaron Problem by Diagrammatic Quantum Monte Carlo. *Phys. Rev. Lett.*, 81:2514–2517, 1998.

[10] Kris Van Houcke, Evgeny Kozik, N. Prokof'ev, and B. Svistunov. Diagrammatic Monte Carlo. *Phys. Proc.*, 6:95 – 105, 2010.

[11] K. Van Houcke, F. Werner, E. Kozik, N. Prokof'ev, B. Svistunov, M. J. H. Ku, A. T. Sommer, L. W. Cheuk, A. Schirotzek, and M. W. Zwierlein. *Nat. Phys.*, 8:366, 2012.

[12] E. Kozik, K. Van Houcke, E. Gull, L. Pollet, N. Prokof'ev, B. Svistunov, and M. Troyer. Diagrammatic Monte Carlo for correlated fermions. *Europhys. Lett.*, 90(1):10004, 2010.

[13] Riccardo Rossi. Determinant Diagrammatic Monte Carlo Algorithm in the Thermodynamic Limit. *Phys. Rev. Lett.*, 119:045701, 2017.

[14] Nikolay Prokof'ev and Boris Svistunov. Bold Diagrammatic Monte Carlo Technique: When the Sign Problem Is Welcome. *Phys. Rev. Lett.*, 99:250201, 2007.

[15] Fedor Šimkovic and Evgeny Kozik. Determinant Monte Carlo for irreducible Feynman diagrams in the strongly correlated regime. *Phys. Rev. B*, 100:121102, 2019.

[16] Alice Moutenet, Wei Wu, and Michel Ferrero. Determinant Monte Carlo algorithms for dynamical quantities in fermionic systems. *Phys. Rev. B*, 97:085117, 2018.

[17] R. Levy, J. P. F. LeBlanc, and E. Gull. Implementation of the Maximum Entropy Method for Analytic Continuation. *Comp. Phys. Comm.*, 215:149, 2017.

[18] Mark Jarrell and J.E. Gubernatis. Bayesian inference and the analytic continuation of imaginary-time quantum Monte Carlo data. *Phys. Rep.*, 269(3):133 – 195, 1996.

[19] J. Vučičević, J. Kokalj, R. Žitko, N. Wentzell, D. Tanasković, and J. Mravlje. Conductivity in the Square Lattice Hubbard Model at High Temperatures: Importance of Vertex Corrections. *Phys. Rev. Lett.*, 123:036601, 2019.

[20] Amir Taheridehkordi, S. H. Curnoe, and J. P. F. LeBlanc. Algorithmic Matsubara integration for Hubbard-like models. *Phys. Rev. B*, 99:035120, 2019.

[21] J. Hubbard. Electron Correlations in Narrow Energy Bands. *Proc. R. Soc. London, Ser. A*, 276(1365):238–257, 1963.

[22] J. P. F. LeBlanc, Andrey E. Antipov, Federico Becca, Ireneusz W. Bulik, Garnet Kin-Lic Chan, Chia-Min Chung, Youjin Deng, Michel Ferrero, Thomas M. Henderson, Carlos A. Jiménez-Hoyos, E. Kozik, Xuan-Wen Liu, Andrew J. Millis, N. V. Prokof'ev, Mingpu Qin, Gustavo E. Scuseria, Hao Shi, B. V. Svistunov, Luca F. Tocchio, I. S. Tupitsyn, Steven R. White, Shiwei Zhang, Bo-Xiao Zheng, Zhenyue Zhu, and Emanuel Gull. Solutions of the Two-Dimensional Hubbard Model: Benchmarks and Results from a Wide Range of Numerical Algorithms. *Phys. Rev. X*, 5:041041, 2015.

[23] Nikolay Prokof'ev and Boris Svistunov. Worm Algorithms for Classical Statistical Models. *Phys. Rev. Lett.*, 87:160601, 2001.

[24] Vida. Dujmović, Gwenaël. Joret, Pat. Morin, Sergey. Norin, and David R. Wood. Orthogonal Tree Decompositions of Graphs. *SIAM Journal on Discrete Mathematics*, 32(2):839–863, 2018.

[25] M. V. Sadovskii. *Diagrammatic: Lectures on Selected Problems in Condensed Matter Theory*. World Scientific, Singapore, 2006.

[26] See Supplemental Material, for details of the array representation of the diagrams, estimation of truncation error, and a list of the self-energy diagrams up to sixth order.

[27] Evgeny Kozik, Michel Ferrero, and Antoine Georges. Nonexistence of the Luttinger-Ward Functional and Misleading Convergence of Skeleton Diagrammatic Series for Hubbard-Like Models. *Phys. Rev. Lett.*, 114:156402, 2015.

[28] Fedor Šimkovic, J. P. F. LeBlanc, Aaram J. Kim, Youjin Deng, N. V. Prokof'ev, B. V. Svistunov, and Evgeny Kozik. *arXiv:1812.11503*, 2018.

[29] Zhiqiang Tan. Monte Carlo Integration With Acceptance-Rejection. *J. Comp. and Graph. Stat.*, 15, 2006.

[30] W. K. Hastings. Monte Carlo sampling methods using Markov chains and their applications. *Biometrika*, 57(1):97–109, 1970.

[31] Sergei Iskakov, Andrey E. Antipov, and Emanuel Gull. Diagrammatic Monte Carlo for dual fermions. *Phys. Rev. B*, 94:035102, 2016.

[32] Jan Gukelberger, Evgeny Kozik, and Hartmut Hafermann. Diagrammatic Monte Carlo approach for diagrammatic extensions of dynamical mean-field theory: Convergence analysis of the dual fermion technique. *Phys. Rev. B*, 96:035152, 2017.

[33] V. Zlatić, B. Horvatić, B. Dolički, S. Grabowski, P. Entel, and K.-D. Schotte. Perturbation expansion for the two-dimensional Hubbard model. *Phys. Rev. B*, 63:035104, 2000.

[34] Stéphane Daul and Michael Dzierzawa. Second order self-energy of the two-dimensional Hubbard model. *Zeitschrift für Physik B Cond. Matt.*, 103(1):41–44, 1997.

[35] Jan Gukelberger, Li Huang, and Philipp Werner. On the dangers of partial diagrammatic summations: Benchmarks for the two-dimensional Hubbard model in the weak-coupling regime. *Phys. Rev. B*, 91:235114, 2015.

[36] J. K. Freericks and Mark Jarrell. Iterated perturbation theory for the attractive Holstein and Hubbard models. *Phys. Rev. B*, 50:6939–6953, 1994.

[37] J. K. Freericks. Conserving approximations for the attractive Holstein and Hubbard models. *Phys. Rev. B*, 50:403–417, 1994.

[38] F. Gebhard, E. Jeckelmann, S. Mahlert, S. Nishimoto, and R. M. Noack. Fourth-order perturbation theory for the half-filled Hubbard model in infinite dimensions. *Euro. Phys. J. B*, 36(4):491–509, 2003.

[39] Naoto Tsuji and Philipp Werner. Nonequilibrium dynamical mean-field theory based on weak-coupling perturbation expansions: Application to dynamical symmetry breaking in the Hubbard model. *Phys. Rev. B*, 88:165115, 2013.

[40] J. P. F. LeBlanc and Emanuel Gull. Equation of state of the fermionic two-dimensional Hubbard model. *Phys. Rev. B*, 88:155108, 2013.

[41] Thomas Maier, Mark Jarrell, Thomas Pruschke, and Matthias H. Hettler. Quantum cluster theories. *Rev. Mod. Phys.*, 77:1027–1080, 2005.

[42] R. Rossi, T. Ohgoe, K. Van Houcke, and F. Werner. Resummation of Diagrammatic Series with Zero Convergence Radius for Strongly Correlated Fermions. *Phys. Rev. Lett.*, 121:130405, 2018.

[43] Wei Wu, Michel Ferrero, Antoine Georges, and Evgeny Kozik. Controlling Feynman diagrammatic expansions: Physical nature of the pseudogap in the two-dimensional Hubbard model. *Phys. Rev. B*, 96:041105, 2017.

[44] Riccardo Rossi, Félix Werner, Nikolay Prokof'ev, and Boris Svistunov. Shifted-action expansion and applicability of dressed diagrammatic schemes. *Phys. Rev. B*, 93:161102, 2016.

[45] J. Vučičević and M. Ferrero. Real-frequency diagrammatic Monte Carlo at finite temperature. *Phys. Rev. B*, 101:075113, 2020.

[46] Shogo Shinkai, Hiroaki Ikeda, and Kosaku Yamada. Fourth Order Perturbation Theory for Normal Selfenergy in Repulsive Hubbard Model. *J. Phys. Soc. Jpn.*, 74(9):2592–2597, 2005.

[47] Jan Gukelberger, Evgeny Kozik, and Hartmut Hafermann. Diagrammatic Monte Carlo approach for diagrammatic extensions of dynamical mean-field theory: Convergence analysis of the dual fermion technique. *Phys. Rev. B*, 96:035152, 2017.

[48] Alexander Gaenko, Emanuel Gull, Andrey E. Antipov, Lukas Gamper, Gabriele Carcassi, Joe Paki, Ryan Levy, Michele Dolfi, Jonas Greitemann, and James P.F. LeBlanc. ALPSCore: Version 0.5.4, 2016.

[49] Markus Wallerberger, Sergei Iskakov, Alexander Gaenko, Joseph Kleinhenz, Igor Krivenko, Ryan Levy, Jia Li, Hiroshi Shinaoka, Synge Todo, Tianran Chen,

Xi Chen, James P. F. LeBlanc, Joseph E. Paki, Hanna Terletska, Matthias Troyer, and Emanuel Gull. *arXiv:1811.08331*, 2018.

Chapter 5

Algorithmic approach to diagrammatic expansions for real-frequency evaluation of susceptibility functions

In Chapter 4 we used AMI combined with graph invariant transformations (GIT) and Monte Carlo integration routines to evaluate the truncated series expansion of the self-energy function in both the Matsubara and real frequency spaces. However, it is straightforward to use our method to evaluate a wide range of diagrammatic expansions. In this chapter we use our method to evaluate the spin susceptibility functions.

Theoretical calculations of the spin susceptibilities on the real-frequency axis have been limited to coarse approximations such as the T-matrix approximation (TMA) [1, 2], random phase approximations (RPA) [3, 4] and low order vertex corrections [5] for decades. This is because in the absence of a method to systematically generate

and evaluate higher order terms, these approximations have been the only choices available to investigate the susceptibility functions in real-frequency space. We apply our methodology to this challenging problem in order to study, for the first time, the higher order perturbative corrections beyond the approximations mentioned above. We prove the correctness of our results on Matsubara axis by comparing to other numerical methods. Lastly, due to the analyticity of AMI, we provide the results on real-frequency axis.

In the rest of this chapter we reproduce Ref. [6], Amir Taheridehkordi, Stephanie H. Curnoe, and James P. F. LeBlanc, doi: 10.1103/PhysRevB.102.045115; License number: RNP/20/OCT/031578; reproduced with kind permission of the publishers of Physical Review B. The manuscript is followed by Supplemental Material.

5.1 Abstract

We systematically generate the perturbative expansion for the two-particle spin susceptibility in the Feynman diagrammatic formalism and apply this expansion to a model system - the single-band Hubbard model on a square lattice. We make use of algorithmic Matsubara integration (AMI) [A. Taheridehkordi, S. H. Curnoe, and J. P. F. LeBlanc, Phys. Rev. **B** 99, 035120 (2019)] to analytically evaluate Matsubara frequency summations, allowing us to symbolically impose analytic continuation to the real frequency axis. We minimize our computational expense by applying graph invariant transformations [A. Taheridehkordi, S. H. Curnoe, and J. P. F. LeBlanc, Phys. Rev. **B** 101, 125109 (2020)]. We highlight extensions of the random-phase approximation and T-matrix methods that, due to AMI, become tractable. We present results for weak interaction strength where the direct perturbative expansion is convergent, and verify our results on the Matsubara axis by comparison to other numerical

methods. By examining the spin susceptibility as a function of real-frequency via an order-by-order expansion we can identify precisely what role higher order corrections play on spin susceptibility and demonstrate the utility and limitations of our approach.

5.2 Introduction

The Hubbard model [7] has become a laboratory for the development of numerical tools in correlated electron systems. The single-band model on a two-dimensional (2D) square lattice is believed to be the minimal model to capture features of high-temperature superconductivity [8] yet remains a complex numerical problem that has motivated the development of numerous novel numerical algorithms [9, 10].

The single-particle properties of that model have been investigated by a wide variety of different methods, from non-perturbative approaches such as dynamical Mean-field theory [11,12] and dynamical cluster approximation [13,14] to perturbative methods such as diagrammatic Monte Carlo [15–22]. Understanding the role of two-particle excitations - for experiments on cuprates [23–27] as well as for numerical calculations of model systems [28–36] - is of particular importance due to the subtle connections between spin excitations, antiferromagnetic order, superconductivity and pseudogap phenomena. Despite the wide range of existing numerical algorithms the ability for numerical work to make concrete connections to experiment has been largely hampered by the challenges associated with evaluating the necessary two-particle spin and charge response functions.

There exists a greater issue that, in addition to the complexity of two particle response functions, many numerical methods are constructed around the finite-temperature Matsubara formalism and provide results in an abstract imaginary time/-

Matsubara frequency space. While results for physically relevant properties on the so-called 'real-time/real-frequency' axis can be obtained but require numerical analytic continuation procedures for which solutions are not unique [37–41]. As a result, the numerical analytic continuation process dominates the uncertainty of the result and compromises any attempt at high-precision numerics [42–44]. In principle, this issue can be avoided through a textbook application of the residue theorem, resulting in analytical expressions for which analytic continuation can be imposed symbolically. For low order diagrams this can be done by hand but for higher order corrections the resulting expressions become incomprehensibly complicated. For that reason this known solution is discarded for all but the most weakly correlated electron systems. We have recently overcome this particular road-block with the method of algorithmic Matsubara integration (AMI) [45], a procedure that automates the construction of such analytic results and in principle allows for a direct evaluation of arbitrary diagrammatic expansions composed of thousands of analytic terms on the real-frequency axis. In addition, there still remains a general sign problem [46, 47] as well as a more fundamental fermionic sign due to cancellation between diagrams in the expansion. In order to suppress the second issue, one opportunity lies in the construction of *sign-blessed* diagram groups by application of graph invariant transformations (GIT) that can effectively be combined with AMI [48].

In anticipation of these developments, we present the spin susceptibility of the 2D Hubbard model, *beyond* random phase approximation (RPA) [3, 4], T-matrix approximation (TMA) [1, 2] and low-order vertex corrections [5], in the real-frequency domain without need for any ill-posed numerical analytic continuation procedures.

5.3 Hubbard model

We consider the single-band Hubbard Hamiltonian [9, 49],

$$H = \sum_{\langle ij\rangle\sigma} t_{ij} c^\dagger_{i\sigma} c_{j\sigma} + U \sum_i n_{i\uparrow} n_{i\downarrow} - \mu \sum_{i\sigma} n_{i\sigma}, \tag{5.1}$$

where t_{ij} is the hopping amplitude, $c^{(\dagger)}_{i\sigma}$ is the annihilation (creation) operator at site i, $\sigma \in \{\uparrow, \downarrow\}$ is the spin, U is the onsite Hubbard interaction, $n_{i\sigma} = c^\dagger_{i\sigma} c_{i\sigma}$ is the number operator, μ is the chemical potential, and $\langle ij\rangle$ restricts the sum to nearest neighbors. For a 2D square lattice we take $t_{ij} = -t$, resulting in the free particle energy

$$\epsilon(\mathbf{k}) = -2t[\cos(k_x) + \cos(k_y)] - \mu. \tag{5.2}$$

5.4 Transverse spin susceptibility:

The expansion for the transverse spin susceptibility is straightforwardly represented in position ($\mathbf{r}$) and imaginary time (τ) space and is defined as [30]

$$\chi_T(x, x') = \langle \mathcal{T} S_+(x) S_-(x')\rangle, \tag{5.3}$$

where $\mathcal{T}$ is the time-ordering operator, $x = (\mathbf{r}, \tau)$, and $S_{+/-}$ are spin-ladder operators which are given by $S_+(x) = S^\dagger_-(x) = c^\dagger_\uparrow(x) c_\downarrow(x)$. One could instead construct the diagrammatic series for the longitudinal spin susceptibility $\chi_L(x, x') = \langle \mathcal{T} S_z(x) S_z(x')\rangle$ [36], however, the spin-rotation invariance of the Hubbard Hamiltonian [50, 51] implies that $\chi_T = 2\chi_L$; we note that the diagrammatic series for the transverse spin susceptibility is substantially simpler.

5.4.1 Constructing diagrammatic expansion

We use perturbation theory to evaluate the transverse spin susceptibility defined by Eq. (5.3). We construct the perturbative expansion and using Wick's theorem we represent the result as a series of Feynman diagrams [52–54] that can then be evaluated in the momentum-frequency space. Each transverse susceptibility diagram in the series has the property that the particle lines in the *principle loop* (a unique fermionic loop that involves the two external vertices) have spin $\uparrow$, while anti-particle lines have spin $\downarrow$. Furthermore, since the on-site Hubbard interaction only occurs between solid lines with different spins we only consider diagrams that satisfy this criterion.

First, we systematically generate all the *topologically distinct* transverse susceptibility diagrams up to a truncation order m_c by following the procedure described in Ref. [48]. In order to reduce the diagrammatic space we neglect all diagrams with tadpole insertions by applying the chemical potential shift $\mu \to \mu - \bar{n}U/2$, where $\bar{n}$ is the number of electrons per site [55, 56]. Following the method outlined in Refs. [45, 48], we assign frequency (X^j) and momenta ($\mathbf{K}_j$) variables to each fermionic line, where X^j and $\mathbf{K}_j$ are linear combinations of the independent frequencies and momenta. Applying the Feynman rules, a diagram D_{ζ_m} of order m with topology ζ_m is evaluated as:

$$D_{\zeta_m}(i\Omega, \mathbf{q}, \beta, \mu) = \frac{(-1)^{m+F_{\zeta_m}} U^m}{(2\pi)^{2m+2}\beta^{m+1}} \times \sum_{\{\mathbf{k}_{m+1}\}} \sum_{\{\nu_{m+1}\}} \prod_{j=1}^{2m+2} \mathcal{G}_0^j(\epsilon^j, X^j). \tag{5.4}$$

Here, $i\Omega$ and $\mathbf{q}$ are external frequency and momenta respectively, F_{ζ_m} is the number of fermionic loops, β is the inverse temperature, $\{\mathbf{k}_{m+1}\}$ and $\{\nu_{m+1}\}$ are sets of (independent) internal momenta and frequencies, respectively, $\epsilon^j = \epsilon(\mathbf{K}_j)$ represents the free particle energy of the jth line and $\mathcal{G}_0^j(\epsilon^j, X^j) = (X^j - \epsilon^j)^{-1}$ is the bare Green's

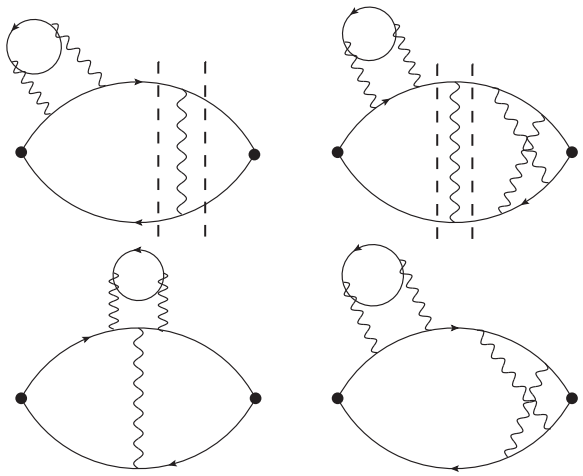

Figure 5.1: *Top row*: Examples of ladder-like diagrams which must be excluded from the ETM series. *Bottom row*: Examples of non-ladder-like diagrams which must be included in the ETM series. The dashed lines identify where the ladder-like diagrams split into independent parts (there are no common independent frequency-momenta variables to the left and right). Solid and wavy lines are fermionic and interaction lines, respectively.

function assigned to the jth solid line.

We first symbolically evaluate the Matsubara sums in Eq. (5.4) by utilizing the residue theorem. Although conceptually straightforward, the complexity of the resulting analytic expressions requires an automated machinery. For this we follow the AMI procedure, described in Refs. [45,48], to automatically construct and store the analytic expressions for the Matsubara sums. Finally, we use an integration procedure [48,57] to evaluate the momenta sums of the diagrams.

The perturbative series of the transverse spin susceptibility is then written as

$$\chi_T^{(m_c)}(i\Omega, \mathbf{q}, \beta, \mu) = \sum_{m=0}^{m_c} \sum_{\zeta_m} D_{\zeta_m}(i\Omega, \mathbf{q}, \beta, \mu), \tag{5.5}$$

where the sum over ζ_m is over all unique topologies of order m, here summed to a cutoff order m_c. The direct evaluation of Eq. (5.5) is a challenging task due to the factorial increase of the number of diagrams with order [58] as well as a factorial increase

in the number of terms after applying AMI. Therefore, to reduce the diagrammatic space we propose an alternative procedure, which we call *extended T-matrix* (ETM), to approximate the transverse spin susceptibility by only evaluating a subset of susceptibility diagrams. We categorize diagrams into two types: *ladder-like* diagrams, those that can be factored into two (or more) independent integrals, and *non-ladder-like* diagrams, which cannot be factored. Examples of such diagrams are shown in Fig. 5.1. We define $\chi_{NL}^{(m_c)}$ to be the sum of all the non-ladder-like diagrams up to a truncation order m_c; then the transverse spin susceptibility is approximated by

$$\chi_{ETM}^{(m_c)}(i\Omega, \mathbf{q}, \beta, \mu) = \frac{\chi_{NL}^{(m_c)}(i\Omega, \mathbf{q}, \beta, \mu)}{1 - U\chi_{NL}^{(m_c)}(i\Omega, \mathbf{q}, \beta, \mu)}. \tag{5.6}$$

In a general sense, $\chi_{NL}^{(m_c)}$ and U play the same roles in the transverse spin susceptibility expansion as the *bare* Green's function and self-energy do in the diagrammatic expansion of the full Green's function [59,60]. Eq. (5.6) reduces to the RPA for longitudinal spin susceptibility and to the TMA for transverse spin susceptibility at $m_c = 0$ ($\chi_{NL}^{(0)}$ is the bare bubble), while in the $m_c \to \infty$ limit it recovers the direct expansion of Eq. (5.5). This provides a systematic bridge between those coarse approximations and the exact result and we expect that Eq. (5.6) with $m_c \geq 1$ will provide more reliable results when compared to the RPA and TMA approaches.

By taking advantage of the inherent symmetry of the half-filled Hubbard model on a square lattice the diagrammatic space can be further reduced. We apply the GIT procedure [48] to identify *exactly* canceling and *exactly* equal diagrams at half-filling. The complete diagrammatic space reduction is shown in Table 5.1. In order to calculate the transverse spin susceptibility up to third order via Eq. (5.4), we need to evaluate only 11 diagrams in total. For the ETM approach this number is further reduced to only six diagrams at third order, and by 4th order the number of non-

Table 5.1: Diagrammatic space reduction of the transverse spin susceptibility up to fourth order at half-filling. In the second row, $n^{(m)}$ is the number of diagrams at each order m (not including diagrams with tadpole insertions), and $(n_{NL}^{(m)})$ is the number of non-ladder-like diagrams at each order m. In the last row, $n_g^{(m)}$ is the number of groups of equal diagrams at each order m, and $(n_{g,NL}^{(m)})$ is the number of groups of equal non-ladder-like diagrams at each order m.

m	0	1	2	3	4
$n^{(m)}(n_{NL}^{(m)})$	1(1)	1(0)	4(3)	17(10)	101(22)
$n_g^{(m)}(n_{g,NL}^{(m)})$	1(1)	1(0)	3(2)	6(3)	71(16)

ladder-like diagrams drops drastically with $\approx 80\%$ of the diagrams being ladder-like.

5.5 Numerical results and comparisons

We first consider the order-by-order evaluation of χ_T on the Matsubara axis at $\mathbf{q} = (\pi, \pi)$. Results for truncation order $m_c = 0$ to 4 are shown in Fig. 5.2. We consider a weak coupling parameter regime which has been of interest for algorithm development due to the long correlation length of the model, a fact that necessitates very careful finite size scaling for many numerical methods [9, 10]. For comparison we include high-quality results from functional-Renormalization Group (fRG) from Ref. [36] and our results from the dual-fermion (DF) technique [35, 61, 62], as well as the evaluation of the TMA. The parameter regime of $U/t = 2$ at $\beta t = 5$ has been chosen precisely because it is the cusp where $U\chi_T^{(0)} \approx 1$ and the TMA breaks down resulting in a diverging negative value at $i\Omega = 0$ while the result at all other frequencies is overestimated by the TMA. In contrast, the order by order expansion is exactly equivalent to the reference data at $i\Omega \neq 0$ and shows a systematic tendency at $i\Omega = 0$ towards the reference fRG and DF data sets. By truncation order $m_c = 4$ the discrepancy of $\chi_T^{(4)}$ compared to the fRG and DF results is $\approx 2\%$ and 5% respec-

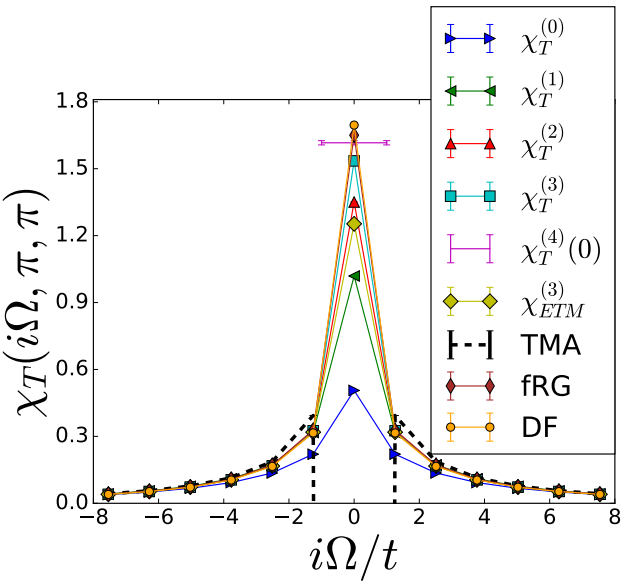

Figure 5.2: Transverse spin susceptibility $\chi_T^{(m_c)}$ for $m_c = 0, 1, 2$ and 3 and $\chi_{ETM}^{(3)}$ vs. Matsubara frequency $i\Omega$ at $U/t = 2$, $\beta t = 5$ and $\mu/t = 0$ for $\mathbf{q} = (\pi, \pi)$. We also present $\chi_T^{(4)}(i\Omega = 0)$, TMA, DF [61], and fRG results from Ref. [36]. Each data point is obtained with $\approx 10^7$ Monte Carlo samples.

tively. Also shown are results for $\chi_{ETM}^{(3)}$ which is in precise agreement with the fRG and DF results for $i\Omega \neq 0$. At $i\Omega = 0$ the third-order ETM result does not suffer the divergence of the TMA although it underestimates the value even in comparison to the direct second order expansion.

Having now verified the precise convergence at a nominal temperature of $\beta t = 5$ we display the order-by-order temperature dependence of the direct expansion, $\chi_T^{(m_c)}$ at $\mathbf{q} = (\pi, \pi)$ for the zeroth bosonic frequency at weak coupling. Results are shown in Fig. 5.3 for $U/t = 1$ and 2. We include results of the DF method, which for this parameter range is essentially exact [63], as well as comparison to the TMA. One immediately notes the deviation of the TMA result from the DF benchmark even at $U/t = 1$ for temperatures above $\beta t = 2$, which translates into a severe divergence for $U/t = 2$ above $\beta t = 1$. In contrast, the order-by-order expansion remains stable, showing a systematic improvement, and we see that higher orders become more im-

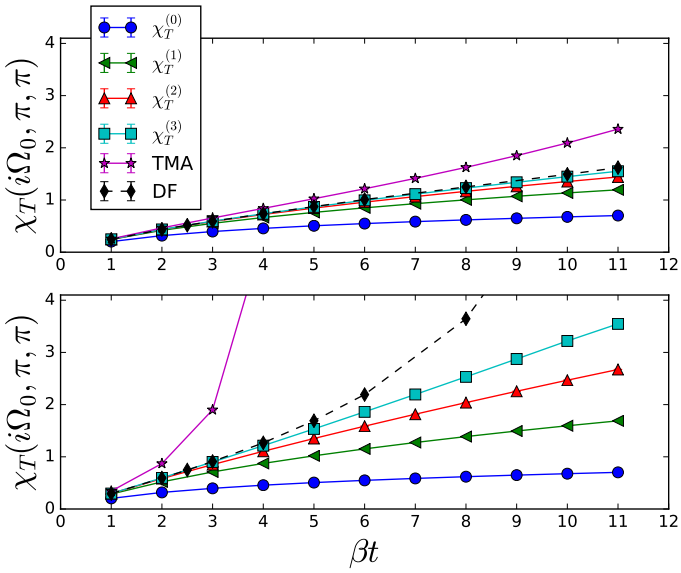

Figure 5.3: Transverse spin susceptibility vs. inverse temperature at different truncation orders $m_c = 0, 1, 2$ and 3. The TMA and DF results are also shown for comparison. Data are for *Top*: $U/t = 1$, *Bottom*: $U/t = 2$ with $\mu/t = 0$ at $\mathbf{q} = (\pi, \pi)$ and $i\Omega = i\Omega_0 = 0$. Each data point is obtained with $\approx 10^7$ Monte Carlo samples.

portant at lower temperatures and larger U/t values. The data point $\mathbf{q} = (\pi, \pi)$ and $i\Omega = i\Omega_0$ is the point where the convergence of the transverse susceptibility series is slowest. However, for non-zero Matsubara frequencies the convergence of the series is extremely fast, often by second or third order (see the Supplemental Materials [64] for a non-zero frequency comparison).

We now turn to one of our main results, the order-by-order contribution of diagrams $[O(m)]$ with $m = 0, 1, 2$, and 3 to the imaginary part of the transverse spin susceptibility as a function of real frequency (see Supplemental Materials [64] for $\mathrm{Re}[\chi_T]$ results). The top frame of Fig. 5.9 shows the contribution to $\chi_T^{(3)}$ at each separate order. As the order increases we find that higher order terms contribute significant corrections only for a range of frequencies near $\Omega = 0$ which adjust the slope of the $\omega \to 0$ limit of χ_T. Otherwise the contributions are largely unstructured until one reaches the band edge near $\omega/t = 4$. The reduced contribution at higher frequency is

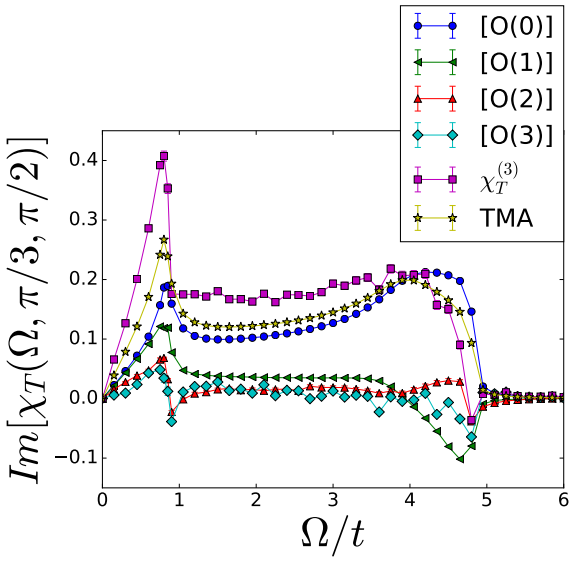

Figure 5.4: *Top*: Imaginary part of the mth order transverse spin susceptibility diagrams $[O(m)]$ vs. real frequency Ω. *Bottom*: The third order transverse spin susceptibility $\chi_T^{(3)}$; TMA, $\chi_{ETM}^{(2)}$ as well as $\chi_{NL}^{(2)}$, are also shown. Data are for $\beta t = 5$, $U/t = 2$ with $\mu/t = 0$ at $\mathbf{q} = (\pi/3, \pi/2)$. We set $\Gamma/t = 0.02$ in the symbolic analytic continuation $i\Omega \to \Omega + i\Gamma$. Each data point is obtained with $\approx 10^8$ Monte Carlo samples.

expected and is similar to that seen on the Matsubara axis. We also produce $\chi_{ETM}^{(2)}$ for real-frequencies using $\chi_{NL}^{(2)}$ and compare this in the lower frame of Fig. 5.4 to the TMA and the direct expansion up to third order $\chi_T^{(3)}$. We see that, for this value of U/t, the TMA underestimates both the peak amplitude and low frequency slope (and performs worse for larger values of U/t - see Supplemental Materials [64]). In contrast $\chi_{ETM}^{(2)}$ is nearly identical to the third order direct expansion - it captures the same slope at low frequency, peak location, and high frequency amplitude. This comparison is rather impressive given that the third order direct expansion includes 23 diagrams while the ETM at second order includes only 4. One notes that at $\Omega/t = 4.8$ there is a single data point where $\mathrm{Im}[\chi_T^{(3)}]$ dips negative. Since $\mathrm{Im}[\chi_T]$ can not change sign higher order corrections in the direct diagrammatic expansion are necessary to achieve physically reliable results at this specific point.

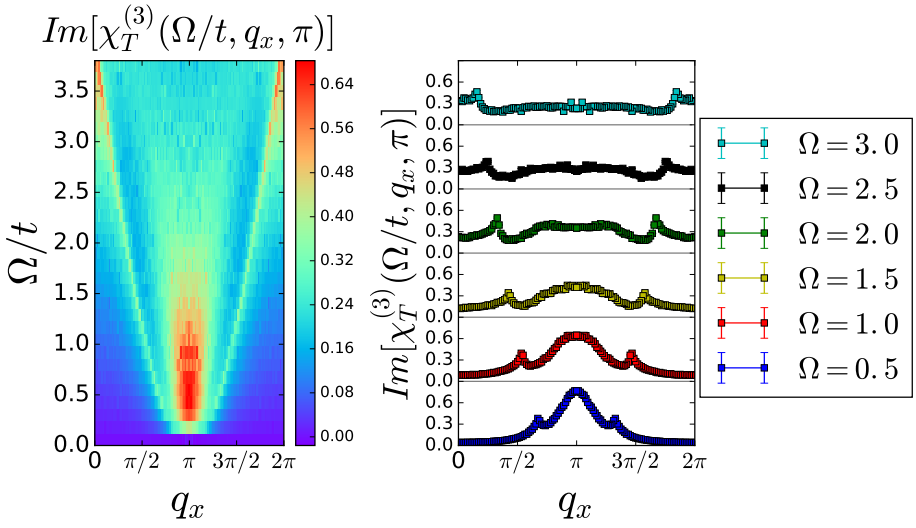

Figure 5.5: *Left*: third order transverse susceptibility $\chi_T^{(3)}$ as a function of real frequency Ω along the momentum cut $(0, \pi) \to (2\pi, \pi)$. *Right*: Frequency cuts along $\Omega = 0.5$ to 3. Data are for $\beta t = 5$, $U/t = 2$, and $\mu/t = 0$. We set $\Gamma/t = 0.02$ in the symbolic analytic continuation $i\Omega \to \Omega + i\Gamma$. Each data point is obtained with $\approx 10^6$ Monte Carlo samples.

Finally, we show on the left in Fig. 5.5 the dependence of the third order spin susceptibility on both $\mathbf{q}$ and real frequency, Ω, along $\mathbf{q} = (0, \pi)$ to $\mathbf{q} = (2\pi, \pi)$ in the first Brillouin zone. On the right we plot the corresponding susceptibility along several fixed-frequency cuts ranging from $\Omega/t = 0.5$ to 3. One notes two important features: a set of two dispersive peaks and a broad peak near $\mathbf{q} = (\pi, \pi)$ that widens and flattens as frequency is increased. This behavior is reminiscent of inelastic neutron scattering results on undoped LSCO [65, 66] where low energy cuts exhibit a single peak near $\mathbf{q} = (\pi, \pi)$ that splits at higher energies into a set of two dispersive peaks. Those materials have been understood, however, with linear-spin-wave models that estimate values of $U/t \approx 8$, well beyond the convergence of our series at low orders [24]. Precisely how spin excitations evolve from weak to strong coupling in Hubbard models has yet to be understood. Our method might be extended to larger values of U/t via renormalization procedures, but such work has yet to be accomplished.

5.6 Conclusion

We have computed a direct perturbative diagrammatic expansion of the spin susceptibility *evaluated on the real frequency axis* facilitated by AMI. We point out that there is no conceptual hurdle in generating and evaluating higher order diagrams. In addition, the method can be used for the case of finite next-nearest neighbors hopping and finite doping. AMI automates this process and provides an *analytic* result in frequency space that can be expressed on the real frequency axis by simple substitution without resorting to numerical analytic continuation methods. The standard methods of numerical analytic continuation (such as MAXENT or Padé-approximants), while known to be ill-posed, have been central in the theoretical analysis of both single and two-particle properties of materials. With the advent of AMI, this no longer need be the case for any problem where direct perturbative expansions are convergent.

This methodology has the advantage that it is conceptually very simple and appears to be systematically controllable. The analytic expressions generated by AMI to solve the 2D square lattice with Hubbard interaction remain valid in any dimensionality for any single-band dispersion. Moreover, the AMI procedure is not limited to Hubbard interactions and can be applied to any frequency independent interaction [45, 48]. The procedures outlined in this work can therefore be applied to the diagrammatic expansion of the polarization function relevant to screening problems such as the GW approximation. Moreover, while we applied AMI to the diagrammatic expansions of the spin susceptibilities it can be used to evaluate charge and particle-particle susceptibility functions. We anticipate that the application of AMI to other interactions on lattice systems will open many avenues of advancement in condensed matter physics.

5.7 Acknowledgments

The authors would like to thank F. Šimkovic, S. Andergassen, C. Hille and T. Schäfer for reference data and useful discussion. JPFL and SHC acknowledge the support of the Natural Sciences and Engineering Research Council of Canada (NSERC) (RGPIN-2017-04253, and RGPIN-2014-057). Computational resources were provided by ACENET and Compute Canada. Our Monte Carlo codes make use of the open source ALPSCore framework [39–41] and we have used the open source code Maxent [38] for numerical analytic continuation.

5.8 Supplemental material

5.8.1 Results on the Matsubara frequency axis

A higher temperature example

In Fig. 5.6 we plot the transverse spin susceptibility versus Matsubara frequency at a relatively high temperature $\beta t = 2.5$ and a weak coupling $U/t = 2$ (Fig. 2 in the main text uses $\beta t = 5$). The direct third order approximation is in solid agreement with the results from self-consistent ladder dual-fermion (DF) calculations.

Temperature dependence for a non-zero Matsubara frequency

As illustrated in Fig. 3 in the main text, upon decreasing temperature, a higher order truncated series should be considered to obtain numerically reliable results. However, one should note that convergence away from zero frequency is quite fast and the third order approximation is typically sufficient. To demonstrate this we present the transverse susceptibility at the first Matsubara frequency against inverse temperature order at $U/t = 1$ and $U/t = 2$ for $m_c = 0$ to 3. We find that, at these interaction

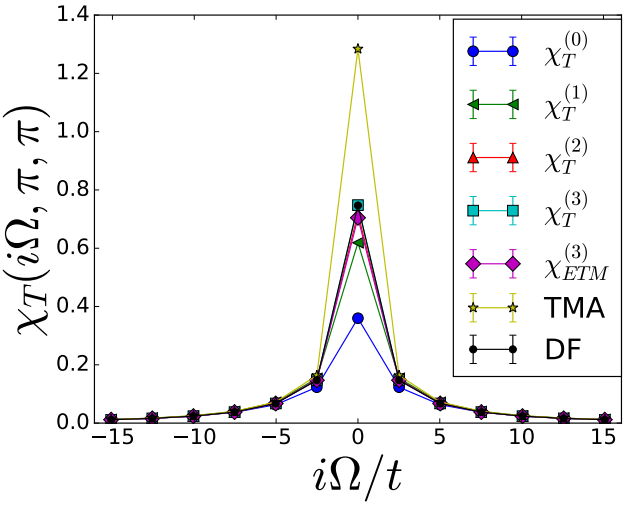

Figure 5.6: Transverse spin susceptibility vs. Matsubara frequency $i\Omega$ at different truncation orders $m_c = 0$ to 3. Data are for $U/t = 2$, $\beta t = 2.5$ with $\mu/t = 0$ at $\mathbf{q} = (\pi, \pi)$. We show the third order ETM, TMA and DF results for comparison.

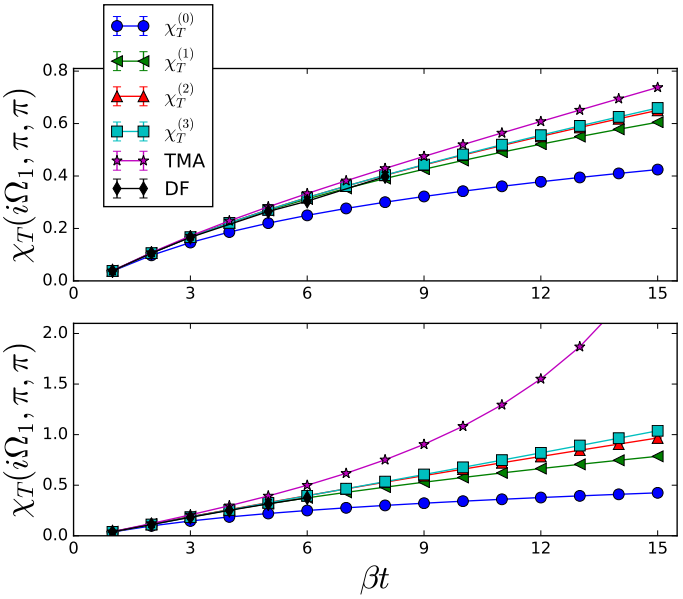

Figure 5.7: Transverse spin susceptibility vs. inverse temperature at different truncation orders $m_c = 0$ to 3. The TMA and DF results are also shown for comparison. Data are for *Top*: $U/t = 1$, *Bottom*: $U/t = 2$ with $\mu/t = 0$ at $\mathbf{q} = (\pi, \pi)$ and $i\Omega = i\Omega_1 = 2\pi/\beta$.

strengths, even at the extremely low temperature $\beta t = 11$ the second and third order approximation are almost identical, i.e., the third order approximation is sufficient to

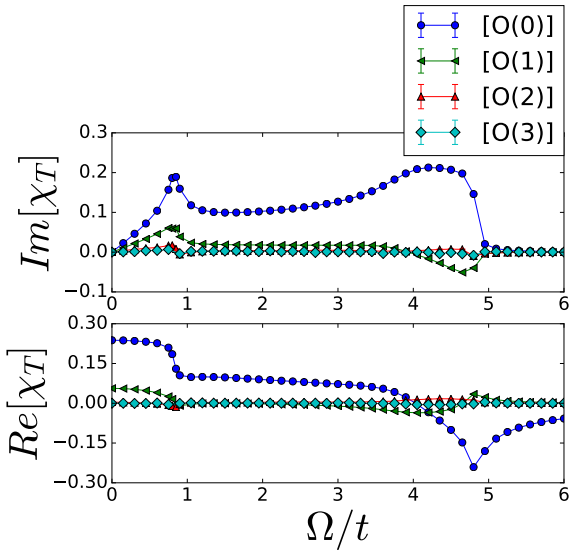

Figure 5.8: *Top*: imaginary and *Bottom*: real part of the mth order transverse spin susceptibility diagrams $[O(m)]$ vs. real frequency Ω. Data are for $\beta t = 5$, $U/t = 1$, and $\mu/t = 0$ at $\mathbf{q} = (\pi/3, \pi/2)$. We set $\Gamma/t = 0.02$ in the symbolic analytic continuation $i\Omega \to \Omega + i\Gamma$.

approximate the susceptibility function. Moreover, in both cases the agreement with DF is solid.

5.8.2 Results on the real frequency axis

Order-by-order contribution

In Fig. 5.8 we show the order-by-order contribution of diagrams $[O(m)]$ with $m = 0$ to 3 to the transverse spin susceptibility versus real frequency for $\beta t = 5$, $U/t = 1$, and $\mu/t = 0$ at $\mathbf{q} = (\pi/3, \pi/2)$. We find that high order terms mostly contribute for a range of frequencies near $\Omega = 0$ and also near the band edge above $\omega = 4$. Furthermore, as one expects the higher order contributions decay very fast increasing order (Fig. 4 of the main text shows the imaginary part only, for a larger value of $U/t = 2$).

We also show in Fig. 5.9 the order-by-order contribution to real part of the sus-

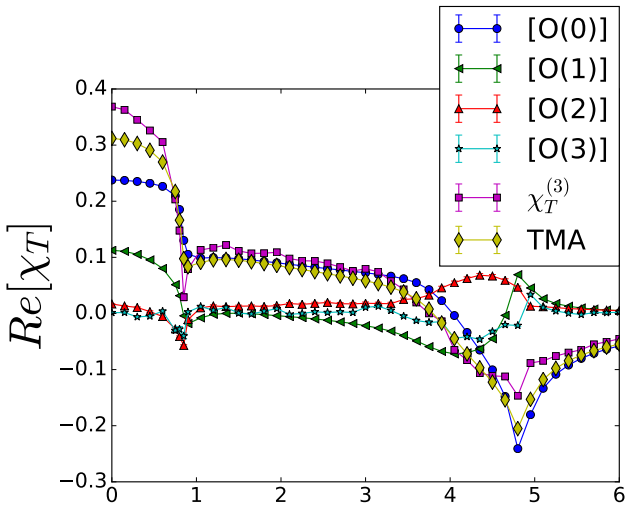

Figure 5.9: Real part of the mth order transverse spin susceptibility diagrams vs. real frequency Ω. The TMA and third order transverse spin susceptibility $\chi_T^{(3)}$ are also shown. Data are for $\beta t = 5$, $U/t = 2$, and $\mu/t = 0$ at $\mathbf{q} = (\pi/3, \pi/2)$. We set $\Gamma/t = 0.02$ in the symbolic analytic continuation $i\Omega \to \Omega + i\Gamma$.

ceptibility function at $U/t = 2$ with the same parameters as the main text Fig. 4. One immediately notes that in this parameter regime, the contribution of the second and third order diagrams is negligible for $1.5 < \Omega < 3$ and $\Omega > 5$.

Comparison with TMA

In Fig. 5.10 we compare the second order transverse spin susceptibility, $\chi_T^{(2)}$ with TMA on the real frequency axis for different choices of $U/t = 1 \to 3$. We note that by increasing U/t the peak in $\mathrm{Im}[\chi_{TMA}]$ moves to lower Ω and the peak becomes rounded, a behavior not observed in $\chi_T^{(2)}$ where the peak is independent of the choice of U/t and remains sharp. Moreover, TMA results show a much steeper slope in vicinity of $\Omega = 0$ compared to the second order approximation.

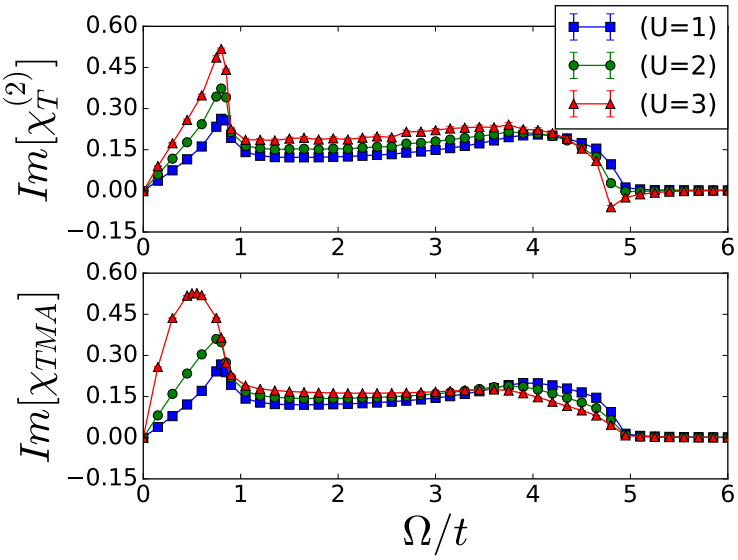

Figure 5.10: Imaginary part of the second order and TMA transverse spin susceptibility vs. real frequency Ω for $U = 1 \to 3$. Data are for $\beta t = 5$ and $\mu/t = 0$ at $\mathbf{q} = (\pi/3, \pi/2)$. We set $\Gamma/t = 0.02$ in the symbolic analytic continuation $i\Omega \to \Omega + i\Gamma$.

Analytic continuation: dependence on the regulator

We investigate the dependence of the first order transverse susceptibility function on the regulator Γ in Fig. 5.11 for $\beta t = 5$, $U/t = 2$, and $\mu/t = 0$ at $\mathbf{q} = (\pi/3, \pi/2)$ and $\Omega/t = 2$. We observe that the result has only weak dependence on $\Gamma/t \leq 0.04$. Therefore, our choice of regulator in this work $\Gamma/t = 0.02$ is effectively in the limit of $\Gamma \to 0$.

Bibliography

[1] Hidetoshi Fukuyama and Yasumasa Hasegawa. t-Matrix Approximation to Two-Dimensional Hubbard Model. *Prog. of Theo. Phys. Suppl.*, 101:441–452, 1990.

[2] Jan Gukelberger, Li Huang, and Philipp Werner. On the dangers of partial diagrammatic summations: Benchmarks for the two-dimensional Hubbard model

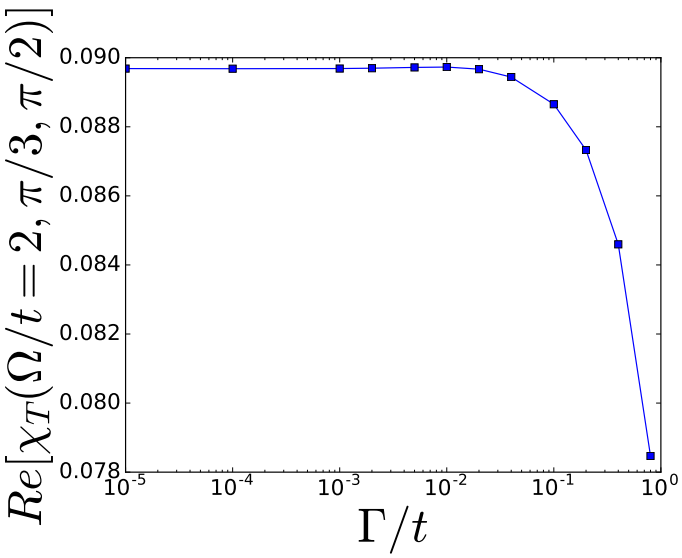

Figure 5.11: Real part of the first order transverse spin susceptibility vs. regulator Γ in analytic continuation process $i\Omega \to \Omega + i\Gamma$. Data are for $\beta t = 5$, $U/t = 2$, and $\mu/t = 0$ at $\mathbf{q} = (\pi/3, \pi/2)$ and $\Omega/t = 2$.

in the weak-coupling regime. *Phys. Rev. B*, 91:235114, 2015.

[3] David Bohm and David Pines. A Collective Description of Electron Interactions. I. Magnetic Interactions. *Phys. Rev.*, 82:625–634, 1951.

[4] David Bohm and David Pines. A Collective Description of Electron Interactions: III. Coulomb Interactions in a Degenerate Electron Gas. *Phys. Rev.*, 92:609–625, 1953.

[5] Kazuyoshi Yoshimi, Takeo Kato, and Hideaki Maebashi. Enhanced Spin Susceptibility toward the Charge-Ordering Transition in a Two-Dimensional Extended Hubbard Model. *J. Phys. Soc. Jpn.*, 78(10):104002, 2009.

[6] Amir Taheridehkordi, S. H. Curnoe, and J. P. F. LeBlanc. Algorithmic approach to diagrammatic expansions for real-frequency evaluation of susceptibility functions. *Phys. Rev. B*, 102:045115, 2020.

[7] J. Hubbard. Electron Correlations in Narrow Energy Bands. *Proc. R. Soc. London, Ser. A*, 276(1365):238–257, 1963.

[8] F. Mancini, S. Marra, and H. Matsumoto. Spin magnetic susceptibility in the two-dimensional Hubbard model. *Phys. C: Superconduc.*, 252(3):361–374, 1995.

[9] J. P. F. LeBlanc, Andrey E. Antipov, Federico Becca, Ireneusz W. Bulik, Garnet Kin-Lic Chan, Chia-Min Chung, Youjin Deng, Michel Ferrero, Thomas M. Henderson, Carlos A. Jiménez-Hoyos, E. Kozik, Xuan-Wen Liu, Andrew J. Millis, N. V. Prokof'ev, Mingpu Qin, Gustavo E. Scuseria, Hao Shi, B. V. Svistunov, Luca F. Tocchio, I. S. Tupitsyn, Steven R. White, Shiwei Zhang, Bo-Xiao Zheng, Zhenyue Zhu, and Emanuel Gull. Solutions of the Two-Dimensional Hubbard Model: Benchmarks and Results from a Wide Range of Numerical Algorithms. *Phys. Rev. X*, 5:041041, 2015.

[10] Thomas Schäfer, Nils Wentzell, Fedor Šimkovic IV, Yuan-Yao He, Cornelia Hille, Marcel Klett, Christian J. Eckhardt, Behnam Arzhang, Viktor Harkov, François-Marie Le Régent, Alfred Kirsch, Yan Wang, Aaram J. Kim, Evgeny Kozik, Evgeny A. Stepanov, Anna Kauch, Sabine Andergassen, Philipp Hansmann, Daniel Rohe, Yuri M. Vilk, James P. F. LeBlanc, Shiwei Zhang, A. M. S. Tremblay, Michel Ferrero, Olivier Parcollet, and Antoine Georges. Tracking the Footprints of Spin Fluctuations: A Multi-Method, Multi-Messenger Study of the Two-Dimensional Hubbard Model. *arXiv:2006.10769*, 2020.

[11] Gabriel Kotliar, Sergej Y. Savrasov, Gunnar Pálsson, and Giulio Biroli. Cellular Dynamical Mean Field Approach to Strongly Correlated Systems. *Phys. Rev. Lett.*, 87:186401, 2001.

[12] G. Kotliar, S. Y. Savrasov, K. Haule, V. S. Oudovenko, O. Parcollet, and C. A. Marianetti. Electronic structure calculations with dynamical mean-field theory. *Rev. Mod. Phys.*, 78:865–951, 2006.

[13] M. H. Hettler, A. N. Tahvildar-Zadeh, M. Jarrell, T. Pruschke, and H. R. Krishnamurthy. Nonlocal dynamical correlations of strongly interacting electron systems. *Phys. Rev. B*, 58:R7475–R7479, 1998.

[14] M. H. Hettler, M. Mukherjee, M. Jarrell, and H. R. Krishnamurthy. Dynamical cluster approximation: Nonlocal dynamics of correlated electron systems. *Phys. Rev. B*, 61:12739–12756, 2000.

[15] Nikolai V. Prokof'ev and Boris V. Svistunov. Polaron Problem by Diagrammatic Quantum Monte Carlo. *Phys. Rev. Lett.*, 81:2514–2517, 1998.

[16] Kris Van Houcke, Evgeny Kozik, N. Prokof'ev, and B. Svistunov. Diagrammatic Monte Carlo. *Phys. Proc.*, 6:95–105, 2010.

[17] K. Van Houcke, F. Werner, E. Kozik, N. Prokof'ev, B. Svistunov, M. J. H. Ku, A. T. Sommer, L. W. Cheuk, A. Schirotzek, and M. W. Zwierlein. *Nat. Phys.*, 8:366, 2012.

[18] E. Kozik, K. Van Houcke, E. Gull, L. Pollet, N. Prokof'ev, B. Svistunov, and M. Troyer. Diagrammatic Monte Carlo for correlated fermions. *Europhys. Lett.*, 90(1):10004, 2010.

[19] Riccardo Rossi. Determinant Diagrammatic Monte Carlo Algorithm in the Thermodynamic Limit. *Phys. Rev. Lett.*, 119:045701, 2017.

[20] Riccardo Rossi, Félix Werner, Nikolay Prokof'ev, and Boris Svistunov. Shifted-action expansion and applicability of dressed diagrammatic schemes. *Phys. Rev. B*, 93:161102, 2016.

[21] Alice Moutenet, Wei Wu, and Michel Ferrero. Determinant Monte Carlo algorithms for dynamical quantities in fermionic systems. *Phys. Rev. B*, 97:085117, 2018.

[22] Fedor Šimkovic and Evgeny Kozik. Determinant Monte Carlo for irreducible Feynman diagrams in the strongly correlated regime. *Phys. Rev. B*, 100:121102, 2019.

[23] M. Takigawa and D. B. Mitzi. NMR studies of spin dynamics in cuprates. *J. Low Temp. Phys.*, 95(1):89–93, 1994.

[24] R. Coldea, S. M. Hayden, G. Aeppli, T. G. Perring, C. D. Frost, T. E. Mason, S.-W. Cheong, and Z. Fisk. Spin Waves and Electronic Interactions in La_2CuO_4. *Phys. Rev. Lett.*, 86:5377–5380, 2001.

[25] Masaki Fujita, Haruhiro Hiraka, Masaaki Matsuda, Masato Matsuura, John M. Tranquada, Shuichi Wakimoto, Guangyong Xu, and Kazuyoshi Yamada. Progress in Neutron Scattering Studies of Spin Excitations in High-Tc Cuprates. *Journal of the Physical Society of Japan*, 81(1):011007, 2012.

[26] Hakuto Suzuki, Matteo Minola, Yi Lu, Yingying Peng, Roberto Fumagalli, Emilie Lefrançois, Toshinao Loew, Juan Porras, Kurt Kummer, Davide Betto, Shigeyuki Ishida, Hiroshi Eisaki, Cheng Hu, Xingjiang Zhou, Maurits W. Haverkort, Nicholas B. Brookes, Lucio Braicovich, Giacomo Ghiringhelli, Matthieu Le Tacon, and Bernhard Keimer. Probing the energy gap of high-

temperature cuprate superconductors by resonant inelastic x-ray scattering. *NPJ Quant. Mat.*, 3(1):65, 2018.

[27] Andrés Greco, Hiroyuki Yamase, and Matías Bejas. Origin of high-energy charge excitations observed by resonant inelastic X-ray scattering in cuprate superconductors. *Comm. Phys.*, 2(1):3, 2019.

[28] Fedor Šimkovic, J. P. F. LeBlanc, Aaram J. Kim, Youjin Deng, N. V. Prokof'ev, B. V. Svistunov, and Evgeny Kozik. Extended Crossover from a Fermi Liquid to a Quasiantiferromagnet in the Half-Filled 2D Hubbard Model. *Phys. Rev. Lett.*, 124:017003, 2020.

[29] Y. C. Chen, A. Moreo, F. Ortolani, E. Dagotto, and T. K. Lee. Spin-charge separation in the two-dimensional Hubbard and t-J models at low electronic density. *Phys. Rev. B*, 50:655–658, 1994.

[30] N. Bulut, D.J. Scalapino, and S.R. White. Spin-fluctuation mediated interaction in the two-dimensional Hubbard model. *Phys. C: Superconduc.*, 246(1):85 – 94, 1995.

[31] Alexandru Macridin, M. Jarrell, Thomas Maier, P. R. C. Kent, and Eduardo D'Azevedo. Pseudogap and Antiferromagnetic Correlations in the Hubbard Model. *Phys. Rev. Lett.*, 97:036401, 2006.

[32] O. Gunnarsson, T. Schäfer, J. P. F. LeBlanc, E. Gull, J. Merino, G. Sangiovanni, G. Rohringer, and A. Toschi. Fluctuation Diagnostics of the Electron Self-Energy: Origin of the Pseudogap Physics. *Phys. Rev. Lett.*, 114:236402, 2015.

[33] Xi Chen, J. P. F. LeBlanc, and Emanuel Gull. Superconducting Fluctuations in the Normal State of the Two-Dimensional Hubbard Model. *Phys. Rev. Lett.*, 115:116402, 2015.

[34] Mingpu Qin, Hao Shi, and Shiwei Zhang. Numerical results on the short-range spin correlation functions in the ground state of the two-dimensional Hubbard model. *Phys. Rev. B*, 96:075156, 2017.

[35] J. P. F. LeBlanc, Shaozhi Li, Xi Chen, Ryan Levy, A. E. Antipov, Andrew J. Millis, and Emanuel Gull. Magnetic susceptibility and simulated neutron signal in the two-dimensional Hubbard model. *Phys. Rev. B*, 100:075123, 2019.

[36] Cornelia Hille, Fabian B. Kugler, Christian J. Eckhardt, Yuan-Yao He, Anna Kauch, Carsten Honerkamp, Alessandro Toschi, and Sabine Andergassen. *arXiv:2002.02733*, 2020.

[37] Dominic Bergeron and A.-M. S. Tremblay. Algorithms for optimized maximum entropy and diagnostic tools for analytic continuation. *Phys. Rev. E*, 94:023303, 2016.

[38] R. Levy, J. P. F. LeBlanc, and E. Gull. Implementation of the Maximum Entropy Method for Analytic Continuation. *Comp. Phys. Comm.*, 215:149, 2017.

[39] A. Gaenko, A. E. Antipov, G. Carcassi, T. Chen, X. Chen, Q. Dong, L. Gamper, J. Gukelberger, R. Igarashi, S. Iskakov, M. Könz, J. P. F. LeBlanc, R. Levy, P. N. Ma, J. E. Paki, H. Shinaoka, S. Todo, M. Troyer, and E. Gull. Updated core libraries of the ALPS project. *Comp. Phys. Comm.*, 213:235–251, 2017.

[40] Alexander Gaenko, Emanuel Gull, Andrey E. Antipov, Lukas Gamper, Gabriele Carcassi, Joe Paki, Ryan Levy, Michele Dolfi, Jonas Greitemann, and James P.F. LeBlanc. ALPSCore: Version 0.5.4, 2016.

[41] Markus Wallerberger, Sergei Iskakov, Alexander Gaenko, Joseph Kleinhenz, Igor Krivenko, Ryan Levy, Jia Li, Hiroshi Shinaoka, Synge Todo, Tianran Chen,

Xi Chen, James P. F. LeBlanc, Joseph E. Paki, Hanna Terletska, Matthias Troyer, and Emanuel Gull. *arXiv:1811.08331*, 2018.

[42] J. Vučičević, J. Kokalj, R. Žitko, N. Wentzell, D. Tanasković, and J. Mravlje. Conductivity in the Square Lattice Hubbard Model at High Temperatures: Importance of Vertex Corrections. *Phys. Rev. Lett.*, 123:036601, 2019.

[43] Edwin W. Huang, Ryan Sheppard, Brian Moritz, and Thomas P. Devereaux. Strange metallicity in the doped Hubbard model. *Science*, 366(6468):987–990, 2019.

[44] J. Vučičević and M. Ferrero. Real-frequency diagrammatic Monte Carlo at finite temperature. *Phys. Rev. B*, 101:075113, 2020.

[45] Amir Taheridehkordi, S. H. Curnoe, and J. P. F. LeBlanc. Algorithmic Matsubara integration for Hubbard-like models. *Phys. Rev. B*, 99:035120, 2019.

[46] E. Y. Loh, J. E. Gubernatis, R. T. Scalettar, S. R. White, D. J. Scalapino, and R. L. Sugar. Sign problem in the numerical simulation of many-electron systems. *Phys. Rev. B*, 41:9301–9307, 1990.

[47] Shailesh Chandrasekharan and Uwe-Jens Wiese. Meron-Cluster Solution of Fermion Sign Problems. *Phys. Rev. Lett.*, 83:3116–3119, 1999.

[48] Amir Taheridehkordi, S. H. Curnoe, and J. P. F. LeBlanc. Optimal grouping of arbitrary diagrammatic expansions via analytic pole structure. *Phys. Rev. B*, 101:125109, 2020.

[49] Elliott H. Lieb and F. Y. Wu. Absence of Mott Transition in an Exact Solution of the Short-Range, One-Band Model in One Dimension. *Phys. Rev. Lett.*, 20:1445–1448, 1968.

[50] J. J. Vicente Alvarez, C. A. Balseiro, and H. A. Ceccatto. Spin- and charge-rotation invariant approach to the Hubbard model. *Phys. Rev. B*, 54:11207–11212, 1996.

[51] Atsushi Masumizu and Kiyoshi Sogo. Ward-Takahashi relations for SO(4) symmetry in the Hubbard model. *Phys. Rev. B*, 72:115107, 2005.

[52] R. P. Feynman. Space-Time Approach to Quantum Electrodynamics. *Phys. Rev.*, 76:769–789, 1949.

[53] Gordon Baym and Leo P. Kadanoff. Conservation Laws and Correlation Functions. *Phys. Rev.*, 124:287–299, 1961.

[54] J. M. Luttinger and J. C. Ward. Ground-State Energy of a Many-Fermion System. II. *Phys. Rev.*, 118:1417–1427, 1960.

[55] V. Zlatić, B. Horvatić, B. Dolički, S. Grabowski, P. Entel, and K.-D. Schotte. Perturbation expansion for the two-dimensional Hubbard model. *Phys. Rev. B*, 63:035104, 2000.

[56] Stéphane Daul and Michael Dzierzawa. Second order self-energy of the two-dimensional Hubbard model. *Zeitschrift für Physik B Cond. Matt.*, 103(1):41–44, 1997.

[57] Zhiqiang Tan. Monte Carlo Integration With Acceptance-Rejection. *J. Comp. and Graph. Stat.*, 15, 2006.

[58] Fabian B. Kugler. Counting Feynman diagrams via many-body relations. *Phys. Rev. E*, 98:023303, 2018.

[59] Walter Tarantino, Pina Romaniello, J. A. Berger, and Lucia Reining. Self-consistent Dyson equation and self-energy functionals: An analysis and illustration on the example of the Hubbard atom. *Phys. Rev. B*, 96:045124, 2017.

[60] A. Fetter and J. Walecka. *Quantum Theory of Many-particle Systems*. Dover Publications, Mineola, New York, 2003.

[61] Behnam Arzhang, A. E. Antipov, and J. P. F. LeBlanc. Fluctuation diagnostics of the finite-temperature quasi-antiferromagnetic regime of the two-dimensional Hubbard model. *Phys. Rev. B*, 101:014430, 2020.

[62] Andrey E. Antipov, James P. F. LeBlanc, and Emanuel Gull. Opendf - An Implementation of the Dual Fermion Method for Strongly Correlated Systems. *Phys. Proc.*, 68:43–51, 2015.

[63] Jan Gukelberger, Evgeny Kozik, and Hartmut Hafermann. Diagrammatic Monte Carlo approach for diagrammatic extensions of dynamical mean-field theory: Convergence analysis of the dual fermion technique. *Phys. Rev. B*, 96:035152, 2017.

[64] See Supplemental Materials, for results on the imaginary and real frequency axes including temperature dependence for a nonzero Matsubara frequency, order-by-order contribution of diagrams in the real frequency space, comparison with TMA and dependence of results to the regulator in the analytic continuation process.

[65] S. M. Hayden, G. Aeppli, H. A. Mook, S-W. Cheong, and Z. Fisk. Spin dynamics in the two-dimensional antiferromagnet La_2CuO_4. *Phys. Rev. B*, 42:10220–10225, 1990.

[66] N. S. Headings, S. M. Hayden, R. Coldea, and T. G. Perring. Anomalous High-Energy Spin Excitations in the High-T_c Superconductor-Parent Antiferromagnet La_2CuO_4. *Phys. Rev. Lett.*, 105:247001, 2010.

Chapter 6

Summary and future work

6.1 Summary

We presented a new method to evaluate the diagrammatic expansions composed of bare Green's functions. Our method enables one to directly compute perturbative expansions in real-frequency space, a task which is inaccessible in other well-established many body techniques. Although the method was used to calculate the self-energy and susceptibility expansions for the 2D single-band Hubbard model with nearest neighbor hopping, it is applicable to any diagrammatic expansion with arbitrary time-independent potential, dimensionality and dispersion, as long as the analytic representation of the Green's functions is known.

Essential to our algorithm is to first produce the Feynman diagrams and translate them into their corresponding symbolic forms. We introduced an array representation to express the terms in the perturbative expansion. Algorithmic Matsubara integration, which is in fact an iterated application of the standard residue theorem, was implemented to evaluate the Matsubara sums of each diagram. In order to improve the efficiency of the numerical integrations of the momenta, we utilized the analytic

pole structure of the diagrams to systematically construct the sign-blessed diagram groups. Finally, we used Monte Carlo integration procedures to evaluate the momenta sums of the truncated series.

Important features of our approach can be summarized as follows. First, the temporal summations are performed symbolically, i.e., the temporal sums can be evaluated exactly (up to machine precision) and as the result statistical error and truncation error (due to introducing a cut-off) are absolutely zero. Second, since the analytic representation of the momenta integrands for each diagram is available, the analytic continuation is imposed symbolically, which eliminates the need for the numerical analytic continuation processes. Thus, for the first time, we present reliable numerical results for the response functions, such as the Green's functions and spin susceptibilities, of the 2D Hubbard model. Third, our procedure can be used to evaluate the diagrams at any temperature since it is fully analytic and does not suffer from sampling issues in typical Monte Carlo routines. Fourth, the sign problem was minimized by using graph invariant transformations, which are based upon the analytic form of the Green's functions. Altogether we can substantially reduce the computational cost to obtain reasonable statistical errors.

We therefore believe our methodology opens new avenues of advancement for condensed matter and high energy physics without introducing any additional conceptual complexity. As such we are excited for the prospect of the application of the method to other lattice systems and interactions.

6.2 Future work

Our method is in principle applicable to any diagrammatic expansion in condensed matter and high energy physics as long as the analytic representations of the diagrams

are known. Therefore, our method can be used to deal with a variety of different classes of problems where the perturbation theory can be used. Examples of such problems are summarized as follows:

1. Our formalism can be easily applied to study the perturbative expansions of self-energy and susceptibility functions for multi-band Hubbard-like models [1] with diagonal hopping matrices. The simplest examples of such systems are mass-imbalanced Hubbard model [2] and Hubbard model in the presence of a Zeeman term [3–8]. In cases with non-diagonal hopping matrices one can conceptually use the method, however, since the expression of the bare Green's functions are different from the single-band model, slight modifications should be imposed.

2. The polaron problem was the first problem solved by DiagMC methods in Matsubara space [9]. Our method with minor modifications can be applied to this problem to evaluate the perturbative expansion on the real frequency axis.

3. AMI methodology can be also used to evaluate the perturbative expansions of multi-orbital (molecular) Hubbard models [10], although the diagrammatic expansion is different and instead of momenta sums one deals with sums over orbitals.

4. One of the disadvantages of working in the bare diagrammatic schemes (as we did in this project) is the poor convergence rate of the expansions, therefore, evaluating the expansion in high-coupling regimes, i.e., large U and low T, is a formidable task. For this reason other diagrammatic schemes such as shifted action DiagMC have been recently proposed [11]. Since in this scheme the expansions are constructed with respect to renormalised Green's functions (which have similar analytic structure as the bare Green's functions) our approach is

still applicable and can be utilized to evaluate the self-energy and susceptibility functions on both the imaginary and real frequency axes.

Bibliography

[1] Nagamalleswararao Dasari, Wasim Raja Mondal, Peng Zhang, Juana Moreno, Mark Jarrell, and NS Vidhyadhiraja. A multi-orbital iterated perturbation theory for model Hamiltonians and real material-specific calculations of correlated systems. *The European Physical Journal B*, 89(9):202, 2016.

[2] Marie-Therese Philipp, Markus Wallerberger, Patrik Gunacker, and Karsten Held. Mott-Hubbard transition in the mass-imbalanced Hubbard model. *The European Physical Journal B*, 90(6):114, 2017.

[3] Elliott H. Lieb and F. Y. Wu. Absence of Mott Transition in an Exact Solution of the Short-Range, One-Band Model in One Dimension. *Phys. Rev. Lett.*, 20:1445–1448, 1968.

[4] Ya-Min Quan, Wei-Cheng Bao, Wei-Hua Wang, and Da-Yong Liu. Phase diagrams of the Kane-Mele-Hubbard model in the presence of an external magnetic field. *Journal of Physics: Conference Series*, 827:012009, 2017.

[5] K. Penc and J. Sólyom. One-dimensional Hubbard model in a magnetic field and the multicomponent Tomonaga-Luttinger model. *Phys. Rev. B*, 47:6273–6292, 1993.

[6] Ferdinando Mancini, Evgeny Plekhanov, and Gerardo Sica. T= 0 phase diagram of the 1D Hubbard model with magnetic interactions in the narrow band limit. *Open Physics*, 10(3):609–614, 2012.

[7] Holger Frahm and Temo Vekua. The Mott metal–insulator transition in the 1D Hubbard model in an external magnetic field. *Journal of Statistical Mechanics: Theory and Experiment*, 2008(01):P01007, 2008.

[8] F Mancini and FP Mancini. Extended Hubbard model in the presence of a magnetic field. *The European Physical Journal B*, 68(3):341–351, 2009.

[9] Nikolai V. Prokof'ev and Boris V. Svistunov. Polaron Problem by Diagrammatic Quantum Monte Carlo. *Phys. Rev. Lett.*, 81:2514–2517, 1998.

[10] Jia Li, Markus Wallerberger, and Emanuel Gull. Diagrammatic Monte Carlo Method for Impurity Models with General Interactions and Hybridizations. *arXiv: 2004.00721*, 2020.

[11] Wei Wu, Michel Ferrero, Antoine Georges, and Evgeny Kozik. Controlling Feynman diagrammatic expansions: Physical nature of the pseudogap in the two-dimensional Hubbard model. *Phys. Rev. B*, 96:041105, 2017.

Appendix A

Residue theorem

Assume a complex function $h(z)$ defined on the complex plane. The poles of $h(z)$ are denoted by z_0. We first consider the following contour integral:

$$J = \oint_C h(z)f(z)\,\mathrm{d}z, \tag{A.1}$$

where f is Fermi distribution function and C is a circle with infinite radius. If $|h(z)f(z)|$ decreases faster than $|z|^{-1}$, Jordan's lemma [1] implies that $J = 0$. The contour C encloses all of the poles of $h(z)$ as well as those of $f(z)$, so residue theorem leads to

$$\sum_{z_f} \mathrm{Res}[h(z)f(z)]_{z_f} + \sum_{z_0} \mathrm{Res}[f(z)h(z)]_{z_0} = 0, \tag{A.2}$$

where $z_f = i(2n+1)\pi/\beta$ are the poles of Fermi function and

$$\mathrm{Res}[f(z)]_{z_f} = \lim_{z\to z_f} \frac{z - z_f}{e^{\beta z}+1} = \lim_{z\to z_f} \frac{1}{\beta e^{\beta z}} = -\frac{1}{\beta}. \tag{A.3}$$

Substituting Eq. (A.3) in Eq. (A.2) we obtain

$$\frac{1}{\beta}\sum_{i\nu_n} h(i\nu_n) = \sum_{\{z_0\}} \mathrm{Res}[f(z)h(z)]_{z_0}. \tag{A.4}$$

Bibliography

[1] H. J. Weber and G. B. Arfken. *Essential Mathematical Methods for Physicists*. Academic Press, London, 2003.

Appendix B

Necessity of AMI in evaluation of Matsubara summations: an instructive example

We consider the bare bubble as the simplest diagram in the diagrammatic expansion of the susceptibility functions. The momenta integrand of the diagram is given by

$$I = \frac{1}{\beta} \sum_{\nu_n} \mathcal{G}_0(i\nu_n, \mathbf{k}) \mathcal{G}_0(i\nu_n - i\Omega_m, \mathbf{k} - \mathbf{q}), \tag{B.1}$$

where $i\nu_n = (2n+1)\pi/\beta$ is the internal frequency, $i\Omega_m = 2m\pi/\beta$ is the external frequency, $\mathbf{k}$ is the internal momenta and $\mathbf{q}$ is the external momenta. We plot the momenta integrand of polarization function denoted by I in Fig. B.1 and compare the AMI result with that of naive Matsubara summation. The figure shows that AMI is probably essential to achieve a reliable result. This simple example suggests that by choosing a large enough cut-off number n_c, a reliable result will be obtained,

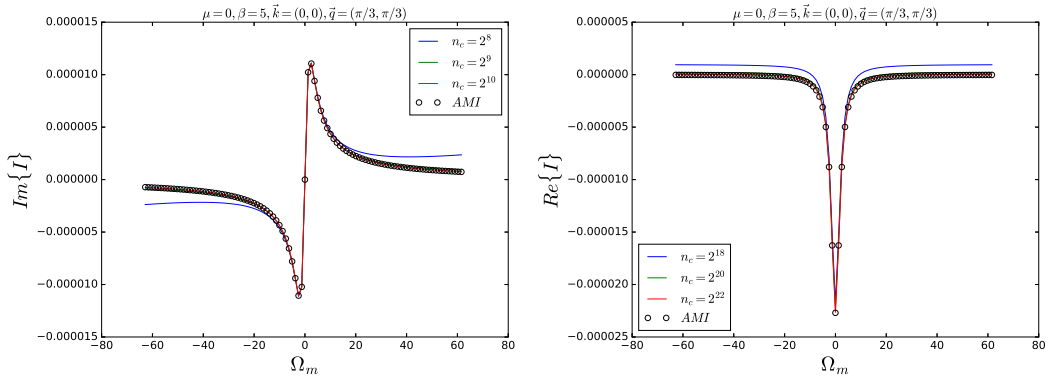

Figure B.1: *Left*: Imaginary part, and *Right*: Real part of the momenta integrand of the bare bubble. We set $\mu = 0$, $\beta = 5$, $\mathbf{k} = (0, 0)$, and $\mathbf{q} = (\pi/3, \pi, 3)$. While the imaginary part of the naive sum approaches to the exact result (obtained by AMI) at $n_c = 2^{10}$, the real part convergence rate is poor.

however, in practice this could be computationally expensive. Therefore, using AMI is necessary when one works in the frequency representation.